COPPER INDIUM DISELENIDE (CIS) BASED SOLAR CELLS: EFFECT OF CIS PREPARATION CONDITIONS AND THICKNESS ON PERFORMANCE

By

Julius Mwakondo Mwabora

A thesis submitted in fulfillment of the requirements for the degree of Doctor of Philosophy (Physics) of the University of Dar es Salaam.

University of Dar es Salaam

September 1999

CERTIFICATION

The undersigned certify that they have read and hereby recommend for acceptance by the University of Dar es Salaam a thesis entitled: *Copper Indium Diselenide (CuInSe$_2$) based Solar Cells: Effect of CuInSe$_2$ Films Preparation Conditions and Thickness on Performance*, in fulfillment of the requirements for the degree of Doctor of Philosophy (Physics).

Prof. R. T. Kivaisi

Department of Physics

University of Dar es Salaam

(SUPERVISOR)

Date:.....4.10.99.....

Prof. R. W. Birkmire

Institute of Energy Conversion

University of Delaware

(CO - SUPERVISOR)

Date:.....9-29-99.....

DECLARATION
AND
COPYRIGHT

I, Julius Mwakondo Mwabora, declare that this thesis is my own original work and that it has not been presented and will not be presented to any other University for a similar or other degree award.

Signature ------------------------------

ACKNOWLEDGMENT

I would like to express my sincere gratitude to Prof. R. T. Kivaisi of the University of Dar es Salaam, Tanzania, for supervising me in this research. His introduction of this field to me, his availability, guidance, cooperation and critical suggestions made this work possible.

Many thanks are due to Prof. R. W. Birkmire for supervising me while I was at the Institute of Energy Conversion (IEC), University of Delaware, USA. His many valuable discussions, guidance and keen interest are immensely acknowledged.

Dr. W. N. Shafarman, who is the electronic materials manager at IEC, University of Delaware is highly appreciated. His unfailing availability, help with research logistics and fruitful discussions while at IEC enhanced compilation of this thesis.

Mike Engelmann of IEC is thanked for selenizing all my samples. Skillful technical help came from Khalfani Mtelela and David Lameck of the University of Dar es Salaam and Kevin Hart, Tom Lampros and Shanon Fields of IEC, University of Delaware. Others whose support in one way or another made this work easier than it would otherwise have been include: Prof. Elias Lushiku, Dr. Godfrey Mbise, Ms Angela Rutakomozibwa , Mr. Damsom Nsimama, and Ms Margaret Samiji all of the University of Dar es Salaam and Prof. Fraser Russel, Dr. Matt Marudachalam, Dr. Juliette Zhu, Mr. Brian McCandless, Mr. Ron Dozier, Mr. Jochen Titus, Mr. Greg Hanket, Mr. Moses Haimbodi and Mr. Chuck Debbo of the University of Delaware. Gratitude is due to them all. I would also like to thank all other people at the Physics

Department, University of Dar es Salaam and the Institute of Energy Conversion, University of Delaware and elsewhere that I have worked with and have kindly introduced me to various equipment whose mention by names would make an inexhaustive list.

To my parents - Mwabora Mwandisha and Scholar Majina Mwabora - and my fiancee

Christina Rutakomozibwa

ABSTRACT

The effect of $CuInSe_2$ thin film preparation conditions and thickness on $CuInSe_2$ based solar cells has been investigated. Prior to $CuInSe_2$ thin films and device fabrication, metallic Cu and In resistivity changes with deposition conditions were studied. The $CuInSe_2$ thin films were fabricated by two stage process which involved DC sputtering of metallic CuIn bilayers followed by reaction of the bilayers in H_2Se gas in a chemical vapor deposition reactor.

Metallic Cu and In films resistivities depend on vacuum deposition conditions as well as their thicknesses. For deposition parameters studied in this work, Cu film resistivity changes are within the order of 10^1 while those for In film were up to order of 10^{11}.

A semi quantitative description on the formation of $CuInSe_2$ films with respect to reaction period, reaction temperature, and precursor thickness has been given. This has helped to explain the phases observed and their effects on device performance. Low reaction temperatures require long reaction periods for complete reaction of CuIn precursors which is consistent with low reaction rate constants for low reaction temperatures. At temperatures greater than 400 °C device performance deteriorates.

A kinetic model was used to predict the progressive number of moles of $CuInSe_2$ and InSe phases in the selenized CuIn bilayers and compared with experimental number of moles calculated from XRD counts. Generally, the experimental data were found to be in good qualitative agreement with those predicted. The best solar cell (efficiency was 10.6 %) in this work was obtained using an absorber layer with a trace of InSe phase. This means a good device with efficiency greater than 10 % can be obtained using an

absorber layer with a trace of InSe phase provided that the number of InSe moles approaches zero.

For each reaction period, there is a limiting $CuInSe_2$ thickness which gives the highest efficiency. Similarly, for each precursor thickness, there is a limiting efficiency which can be obtained. For commercial considerations, the most interesting result is the 7.41 % efficiency obtained for a 0.6 µm thick $CuInSe_2$ absorber layer prepared for 15 minutes at reaction temperature of 350 °C. The thinner $CuInSe_2$ saves the starting Cu and In materials while the short reaction period and the lower reaction temperature translates to low operating costs.

TABLE OF CONTENTS

TABLES

FIGURES

LIST OF SYMBOLS AND ACRONYMS

%	= Percent
θ	= Bragg angle
η	= Efficiency
δ	= Grain boundary
δ_c, γ_c	= Phases for a Pseudo-binary Cu_2Se/In_2Se_3
μ	= Mobility
Θ	= Debye temperature
λ	= Wavelength
$\propto$	= Component of radiation
π	= 22 / 7
$\alpha(\lambda)$	= Absorption coefficient for wavelength λ
$\lambda_{\alpha 1}$	= 1.540562 Å (wavelength of the Cu Kα component of radiation)
Ω/sq.	= Ohm per square
μ_l	= Linear absorption coefficient (m^{-1})
α_a, β, γ	= Angles between plane axes in a crystal
°C	= Degrees centigrade
ρ_d	= Density per square centimeter for grains

Δf_q $\qquad$ = Change in frequency of the crystal

θ_i $\qquad$ = Volume fraction of the species i

ρ_i $\qquad$ = Density of species i

μ_n $\qquad$ = Electron mobility

μ_m $\qquad$ = Linear mass absorption coefficient

μm $\qquad$ = Micrometer

μ_0 $\qquad$ = $4\pi \times 10^{-7}$ m kg C^{-2}

μ_p $\qquad$ = Hole mobility

Ωm $\qquad$ = Ohm meter

τ_n $\qquad$ = Electron life time

τ_p $\qquad$ = Hole life time

α_p, L_p, δ_p, γ_p, β_p, η_p = Phases for Cu-In system

ρ_f $\qquad$ = Film density

ρ_q $\qquad$ = Density of quartz

@ $\qquad$ = at

+ $\qquad$ = Unidentified phase (d spacing = 1.86)

++ $\qquad$ = Unidentified phase (d spacing = 3.03)

Å $\qquad$ = Angstrom

A $\qquad$ = Cross-sectional area of incident beam (m^2)

a, c $\qquad$ = Plane axes for a crystal

A_{ab} $\qquad$ = Absorptance

A_d	= Grain cross sectional area
A_{Dqf}	= Diode quality factor
a_{ad}	= Atomic dimension
AMX	= Air mass number
a_o, c_o	= Lattice parameters
A_q	= Area of the antinodal surface of the crystal
at.	= Atomic
B4	= Before
C	= Coulomb
CBD	= Chemical Bath Deposition
c_i	= Concentration of species i
CIGS	= $CuInGaSe_2$
cm	= Centimeter
$C_p(T)$	= Specific heat
CVD	= Chemical Vapor Deposition
DC	= Direct current
D_{cu}	= Density of Cu film
d	= Plane spacing for a crystal
d_{cr}	= Thickness of field free collection region
D_{In}	= Density of In film
D_n	= Electron diffusion coefficient
D_p	= Hole diffusion coefficient
d_q	= Quartz crystal thickness
E	= Electrostatic field
E_{ai}	= Activation energy
EDS	= Energy Dispersive Spectroscopy
E_r	= Fermi level

E_g	= Band gap
ENEA	= Ente per le Nuove Technologie, l'Energia e l'Ambiente
EPV	= Energy Photovoltaics
eV	= Electron volt
F	= Debye function
f	= Fraction
FF	= Fill Factor
forw	= Forward
f_q	= Frequency of the fundamental resonance of a thickness mode for an AT cut crystal
F_{sf}	= Structure factor
G	= Generation rate
G_n	= Electron generation rate
g_n	= $qD_n dn/dx$
g_p	= $qD_p dp/dx$
G_p	= Hole generation rate
hkl	= Miller indices
I	= Current
I - V	= Current - Voltage
I_{dl}	= Integrated intensity per unit length of diffraction line
IEC	= Institute of Energy Conversion
IEEE	= Institute of Electrical and Electronic Engineers
I_j	= Intensity of the selected angle of the jth phase
I_L	= Light generated current
I_0	= Diode injection current
I_{0b}	= Intensity of incident beam
ISET	= International Solar Energy Technology

J	= Current density
JCPDS	= Joint Council for Powder Diffraction Studies
J_L	= Light-generated current density
J_{mp}	= Maximum power current density
J_o	= Dark current density
J_{sc}	= Short circuit current density
JV	= Current density - Voltage
K	= Kelvin
k	= Boltzmann constant
kg	= Kilogram
K_i	= XRD intensity per unit mole for species i.
k_i'	= $k_i[Se]$: Modified set of reaction rate constant for species i assuming selenium species concentration is constant
k_i	= Reaction rate constant for species i; i = 2, 3, 5, and 7 for In, In_2Se, CuIn or $Cu_{11}In_9$, and InSe, respectively
K_{io}	= Frequency factor
kJ	= Kilo joules
K_q	= Constant for a quartz crystal
kWh	= Kilowatt hour
L	= Diffusion length
l	= Grain size
M	= Molar
m	= Meter
mA	= Milliampere
mbar	= Millibar
M_{cu}	= Mass of Cu film
m_e	= Mass of an electron

m_f	= Mass of the film
M_i	= Molecular weight of the ith phase
M_{in}	= Mass of In film
mm	= Millimeter
MW_{Se}	= Molecular weight of selenium
n	= Electron
NASA	= National Aeronautics and Space Administration
N_{cu}	= No. of moles of copper
n_i	= Number of moles
N_{in}	= No. of moles of indium
N_{in}	= Number of moles of In during selenization
nm	= Nanometer
No, Cu	= Initial number of moles of Cu in the CuIn precursor
No, In	= Initial number of moles of In in the CuIn precursor
No.	= Number
N_q	= Frequency constant for an AT cut quartz crystal vibrating in the thickness shear mode
NREL	= National Renewable Energy Laboratory
P	= Pressure
p	= Holes
Pa	= Pascal
P_{in}	= Total power of incident light source
p_{mf}	= Multiplicity factor
P_{mp}	= Maximum electrical power
PV	= Photovoltaic
PVD	= Physical Vapor Deposition
Q	= Quantum efficiency

q	= Charge of an electron
Q_b	= Backwall Quantum Efficiency
Q_F	= Frontwall Quantum Efficiency
Q_f	= Frontwall quantum efficiency with d_{cr} approaching infinity
R	= Gas constant
r	= Radius of diffractometer circle
$R_{Cu/In}$	= Cu/In ratio
rct	= reaction
r_d (I)	= Rate of delivery of species
Refl	= Reflected
RF	= Radio Frequency
RGA	= Residual gas analyzer
R_m	= Mean earth-sun distance
R_n	= n/τ_n
R_p	= p/τ_p
r_r (I)	= Rate of removal of species
Rrefl	= Reflectance
r_{rxn}	= Rate of reaction of the ith species
R_s	= Series resistance
R_{sh}	= Sheet resistance
R_{sht}	= Shunt resistance
RTP	= Rapid Thermal Processing
R_z	= Acoustic impedance ratio
s	= Seconds
SEM	= Scanning Electron Microscopy
SL	= Soda lime

SSI   = Siemens Solar Industries

T   = Temperature

t   = Time of reaction

t_{CIGS} = Thickness of CIGS: $t_{CIGS} = d_{cr} + w$

t_{CIS} = $CuInSe_2$ film thickness

t_{Cu} = Thickness of Cu film

TEM   = Transmission Electron Microscopy

T_l = Period of the loaded crystal

t_{In} = Thickness of In film

T_q = Period of the uncoated crystal

T_{tf} = Temperature factor

T_{trans} = Transmittance

ULSI   = Ultra Large Scale Integrated Circuits

V   = Voltage

v   = Volume of unit cell (m^3)

V_f = Volume of film

V_{mp} = Maximum power voltage

V_{oc} = Open circuit voltage

W   = Watt

w   = Depletion width

w_i = Mass fraction for species i

x   = Axis along the n-window and CIGS absorber layer

x_i = Mole fraction of species i

XRD   = X - Ray Diffraction

Z   = Zenith Angle

Z_{cu} = Atomic weight of copper

Z_{in} = Atomic weight of indium

CHAPTER ONE

INTRODUCTION

PART ONE: BACKGROUND

1.1 General Introduction

The origin of most of the energy presently available on earth is the sun. This includes the energy for direct heating, as well as wind energy, hydroelectric power, and energy derived from fossil fuels. Limitations, environmental issues and safety issues associated with conventional energy sources such as fossil and nuclear fuels has made human beings aware of energy sources which are renewable and environmental benign.

Solar energy has been identified as one of the promising renewable energy for exploitation. Growing interest for solar energy can be attributed to the fact that solar energy is abundant and its depletion is negligible. A country cannot be cut off from it. Another reason is that in solar energy conversion, no harmful environmental or societal consequences have been experienced.

Disruption of the oil supplies to the industrialized world in the early 1970's led to serious considerations of photovoltaic as a terrestrial power source. The commercialization of this technology has been hindered by the high cost per peak watt for the solar modules. Even though researchers have made extraordinary progress over the years, improved performance, lower costs and reliability remain to be the major consideration today [Stone, 1993]. Policy goals by some governments such as

improved energy security and diversity, reduced emissions of greenhouse gases, and increased levels of technology growth has spawned several photovoltaic technologies in the past two decades.

1.2 The Sun and Solar Radiation

The sun, our closest star, is the origin of most of the energy for maintaining life on earth and produces the necessary gravitational attraction to keep our planet in a nearly circular orbit. It has a mass of 1.99×10^{30} kg and a radius of 6.96×10^8 m [Wielder, 1982]. The mean earth-sun distance, R, is approximately 1.5×10^{11} m. A simple model assumes that the sun is circular and behaves as a black body whose surface temperature is maintained at 6000 K. This surface temperature is kept constant by energy generated through continuos nuclear fusion of hydrogen into helium in the interior. The interior temperature is about 10^7 K. As a result of the core temperature, the surface radiates electromagnetic radiation in all directions of space. Out of the approximately 8.33×10^{25} kWh of energy radiated by the sun into space everyday, the earth receives about 4.41×10^{15} kWh of the energy [Cheremisinoff, 1978].

Most of the solar spectrum lies in the range between 0.25 to 2.5 μm with the maximum occurring at 0.55 μm for AM 1.5. Solar spectrum is modified by the atmosphere if it is observed on the earth's surface. The absorption and scattering of light in the atmosphere is mainly due to ozone, water vapor, carbon dioxide, aerosols and particulate matter.

The greater the distance light has to travel, the more the spectrum is modified. This effect is conveniently described by defining an air mass number (AM X). Air mass according to IEEE Standard Dictionary of Electrical and Electronics Terms [Jay, 1977] is the mass of air between a surface and the sun that affects the spectral distribution and intensity of sunlight. AM 0 specifies the spectral distribution and intensity of sunlight outside the atmosphere. AM 1 is the spectral distribution and intensity of sunlight on earth at sea level with the sun directly overhead and passing through the standard atmosphere. AM 2 is the solar radiation at ground level when the sun is 30° above horizon. The spectral distribution of the solar radiation for AM 0, AM 1.5 and blackbody is as shown in figure 1.1. The spectral distribution of AM 0 radiation differs from that of an ideal black body. This is due to such effects as differing transmittiviy of the sun's atmosphere at different wavelengths.

1.3 Types of Solar Cells

The first practical solar cell was developed at Bell laboratories in 1954 [Chaplin et. al., 1954; Chaplin et. al., 1957]. In the beginning, solar cells were made from semiconductor grade single crystalline and were the power source of choice for use in space applications such as on satellites. The systems were very reliable, and cost was of little concern with regard to the huge space programs budget.

Solar cells can be categorized into three main groups:

- Crystalline and polycrystalline silicon

- III-V group single crystals

- Thin films

1.3.1. Crystalline and Polycrystalline Silicon

Crystalline and polycrystalline silicon are produced by refining silicon. The source material for extraction of silicon is silicon dioxide, the major constituent of sand. For use in solar cells as well as other semiconductor devices, silicon must be very pure. Standard purification techniques have already been developed [Runyan, 1965].

Silicon is an indirect band gap material. This means over a large range of visible spectrum, light absorption occurs only with assistance of a phonon. The phonon provides the additional wave vector needed.

1.3.1.1 Single-Crystal Silicon

Single-crystal silicon forms the basis of the present solar cell technology. The first reasonably efficient silicon cells was developed in 1953. The major application for these cells has been for space craft till 1973 when increased interest in renewable energy resources led to several companies currently producing cells specifically for terrestrial use. Silicon devices have attained an efficiency of 23% [Green M. A., 1993]. This value can be increased to 28% when a concentrator is used [Green and Emery, 1993]. This performance achievement can be attributed to the substantial understanding of the material properties and improved design of the solar cell. Commercial silicon solar cell modules are available with conversion efficiencies over 15%. The major disadvantage of single crystal silicon solar cells are the requirements of high grade material and the problems associated with making single crystals in large areas. Efforts have been focused on single crystals silicon ribbon technology to solve

large area requirements. This method is energy intensive and requires large material input.

1.3.1.2 Polycrystalline Silicon

Polycrystalline silicon is refined silicon consisting of small grained crystals. This technology combines the benefits of high performance single crystal silicon with low cost of thin films. Silicon thin films used for solar cells are less than 100 μm thick and

are

obtained by sheet growth process from the liquid melt. The rate of growth of thin films determines the cost-effectiveness of the process. Sub-modules and small area efficiencies of 12.2 % (on 240 cm^2) and 16.6 % (on 1 cm^2), respectively, have been demonstrated by AstroPower Inc. [Bai et. al., 1997; Ford et. al, 1996]. Advances in semiconductor wafer technology and processing techniques should further improve the device efficiency.

1.3.2 III-IV Group Single Crystals

These are mainly used for space applications. Although expensive, their cost can be compensated by using concentrators which increase the energy conversion efficiency under higher illumination. Concentrators focus light from a large area to a small area where the solar cell sits thereby increasing illumination to many times the terrestrial sunlight. The major solar cells in this category are Gallium arsenide and Indium phosphorous.

1.3.2.1 Gallium Arsenide

Gallium arsenide has a well developed technology because of the commercial interest in this material for light-emitting diodes and semi-conductor injection lasers. Its direct band gap nature means that sunlight is absorbed very quickly after entering it. It also means that minority carrier lifetimes and diffusion lengths are much smaller than silicon. The most efficient solar cells made to date have been based on this material. GaAs cells of 25.1 % efficiency have been confirmed [Green and Emery, 1993]. When used in concentrator applications, the efficiency increases to 27.6 % [Vernon et. al., 1991]. The highest confirmed efficiency is 32.6 % for a GaAs/GaSb multijunction stacked cell operating at 100-suns concentration, i.e., light concentrated to an intensity of 100 times terrestrial sunlight. [Fraas et. al., 1990]. The high cost of this material caused by the limited resources of Gallium [Hovel, 1975] and the toxic nature of the arsenic are its major limitation. This has limited its use to space applications only.

1.3.2.2 Indium Phosphorous

Indium phosphorous (InP) is a direct band gap material with a band gap of 1.34 eV close to the optimum for solar energy conversion. Research on InP heterojunction did not start until about 1974, probably because of unavailabity of high quality single crystals of p-type InP. InP crystals are grown by the Czochraski method at high pressures or by using a liquid encapsulation technique to preserve stoichiometry. A 21.9 % efficient InP crystalline solar cell has been reported [Keavney et. al., 1990]. When 99-suns concentration was used, the efficiency increased to 24.3 % [Ward et. al., 1991]. A 31.8 % multijunction InP/GaInAs operating at 50-suns concentration has been achieved [Wanlass et. al., 1990]. The major limitation for this technology is high cost due limited resources for indium and purification of phosphorous.

1.3.3. Thin Film Solar Cells

Devices based on Cu_2S/CdS were the first to achieve 10 % conversion efficiency in laboratory scale among thin films. However, the difficulty of achieving more than 10 % efficiency on large area combined with stringent encapsulation requirements to minimize degradation prevented its wide-spread use.

Thin films are usually 0.5 - 5 µm thick compared to crystalline silicon devices which are approximately 300 µm thick. Although the processing of thin films solar cells is difficult, these cells offer two very important advantages for terrestrial applications: first, since the required thickness of the active absorber layer is on the order of several times the optical absorption length of the material, solar cells using direct band gap materials can be made very thin, usually a few microns thick, thus lowering the material cost; and secondly, the thin film configuration lends itself to large area and continuos flow processing. Interconnections in thin films can be done monolithically allowing large area modules to be fabricated on a single substrate. There is a wide variety of low-cost deposition techniques for thin films. Thin films can also be deposited by a combination of processing methods, thus allowing one to manipulate the microstructure to maximize device performance. Currently, the major thin film options are amorphous silicon (a-Si), polycrystalline cadmium telluride (CdTe), and polycrystalline copper indium diselenide ($CuInSe_2$). All the options appear to be scaleable and amenable to mass production, have the potential for efficiencies greater than 10 %, and have demonstrated reliability in the short term.

1.3.3.1. Amorphous Silicon

In 1975 [Spear W. E. and LeComber P. G. (1975)], it was reported that amorphous silicon produced by the glow discharge decomposition of silane (SiH_4) could be doped

to form p-n junctions. Currently, commercial products based on a-Si:H solar cells are already in the market. The role of hydrogen is to saturate dangling bonds on the internal microvoids of the film and at other defects in the structure. A development in this area is the use of amorphous silicon layers with both hydrogen and fluorine incorporated into the structure [Medan et. al.(1980)]. These a-Si: F: H alloys have been produced by the glow discharge decomposition of SiF_4 in the presence of hydrogen. This approach has been reported to lead to more desirable properties for photovoltaic action, in particular a reduced density of states within the forbidden gap [Medan et. al.(1980)].

Recent developments in a-Si:H alloys such as a-SiGe:H, a-SiN:H and a-SiSn:H to taylor the electrical and optical properties of devices are very promising and broaden the scope of applications into areas like transistors and photosensors [Hamakawa et. al., 1993]. Incorporation of deuterium instead of hydrogen in a-Si devices may improve their life time as Si-D bond is thought to be more resistant to hot electron excitation than the Si-H bond [Van de Walle, 1998]. MOS transistors with deuterium incorporated into the Si/SiO_2 interface instead of hydrogen have registered an improvement in lifetime [Lyding J. W., 1996].

Single junction and multijunction devices are being explored for improved performance [Stone, 1991]. One major concern with amorphous-silicon material is that all device quality amorphous-Si solar cell exhibit light induced degradation often referred to as the Staebler-Wronski effect [Staebler and Wronski(1977); Zanzucchi et. al., 1977]. Recently, a stable 13.5 % triple junction a-Si/a-SiGe/a-SiGe cell on a small area was demonstrated [Yang et. al., 1997]. A one square-foot area sub-module exhibiting a stable aperture-area efficiency of 10.4 % using the same triple structure above was also achieved [Guha, (1996); Guha et. al., (1994)].

1.3.3.2 Cadmium Telluride

The Cadmium telluride (CdTe) thin film solar cells are based on a CdTe/CdS heterojunction. CdTe has a direct band gap of 1.45 eV which is ideal for conversion of sunlight to electricity. Polycrystalline thin films of 1 μm thick are sufficient for 99 % absorption of the visible light [Suntola, 1993]. Another advantage of CdTe technology lies in that a variety of low cost techniques are available to process the material. Closed-space sublimation, physical vapor deposition, electrodeposition, spray pyrolysis, and screen printing are some of the methods used to process CdTe.

Achievements such as high cell efficiencies, good module performance and existence of pilot production facilities have placed CdTe as one of the most promising candidates for terrestrial applications [Zweibel, 1992]. Small area cell efficiency of 16 % has been achieved [Ohyama et. al., 1997] and it is expected efficiencies can be improved to 18 % in the near future [Chu and Chu, 1993]. Solar cells Inc. have introduced a 2 × 4 sq. ft. module with 7.8 % aperture efficiency. CdTe solar cell technology appears to be scaleable and viable. Problems associated with this technology are reactions of CdTe with the encapsulating material and the use of toxic cadmium.

1.3.3.3 Copper Indium Diselenide

The $CuInSe_2$ solar cells are based on $CuInSe_2$/ZnO heterojunction with a thin (20 - 50 nm) buffer layer of CdS between $CuInSe_2$ and ZnO. Its high absorption coefficient ($\alpha > 10^5$ cm^{-1}), good thermal, environmental and electrical stability makes it a very promising material for photovoltaic applications. Among the scaleable processing methods of $CuInSe_2$ film are co-evaporation of constituent elements, selenization of Cu/In bilayers, and annealing of stacked elemental layers. $CuInSe_2$/CdS/ZnO solar

cell efficiencies of 12 - 15.4 % have been reported [Verma et. al., 1996, Sato et. al., 1993; Hedström et. al., 1993].

When Gallium is incorporated in the $CuInSe_2$ films, the band gap of the resulting material can be changed from 1.0 eV of $CuInSe_2$ to 1.7 eV for $CuGaSe_2$. For a maximum efficiency solar cell, the absorber should have a band gap in the range 1.4 - 1.6 eV [Green, 1982]. Ga incorporation is also believed to improve the adhesion between the $CuInSe_2$ film and the molybdenum electrical back contact [Jensen et. al., 1993]. S incorporation in $CuInSe_2$ film to form a $CuInS_2$ ($E_g = 1.53$) alloy is also another avenue being pursued for improvement in device performance. Recent high efficiency of 17.7 % on small area and 13.9 % on 90.6 cm^2 area sub-modules has strengthened the prospects of $CuInSe_2$ solar cell technology [Tuttle et. al., 1996; Birkmire, 1997].

Commercialization of $CuInSe_2$ based solar cell technology is almost being realized with Siemens Solar Industries (SSI) believed to be leading in this effort. Other companies in the developmental stages are International Solar Energy Technology (ISET), Energy Photovoltaics (EPV) and Solarex Inc. To compete with silicon solar cells, more than 10 % efficiency is required on large areas. SSI have manufactured a 11.2 % efficient prototype module on a 3830 cm^2 area. For successful commercialization, efficiency, material utilization, capital cost and process yields have to be taken into account in realizing this dream. Successful production for commercial $CuInSe_2$ based modules is slow because of the high initial investment and problems associated with $CuInSe_2$ manufacturing. It is believed that SSI obtained $CuInSe_2$ layers by reacting sputtered Cu/In bilayers with H_2Se.

1.4 Basis and Scope of this Work

1.4.1 Motivation

Solid state devices based on copper indium diselenide have produced the highest efficiencies for thin film polycrystalline photovoltaic solar cells. While most efficient $CuInSe_2$ based solar cells have been prepared using co-evaporation process, i.e. vacuum evaporation from three elemental sources, selenization of sputtered Cu/In bilayer shows promise for large scale prospects. Scaling of co-evaporation process for large area deposition of $CuInSe_2$ has several barriers and is energy inefficient [Marudachalam, 1996]. The next challenge for this technology is to bring large scale modules to market. Companies like Siemens Solar Industries (SSI) and International Solar Energy Technology (ISET) thought to be making a breakthrough in commercializing this technology are making $CuInSe_2$ layers by selenizing CuIn bilayers by using H_2Se. Cu and In layers can be sputtered at room temperature on large areas with good uniformity. Selenization of these layers on a large scale appears to be feasible. Due to the toxicity of H_2Se, research efforts are also being focused on selenizing CuIn bilayers by evaporation of elemental selenium.

1.4.2 Statement of the Research Problem

To produce large area commercial devices based on $CuInSe_2$, an understanding of the effect of process parameters on the efficiency of solar cells is very important in determining cost effectiveness. Selenization of CuIn bilayers by H_2Se appears to be the most feasible from an industrial perspective as regards to the compositional uniformity in large areas, deposition control and throughput. Reaction period, reaction temperature and absorber layer thickness are the major process parameters which matter with regard to cost-worthiness in this two-stage process of $CuInSe_2$ thin film

formation. This research is believed to be the first task to systematically quantify the effect of different reaction periods, reaction temperature and absorber layer thickness on the performance of $CuInSe_2$ solar cells.

1.4.3 Objectives of the Research

The objectives of this research were:

- Study of variation of resistivity of metallic Cu and In films with sputtering conditions.

- Study of $CuInSe_2$ thin films prepared by two stage method with reaction period and temperature.

- Study of effect of selenization period on the performance of $CuInSe_2$ based solar cells.

- Study of effect of selenization temperature on the performance of $CuInSe_2$ based solar cells.

- Study of effect of $CuInSe_2$ thickness on the performance of $CuInSe_2$ based solar cells.

1.4.4 Significance and Scope of the Research

This research will provide a fundamental information needed to develop and operate a commercial scale process.

Before sputtering Cu/In bilayers for selenization, one needs to have an idea of the properties of metallic Cu and In films being used. Hence, studies involving the variation of resistivity of Cu and In films with sputtering conditions was done at the Solar Energy Laboratory, University of Dar es Salaam. For different $CuInSe_2$ thicknesses, reaction periods and temperatures in the selenization reactor, solar cells were fabricated using a standard procedure developed at the Institute of Energy Conversion, University of Delaware. J - V data was used to quantify the effect of reaction period, reaction temperature and $CuInSe_2$ thickness on the performance of solar cells. The $CuInSe_2$ thin films were characterized using x-ray diffraction, scanning electron microscopy, energy dispersive spectroscopy and spectrophotometer.

1.5 Thesis Organization

This thesis is organized into five chapters. Part two of chapter 1 gives the literature review. In chapter 2, some of the theory used in this work is given. Experimental methods are highlighted in chapter 3 and the results and analysis are discussed in chapter 4. Conclusion drawn from the investigation is summarized in chapter 5. The cited references and appendices are included at the end of the thesis. Figures and tables are given at the end of each chapter.

PART TWO: LITERATURE REVIEW

1.6 Metallic Films and Precursor Properties

1.6.1 Methods of Fabrication of CuIn Bilayers

Metallic CuIn bilayer films can be deposited by several methods. The most common methods are electrodeposition, electron beam evaporation and DC magnetron sputtering.

Although electrodeposition is commonly used for the deposition of metallic layers over large areas and on complex shapes, the degree of control over thickness and uniformity of the films would likely prevent this technique from being used for the copper and indium deposition. Electron beam deposition has been used successfully to deposit copper and indium layers [Alberts and Swanepoel, 1996]. Others [Basol et. al., 1994] have reported that CuIn bilayers and alloys for the highest quality selenized $CuInSe_2$ were produced by DC magnetron sputtering. Sputtering has also demonstrated scale up, low cost, and a truly in-line sequential process [Gillespie et. al., 1997]. Sections 1.6.1.1 and 1.6.1.1.1 describe briefly the sputtering process.

The principal substrate materials are Mo coated soda lime glass. First a copper film is deposited for good adhesion to the Mo back contact. This is followed by an indium film. Cu and In metallic film thicknesses control the $CuInSe_2$ thickness and the Cu/In ratio.

1.6.1.1 Sputtering

Sputtering is a widely used technique for thin film deposition, both in scientific and industrial work. In many applications, a detailed control of the process parameters is essential in order to achieve films with desired properties. It is well known, for example, that optical and electrical properties are very sensitive to deposition conditions. The required process control can often be achieved in a sputtering system. An additional advantage of the sputtered films is their excellent adhesion to the substrate.

1.6.1.1.1 The Sputter Process

Only a brief discussion of the sputter process will be given in this report. For a thorough treatment, the book by Chapman is recommended [Chapman, 1980). Furthermore, the series "Topics in Physics", [Behrisch, 1981; Behrisch, 1983; Behrisch, 1991] and the books edited by Vossen [Vossen and Kern, 1978] and Glocker[Glocker and Shah, 1995], give detailed information on the subject.

In an evacuated chamber, a working gas is introduced to a pressure in the 10^{-3} mbar range. The working gas is usually inert, i.e., one of the noble gases is used. In practice, argon is the working gas in most systems as it is cheaper.

The target is made of the material that is going to be sputtered, and the substrate is placed a few centimeters away opposite the target. In the simplest version of a sputtering unit, a high potential is set between the target and the substrate, the target serving as cathode and the substrate as anode or ground. The potential must be over the break-down voltage point of the gas. Three steps in the sputter process can be distinguished:

- Electrons are emitted from the cathode and accelerated toward the anode;

- If an argon atom is hit by the electron, it will be ionized and accelerated toward the cathode; after the impact in the target, a secondary electron may be ejected and a self-sustained glow-discharge can be established; and

- With sufficient energy in the impinging argon ion, an atom will be knocked out of the target and sputtering is achieved.

The ejected atoms from the target are usually not ionized, and are consequently not affected by the electric field. The energy of the sputtered atoms is in the range 10 to 30 eV, to be compared with a few tenths of an eV for evaporated atoms. This high energy is conducive to the good adhesion of the sputtered films.

Magnetron systems are more widely used than other sputtering systems such as diode sputtering, triode sputtering, etc, This is mainly due to:

- large deposition rates achievable at low pressures (up to 10^{-3} mbar) due to high current densities;

- low substrate heating; and

- apart from DC (direct current) sputtering, RF (radio frequency) sputtering is also possible.

With magnetron sputtering, the sputtering process can be used in a wide range of applications. The deposition of films by sputtering is influenced by factors such as gas pressure, current, voltage and the anode-cathode geometry.

1.6.2 Metallic Cu and In Films

The use of Cu and In films has increased in recent times especially in the photovoltaic industry where they are used to prepare precursors for selenization to form the chalcopyrite compounds, $CuInSe_2$ and $CuInS_2$. Cu films can also be used in mettalization in Ultra Large Scale integrated Circuits (ULSI) [Musil et. al. 1995, Vinci et. al., 1995] and thin film silicon transistor gate [Sirringhaus et. al., 1997], and solar selective surface application [Craig and Harding, 1981A & B] whereas In films can be used as super conductors [Okuma and Hirai, 1996]. The bulk resistivities of Cu and In are about 1.7 and $8.4 \times 10^{-8}\, \Omega m$, respectively.

Little has been mentioned on electrical and optical properties of metallic Cu and In films by the photovoltaic community. Szot and Prince (1989) mentioned that he used only white In films. Nadenau et. al. (1995) pointed out that Indium layers lead to dense films only if the substrate temperature during deposition is low, preferably below room temperature. Alberts and Swanepoel (1996) observed that Indium deposition temperature is one of the most critical parameters. Parretta et. al. (1992) used RF magnetron sputtering and observed a droplet structure when In was deposited at 75 °C and 100 °C.. It is only Parretta et. al. (1992) who mentioned the resistivity of Cu films as $3 \times 10^{-8}\, \Omega m$. The films were deposited by RF magnetron sputtering at

substrate temperature of 75 °C and magnetron power of 40 W. They did not, however, provide the resistivity of their In films.

1.6.3 CuIn Bilayers

CuIn bilayers have mostly been deposited in the sequence Mo/Cu/In, due to the adhesion problems encountered in the Mo/In/Cu sequence. When In is deposited on a Mo/Cu substrate maintained at room temperature, it exhibits a non uniform morphology which resembles either interconnected islands or separated closely spaced islands. This morphology has been observed when indium was deposited by either evaporation or sputtering. Indium deposited at liquid nitrogen temperatures exhibits a smooth structure, due to the reduced mobility of In surface atoms to diffuse to form islands [Dittrich et. al, 1988]. A thin layer of tellurium on Cu or Mo apparently causes In to deposit as a smooth film at room temperature [Basol et. al., 1993].

The phases formed in the as-deposited precursors and annealed precursors are important to the understanding of the kinetics of $CuInSe_2$ film formation. The phase diagram for the Cu-In system is shown in figure 1.2. The equilibrium phases are the liquid phase, L_p, the terminal solid solution α_p of Cu with maximum solubility of 10.9 atomic percent In, β_p phase with a homogeneity range of 27.7 to 31.3 atomic percent In, γ_p phase with a homogeneity range of 27.7 to 31.3 atomic percent In, δ_p phase with a homogeneity range of 28.9 to 30.6 atomic percent In, η_p phase in the composition range of 33 to 39 atomic percent In, $Cu_{11}In_9$ occurring at $\approx$ 45 atomic percent In and the terminal solid solution of In with very little or no Cu dissolved in

In. There are several intermediate phases in the composition range between 34 and 38 atomic percent In.

In the Cu-In bilayer deposited at room temperature by electron beam evaporation the phases observed were Cu, In, and $CuIn_2$. Annealing of these films results in the formation of a $Cu_{11}In_9$ phase and an In phase [Verma, 1993]. The $CuIn_2$ phase is a metastable phase. However, Gupta et. al. (1994) observed Cu, In, Cu_4In and Cu_7In_4 phases when they deposited Cu and In layers at room temperature by thermal evaporation. Annealing of these films in vacuum at 150 °C for 40 minutes preserved the phases observed but the amount of Cu_4In increased. Annealing at 200 °C for 15 minutes increased the amount of Cu_7In_4. When Cu and In is deposited at 200 °C, $Cu_{11}In_9$ is the only phase observed. The final quality of $CuInSe_2$ films was also found to be dependent on the deposition temperature of the Cu and In layers [Gupta et. al., 1994].

1.7 Properties of $CuInSe_2$

1.7.1 Optical Properties

$CuInSe_2$ is direct band gap material. Its band gap is 1.02 ± 0.01 eV at room temperature, and has a temperature coefficient of $-2 \pm 1 \times 10^{-4}$ eV/K in the lower temperature regime [Rincón and Gonzalez, 1986]. The typical absorption coefficient is larger than 5×10^4 cm^{-1} at photon energies greater than 1.4 eV. The band gap of $CuInSe_2$ can be modified continuously over a wide range by substituting Ga and S for

In and Se, respectively. Recent trends in CuInSe$_2$ research and development focus exclusively on these high band-gap alloys (Birkmire and Eser, 1997].

1.7.2 Electrical Properties

Electronic properties of CuInSe$_2$ are controlled largely by the intrinsic defect chemistry of the material. In general, the defect chemistry is complex; however, within ± 2 at. % of the stoichiometric composition, various analyses of single crystal. [Neumann and Tomlinson, 1990] and thin films [Noufi R. and Powell R., 1985] give a relatively coherent model of defect chemistry. Cu and In vacancies (excess Se), which are acceptors, yield strongly p-type material. In contrast, Se vacancies produce n-type material. Along or near the pseudo-binary tie Cu$_2$Se-In$_2$Se$_3$, In-rich material have both In-on-Cu (In$_{Cu}$) antisite donor defects and Cu vacancy acceptors, resulting in heavily compensated n- or p-type material. In the case of excess Cu, dominant defects are Cu-on-In (CuIn) antisite and In vacancy acceptors, which both contribute to a strongly p-type material. Mobilities determined by temperature-dependent transport measurements performed on single crystals [Neumann and Tomlinson, 1990] were 15 to 150 cm^{2}V^{-1}s^{-1} for p-type materials with carrier densities 0.15 to 2 × 10^{17} cm^{-3} at 300 K. For n-type materials, sample mobilities were 90 to 900 cm^{2}V^{-1} s^{-1}, while carrier densities varied from 1.8 × 10^{15} to 5 × 10^{17} cm^{-3} at 300 K. No correlations were found among carrier densities, mobilities, and composition.

Electronic transport in CuInSe$_2$ and related alloys is dominated by intrinsic defects with heavy self-compensation [Birkmire and Eser, 1997]. Polycrystalline thin films of CuInSe$_2$ can be used as absorbers in PV devices because their electronic transport is

dominated by such defect structure. CuInSe$_2$ grain boundaries, which are parallel to the current-flow direction in these devices, can easily be modified electronically by dopants such as oxygen, and by low-temperature post processing heat treatments, without affecting the bulk chemistry. As a result, grain boundaries can be made more p-type and thus are electronically benign since minority carries (i.e. electrons) cannot reach the grain boundaries to recombine.

1.8 Methods for Deposition of CuInSe$_2$ Film

Copper indium diselenide was first synthesized in 1953 [Hahn et. al., 1953]. Since then, a variety of methods have been developed for deposition of CuInSe$_2$ based absorbers. The methods can be divided into two major categories:

- 1) those processes where the metals are delivered separately from Se and

- 2) those processes where Se is incorporated with the metals during material delivery.

Both these processes will require thermal activation in Se. Examples of case 2 are co-evaporation of the three elements in vacuum [Pal et. al., 1994], electrodeposition [Pern et. al., 1991], chemical dipping [Garg et. al., 1988], CVD [Philip et. al., 1994], spray pyrolysis [Mooney and Lamoreaux, 1986], sputtering [Devaney and Mickelson, 1986; Rockett et. al., 1988; Sammann et. al., 1980; Thornton et. al., 1988], etc. Thermal mixing of stacked binary or elemental layers [Sachan and Meakin, 1993], selenization of Cu-In alloy using H$_2$Se [Kumar et. al., 1992] or selenium [Lakshmikumar and Rastogi, 1994 ;Yamanaka et. al., 1993] are examples of case

one. Of these deposition methods, the films produced by selenization of CuIn alloy using H_2Se is the most compatible with large scale production.

Control of film stoichiometry and uniformity are the critical factors for obtaining high quality $CuInSe_2$ films needed for making high efficiency solar cells, and these factors depend on the deposition process. Factors which affect the process selection are the degree of control the process offers, material utilization, capital equipment costs and scalability prospects. The most efficient $CuInSe_2$ based solar cells have been fabricated by co-evaporation from elemental sources and selenization of precursor films [Rocket and Birkmire, 1991]. Efficiencies between 16 and 18 % for co-evaporated [Hedström et. al., 1993; Tuttle et. al., 1996] , and between 12 and 14 % for selenization of precursors [Gay et. al., 1994; Marudachalam et. al., 1995; and Verma et. al., 1996] have been achieved.

1.8.1 Co-evaporation from Elemental Sources

Co-evaporation has consistently produced cells with the highest efficiencies since its popularization in 1982 by a group at Boeing when they were able to fabricate a 11% efficient $CuInSe_2$/CdS solar cell [Mickelsen and Chen, 1982]. In this technique, the composition of the evaporated flux is continuously adjusted from highly copper-rich to highly indium-rich during the growth period. High vacuum evaporation systems with open boats or effusion cells are usually used and the fluxes are controlled by electron impact emission spectroscopy, and thermally controlled effusion sources. The advantage of this method is the ability to adjust and control the elemental fluxes and substrate temperatures throughout the film deposition. $CuInSe_2$ films prepared by this approach display the large grain size of a copper-rich material with the desirable electronic properties of the indium-rich compound [Gabor, 1995].

The "Boeing recipe" was two $CuInSe_2$ layers deposited on Molybdenum-coated glass substrates. The first layer was typically 2 μm thick, deposited at 350 °C, with an average composition of approximately 26 at. % copper, 25 at. % indium, and 49 at. % selenium. This layer has large grains and a low resistivity, consistent with the copper-rich composition. The second layer was 1 μm thick grown at 450 °C with a typical average composition of 21 at. % copper, 28 at. % indium, and 51 at. % selenium. Diffusion during growth mixes the two layers completely forming a near-stoichiometric film through the depth of the film with 24 at. % copper, 26 at. % In, and 50 at. % selenium. The resulting material has larger grains than a single-layer film of comparable composition that may be necessary for good device performance [Mickelsen and Chen, 1981].

Although simultaneous evaporation from four elemental sources has produced the highest total area device efficiency of 17.7 %, the scale up of evaporation has been questioned regarding such issues as material utilization, composition uniformity in large areas, deposition control, and throughput [Gillespie et. al., 1997].

1.8.2 Selenization Process

Selenization is a versatile two-stage technique for fabricating thin film $CuInSe_2$ layers. In this approach, sequential layers of copper and indium (and sometimes selenium) are deposited on a molybdenum coated soda lime glass substrate. This elemental stack is exposed to a Se environment, either a dilute H_2Se gas mixture or Se vapor at about 10^{-6} mbar, at temperatures close to 400 °C to convert the elemental stack to $CuInSe_2$. Selenization using Se vapor as the chalcogenide source is generally preferred to using

H$_2$Se gas. The driving force behind this idea is due to toxicity of the latter, which presents not only high security costs, but also an environmental risk factor (Dimmler et. al., 1991). For large scale industrial production, H$_2$Se may be more appropriate.

Single phase device quality CuInSe$_2$ has been reported by a number of groups which included Siemens Solar Industries (SSI), Institute of Energy Conversion (IEC), International Solar Electric Technology (ISET), and National Renewable Energy Laboratory (NREL). The claimed advantages to this approach are:

- greater process control due to the sequential deposition of the source materials;

- greater freedom in the choice of the separate deposition techniques enabling processes more adapted to large area, low cost considerations; and

- the potential for higher "quality" of the final material due to the thermodynamic equilibrium of the process [Sato et. al., 1993; Basol and Kapur, 1990].

The Cu-In bilayers may be deposited by electrodeposition, evaporation and sputtering.

Reactors used in selenization differ in the delivery of the reacting species, the starting precursor and the temperature time profile in the growing film. These reactor systems are summarized below:

- Physical Vapor Deposition (PVD) Reactors:

    Direct line of sight delivery of the reacting species to the substrate in three or four source (gallium) reactors has been extensively studied. The highest efficiency devices have been produced in such reactors [Tuttle et. al., 1995; Hedstrom et. al., 1993; Sharfarman et. al., 1996]. Reactor temperature can be varied from 350

to 550 °C during absorber preparation. Copper and Indium layers can also be selenized in a PVD reactor using a single selenium source [Birkmire, 1993].

- Rapid Thermal Processing (RTP) Reactor:

In this method of producing copper indium diselenide, elemental copper, indium(gallium) and selenium are deposited at room temperature by various methods and the stack is then very rapidly heated to over 500 °C and reacted [Probst et. al., 1996].

- Chemical Vapor Deposition(CVD) Reactors:

Successful devices of efficiencies between 12 and 14 % have been achieved in CVD reactors using H_2Se to selenize copper indium layers [Gay et. al., 1994; Marudachalam et. al., 1995].

1.8.2.1 Diffusion and Reaction Kinetics for $CuInSe_2$ Film Growth

The growth of film in the selenization reactor is controlled by diffusion and reaction kinetics.

1.8.2.1.1. Diffusion

Interdiffusion and diffusion in thin films are basically similar to processes occurring in bulk specimens. The geometry of thin films and the presence of numerous defects, in comparison with bulk materials, induced during processing, makes diffusion in thin films a complicated field of study [Philibert, 1991]. Diffusion in thin films can be

observed at temperatures well below those at which equilibrium vacancy diffusion is negligible [Hall and Morabito, 1976]. Structural defects which influence self and impurity diffusion through thin films include grain boundaries, dislocations and vacancies.

Grain boundaries are surface or area defects that constitute the interface between grains of different crystallographic orientation. The atoms on the grain boundary are as energetic as the atoms on the film surface and various atomic phenomenon such as diffusion are accelerated. The fraction of atoms associated with grain boundaries is roughly $3a_{ad}/l$ where a is the atomic dimension and l is the grain size [Ohring, 1992].

Dislocations may be viewed as line defects that bear a definite crystallographic relationship to the lattice. There are two basic kinds of dislocations: edge and screw. The edge dislocation requires displacement of a plane in the perfect crystal lattice. Dislocations can be sites for charge recombination or generation as a result of uncompensated dangling bonds. Diffusion, film stress and thermally induced mechanical relaxation processes are strongly influenced by dislocations.

Vacancies are point defects that arise when lattice sites are unoccupied by atoms. Vacancies are formed as the energy required to displace an atom from the lattice to the surface, E_T, is not particularly high. Additionally, the increase in system disorder or entropy due to mixing of vacancies among lattice sites gives rise to a thermodynamic probability that a fraction f, of the total number of sites will be unoccupied at any temperature, T.

To illustrate diffusion in thin films, consider a highly idealized polycrystalline thin film shown in figure 1.3. The film contains square grains of size l, grain boundaries of

thickness δ, and dislocations with an area of cross section A_d, which thread through

the lattice with density ρ_d per square centimeters. If we choose our control volume as

the entire thin film surface, then the incoming flux of atoms on the film surface may

either diffuse through the film lattice, the grain boundaries or the dislocations. The

individual fluxes can be expressed as the product of the appropriate diffusion

coefficient with the concentration gradient.

1.8.2.1.2 Reaction Kinetics

Recent efforts in copper indium diselenide solar cell research have been focused

toward understanding the reaction kinetics for the selenization of copper/indium

precursor films. The information is necessary because:

- a complete understanding of the reaction pathways can be used to modify the

   absorber layer properties for maximum cell efficiency; and

- the information can be used in design and operation of large scale solar panel

   manufacturing equipment.

An early study of the reaction kinetics indicated that the compounds, Cu_2Se and In_2Se_3

are formed first. These compounds then react to form chalcopyrite $CuInSe_2$. The

films were analyzed using x-ray diffraction and electron microprobe. Three methods

of selenium delivery were mentioned:

- selenization from elemental selenium in a closed ampoule;

- transport of elemental selenium with Ar in an open system; and

- selenization from a solid/liquid selenium source in a Cu/In/Se sandwich

Distinctions among the behaviors of these delivery systems were not discussed, and the temperature profiles of the reacting films were not specified [Dimmler et. al., 1988].

Time dependent studies for $CuInSe_2$ formation has been carried out using the following reactor systems:

- reactive thermal annealing of stacked layers of Cu-In-Se [Dittrich et. al., 1988];

- Cu-In bilayer selenization in a CVD reactor [Orbey et. al., 1997; Verma et. al., 1996; Verma, 1993];

- Cu-In bilayer selenization in a single source PVD reactor [Orbey et. al., 1998]

Stacked layers of Cu-In-Se deposited by evaporation were used in the reactive annealing system. An excess of selenium was used to compensate for re-evaporation from the film. The films were then annealed at a temperature of 500 °C in an argon atmosphere. Hold times were 2, 6, 10, 15, and 20 minutes, with a heating rate of 5 °C per minute and a cooling rate of 20 °C per minute. The phases identified using x-ray diffraction are shown in table 1.1

Both experimental and theoretical work using CVD and PVD reactor systems has been carried out. Pertinent chemical species which take part in the reaction to form $CuInSe_2$

layers were identified and comparing mass balance equations predictions with species compositions at various times, reaction rate expressions for each reaction rate constant were obtained. CuIn bilayers deposited by evaporation on Molybdenum coated soda lime glass were used in the time dependent studies. The CuIn bilayers were annealed at 150 °C in an inert Ar atmosphere for 20 to 30 minutes prior to selenization. The selenized samples were analyzed using x-ray diffraction and atomic absorption spectroscopy to identify phases and estimate the relative mole fraction of the identified phases. Details of the methodology followed using the both CVD and PVD reactor are described elsewhere [Verma et. al., (1996); Orbey et. al.(1997); Orbey et. al. (1998)]. The phases identified for different reaction periods are shown in tables 1.2 and 1.3.

1.8.2.2 IEC CVD Reactor for Selenization

The CVD reactor at IEC was designed and constructed by Varin (1991) and modified by Verma (1993) for safe production of $CuInSe_2$ by reaction of Cu-In bilayers in the presence of H_2Se at elevated temperatures. A schematic diagram of the entire selenization system is given in chapter 3 (figure 3.2). The operating procedures, developed over a period of more than a year, took into account the use of the extremely toxic H_2Se gas and concerns on the effect of the gaseous impurities like H_2O and O_2. The selenization reactor to the best of our knowledge is the only existing system which is so versatile in its capabilities of:

- being able to pump down to pressures less than 10^{-6} mbar effectively removing the gaseous impurities;

- having the ability to do short time experiments with the push-pull feed through;

- exploring a series of experiments schemes which require time-temperature ramp/soak profiles; and

- having the ability to isolate the effect of O_2 on the thin film and H_2Se pyrolysis properties.

A quartz tube (50.8 mm in diameter and 750 mm long) with a heating jacket accommodates a substrate holder for Cu-In bilayers. When H_2Se gas enters the heated quartz tube, the H_2Se dissociates according to the following chemical reaction [Verma et. al., 1991]:

$$x \; H_2Se \; (g) \quad \leftrightarrow \; x \; H_2 \; (g) + Se_x \; (g) \qquad\qquad\qquad (\; 1.1 \;)$$

where x is 1, 2, 3, 5, 6 and 7.

Gas phase analysis established that the reacting selenium gas-phase species could be either H_2Se or one of the Se_x species [Verma et. al., 1992]. Both the H_2Se and Se_x adsorbed from the gas phase dissociate on the film surface to form selenium species.

Preliminary studies using the reactor showed that high efficiency solar cells could not be made on $CuInSe_2$ films using only H_2Se as the reacting gas. However, by mixing O_2 with H_2Se, $CuInSe_2$ was formed and cells with efficiencies over 10 % were fabricated [Verma et. al., 1993]. It was postulated that oxygen reacts with the H_2Se in the gas phase forming Se_x according to the following reaction:

$$H_2Se + O_2 \rightarrow H_2O + (1/x)\,Se_x \hspace{4cm} (1.2)$$

Quantitative data by Verma et. al. (1993) show that excess selenium is available for reaction when the gas mixture contains oxygen. This result was confirmed by experimental observation of the selenium deposited on the reactor walls in the presence of oxygen and by no deposition in the oxygen free experiments.

Ramp up to desired reaction temperature in the presence of O_2 was also found to prevent the bilayer segregation on the molybdenum [Verma et. al., 1993]. This is probably due to formation of a surface indium oxide film. The presence of an indium oxide film was confirmed by Auger electron Spectroscopy at the NREL [Kazmerski L., ref. 5 in Verma et. al., 1993].

1.9 CuInSe₂ Based Solar Cells and Fabrication

Chalcopyrite films of $CuInSe_2$ are well known as highly efficient absorbers for thin film solar cells. Devices based on $CuInSe_2$/CdS/ZnO have already demonstrated terrestrial active area conversion efficiencies of 17.7 % [Tuttle et. al., 1996]. The great potential of $CuInSe_2$ for solar energy conversion is due to its direct band gap (1.02 eV), high absorption coefficient, good thermal, environmental and electrical stability, and the existence of a variety of potential low cost methods for its preparation. Preliminary tests also indicated that the radiation tolerance of $CuInSe_2$ thin films is superior to that of single-crystalline Si or GaAs devices when tested under high energy electron and proton radiation (Mickelson et. al., 1985). Besides their stability and high efficiency $CuInSe_2$, thin films also offer to the space market, high specific power and low cost (Basol et. al., 1993).

In general form, the most recent structure for $CuInSe_2$ based solar cells is shown in figure 1.4. The structure incorporates three important variations [Birkmire and Eser, 1997]:

- to retain proper junction characteristics and at the same time reduce absorption and resistive losses, the CdS buffer layer thickness must be reduced to 0.05 μm and an n-type ZnO window layer must be added onto the CdS;

- partial substitution of In with Ga and S with Se can improve efficiency because the higher band gap gives a better match to the solar spectrum;

- further improvements are obtained by incorporating Na into the $CuInSe_2$ layer, although the role Na plays in improving device efficiencies is not well known [Basol et. al., 1994; Probst et. al., 1995]. Soda lime glass used as substrate provides a practical, though uncontrollable, source of Na since at the process temperatures used, Na diffuses through the Mo layer into the $CuInSe_2$ film.

The typical substrate for high efficiency terrestrial $CuInSe_2$ solar cell is Mo coated soda lime glass. Mo is preferred as contact material because it does not chemically interfere with the growing film at the processing temperatures. However, the quality of the $CuInSe_2$ film (i.e. morphology, grain size and orientation) is directly affected by the quality of the underlying Mo layer. If deposited under sub-optimized conditions, the Mo layer exhibits either tensile or compressional stresses which contribute to the commonly observed peeling of the $CuInSe_2$ films at the $CuInSe_2$/Mo interface.

The key component of the thin film solar cell is the $CuInSe_2$ absorber layer. Methods for preparation of $CuInSe_2$ were discussed in section 1.8. Regardless of the deposition process used, it has been reported that the morphology and grain orientation of $CuInSe_2$ thin films depend strongly upon Cu-In atomic ratio in the films (Walter et. al., 1992). Stoichiometric and Cu-rich films exhibit a rough appearance, whereas In-rich samples have smooth and shiny surfaces. The coarse grained morphology of Cu-rich films is desirable because large grain crystallites lead to smaller contact interface areas and thus a fewer grain boundaries. In addition Transmission Electron Microscopy (TEM) studies have shown that these films are also superior with respect to internal defects such as microtwins and stacking faults (Kiely et. al., 1991). The change in morphology as a function of the Cu-In atomic ratio is also accompanied by a change in orientation of the films. Stoichiometric and Cu-rich films exhibit a pronounced 112 orientation, whereas In-rich films are characterized by (220/204) oriented grains (Walter et. al., 1992).

In order to match the p-type absorber ($CuInSe_2$) and the n-type window (ZnO), a thin (30 - 50 nm) CdS buffer layer is required [Walter and Schock, 1996]. The CdS buffer layer is lattice and electronically matched to $CuInSe_2$, and has a significant higher spectral response in the blue region. The chemical bath deposition (CBD) technique is the preferred method for depositing CdS films of approximately 0.05 μm thick. This technique, which involves dipping the sample in an ammonia solution containing $CdSO_4$ and thiourea [Doña and Herrero, (1992)] gives deposition rates on the order of 0.06 μm/min. The primary advantage of the CBD method is that it gives almost complete surface coverage even at low thicknesses. Other vacuum deposition techniques would require higher thicknesses to obtain complete surface coverage. However, because of environmental concerns related to cadmium, research effort are

being directed toward either finding a replacement for CdS buffer layer or making direct rectifying contact with ZnO [Velthaus et. al., 1993; Hariskos et. al., 1994; Kessler et. al., 1994]. However, at present time, highest efficiencies are still obtained using CdS buffer layer deposited by CBD.

ZnO is the ideal material as n-type window layer due to its wide band gap (3.2 eV), high temperature stability and the fact that it can be doped in any desired order. In order to optimize the $CuInSe_2$/ZnO heterojunction, it is performed most commonly by room temperature sputtering in two steps. A 100 to 500 Å highly resistive (sheet resistance in the order of 10^6 Ω/sq.) ZnO film is deposited first, followed by a 0.1 to 2 μm highly conductive (sheet resistance $\approx$ 10 to 15 Ω/sq.) film. The deposition rates are approximately 0.05 μm/min.

Finally, as a front contact an Al grid of about 1 μm thick is evaporated onto the ZnO window layer. A thin Ni layer can be used between the ZnO and Al to prevent oxidation of Al as well as reduce resistive losses between the semiconductor / metal contacts.

2.0. Solar Cell Results using the IEC CVD Reactor

IEC data base for most of the $CuInSe_2$ solar cells fabricated by different workers since 1990 using the chemical vapor deposition reactor shows solar cells with efficiencies as high as 12 %. Most of these results were obtained in the process of finding the optimum operating parameters of the CVD system to obtain good device performance. Except for absorber thickness which was maintained constant at about 2 μm, reaction

period, reaction temperature, H_2Se and O_2 concentration, procedures and post treatment have been varied. Analysis of good device performance solar cells gave a general pattern for reaction period versus efficiencies (Figure 1.5). However, it is difficult to make a confident conclusion as the data was not systematic as shown in table 1.4. The reaction period, H_2Se concentration, and O_2 concentration changed from 20 to 90 minutes, 0.35 to 2.6 % and 0.01 to 0.4 %, respectively. The present research is aimed at giving us systematic data on the effect of reaction period, reaction temperature and absorber thickness on the performance of $CuInSe_2$ solar cells. This information is very useful for design of commercial scale CVD reactor for selenization.

Table 1.1.   Phases identified in the reactive thermal annealing study [Dittrich et. al., 1988]

Reaction period (min.)	Identified phases
2	Se, In, CuIn
6	InSe, $Cu_{2-x}Se$, $CuInSe_2$
10	$CuInSe_2$
15	$CuInSe_2$
20	$CuInSe_2$

Table 1.2. Copper-indium bilayer selenization in single source PVD reactor at 400 °C: Summary of XRD results [Orbey et. al, 1998]

Time (min)	Phases Observed		
	metals	selenides	ternary selenides
0.5	Cu_xIn_y, In	In_2Se	
1	Cu_xIn_y, In	In_2Se, Inse	
2	Cu_xIn_y	In_2Se, Inse	$CuInSe_2$
5	Cu_xIn_y	In_2Se, Inse	$CuInSe_2$
10	Cu_xIn_y	In_2Se, Inse	$CuInSe_2$
20		InSe	$CuInSe_2$
30		InSe	$CuInSe_2$

Table 1.3. Species observed in copper-indium bilayer selenization in the CVD reactor: Summary of XRD results [Orbey et. al., 1997; Verma et. al., 1996; Verma, 1993]

Time (min)	Phases Observed		
	metals	selenides	ternary selenides
(a) T = 250°C			
5	Cu_xIn_y	In_2Se	
10	Cu_xIn_y	In_2Se, InSe	
25	Cu_xIn_y	In_2Se, InSe	$CuInSe_2$
30	Cu_xIn_y	In_2Se, InSe	$CuInSe_2$
45	Cu_xIn_y	In_2Se, InSe	$CuInSe_2$
60	Cu_xIn_y	In_2Se, InSe	$CuInSe_2$
90	Cu_xIn_y	In_2Se, InSe	$CuInSe_2$
120	Cu_xIn_y	In_2Se, InSe	$CuInSe_2$
(b) T = 325°C			
2	Cu_xIn_y	In_2Se, InSe	
5	Cu_xIn_y	In_2Se, InSe	
10	Cu_xIn_y	In_2Se, InSe	$CuInSe_2$
20	Cu_xIn_y	In_2Se, InSe	$CuInSe_2$
30	Cu_xIn_y	InSe	$CuInSe_2$
45	Cu_xIn_y	InSe	$CuInSe_2$
65	Cu_xIn_y	InSe	$CuInSe_2$
90	Cu_xIn_y	InSe	$CuInSe_2$
(c) T = 400°C			
1	$Cu_{11}In_9$, In	In_2Se	
2	$Cu_{11}In_9$	In_2Se, Inse	$CuInSe_2$
5	$Cu_{11}In_9$	In_2Se, Inse	$CuInSe_2$
10		Inse	$CuInSe_2$
15		Inse	$CuInSe_2$
30		Inse	$CuInSe_2$
45			$CuInSe_2$

Table 1.4. Preparation conditions for selected CuInSe$_2$ samples whose solar cell efficiencies are shown in Fig. 1.5 [Russel, 1998]

No.	Sample	η	reaction period (min)	H$_2$Se (%)	Reaction Temp. (°C)	V$_{oc}$ (V)	J$_{sc}$ (mA/cm^2)	FF	O$_2$ (%)	other
1	89162-1	9.69	60	0.35	410	0.4084	34.63	59.9	0.01	post HT(30min)/KCN etch
2	89163-1	11.07	90	0.35	410	0.4353	34.71	64.1	0.01	longer rct time
3	81111-1	9.98	45	2.6	400	0.3921	33.38	66.7		post anneal(10 min)
4	81124-4	9.93	45	2.6	400					
5	81110-2	7.63	45	2.6	400	0.3941	32.5	52.2		
6	81076-1	7.89	45	1.5	400	0.35	32.82	60.1		
7	81120-2	8.09	45	2.6	400	0.365	32.74	59.3		
8	81072-1	3.25	20	1.1	400	0.3717	26.14	29.3		shorter rct time
9	91034	5.33	30	3.4	462				none	slow cool down.intermediate hold@300°C B4 final Se at 462°C
10	91091	9.58	60	1.7	412				0.4	KCN etch
11	91095	9.25	60	1.7	412				0.4	KCN etch/30 min Ar
12	H$_2$Se-CVD-521	11.95	90	0.25		0.4725	35.47	71.3		longer rct time
13	H$_2$Se-CVD-514	11.33	90	0.35		0.4788	33.35	70.9		longer rct time
14	H$_2$Se-CVD-515	10.44	90	0.35		0.4783	34.01	64.2		longer rct time
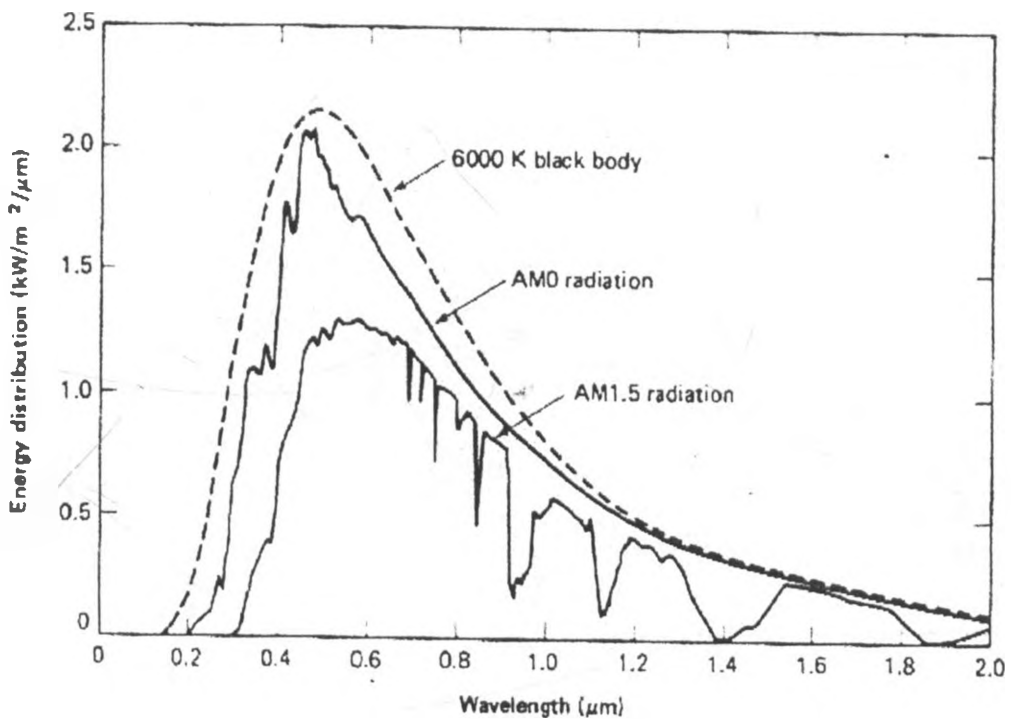
Figure 1.1. Spectral distribution of sunlight. Shown are the cases of AM0 and AM1.5 radiation together with the radiation distribution expected from the sun if it were a black body at 6000 K [Green, 1982].
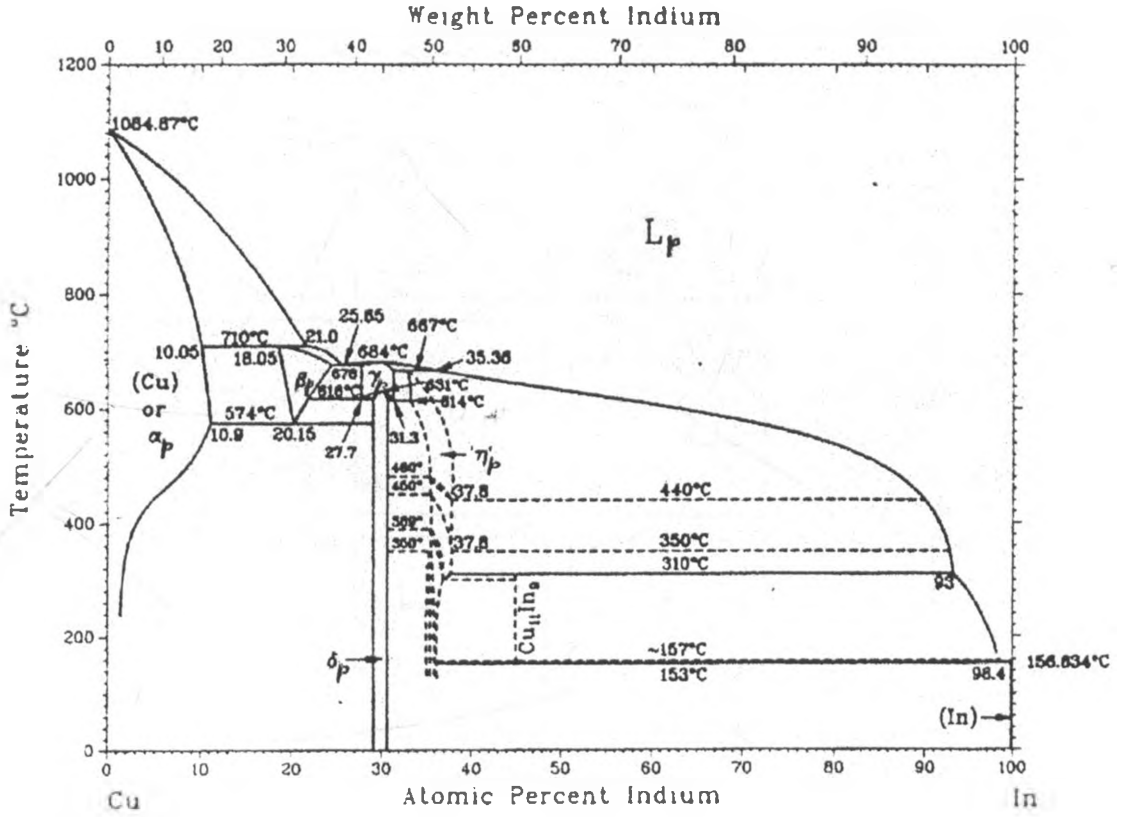
Figure 1.2. Phase diagram of the Cu-In system [Subramanian and Laughlin, 1989].
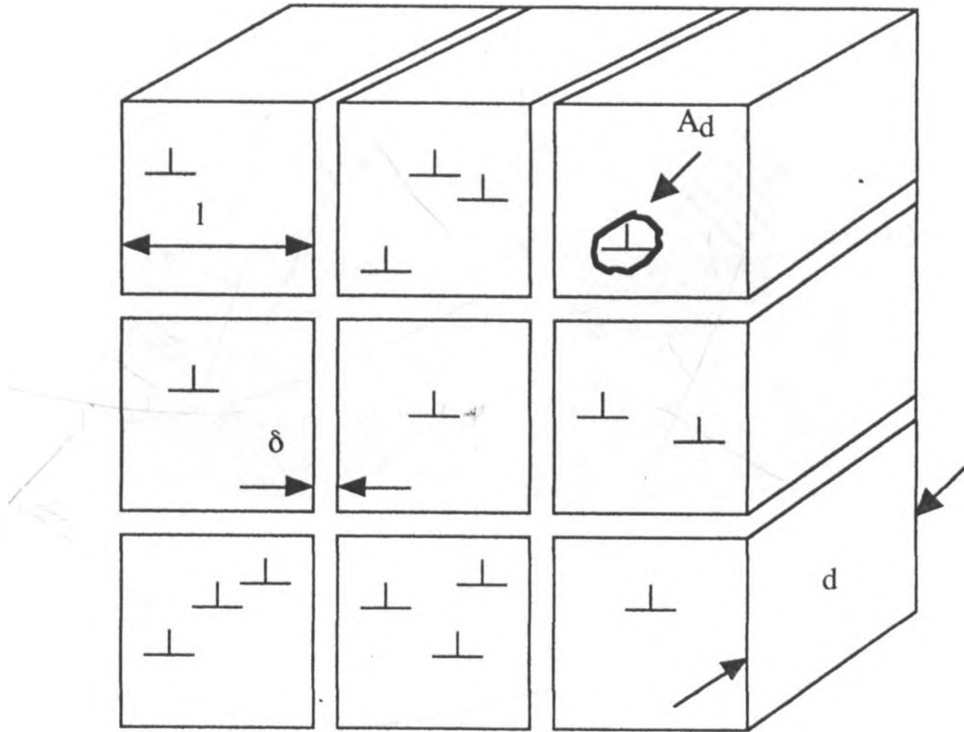
Figure 1.3. Highly idealized polycrystalline film containing square grains, grain boundaries and dislocations.
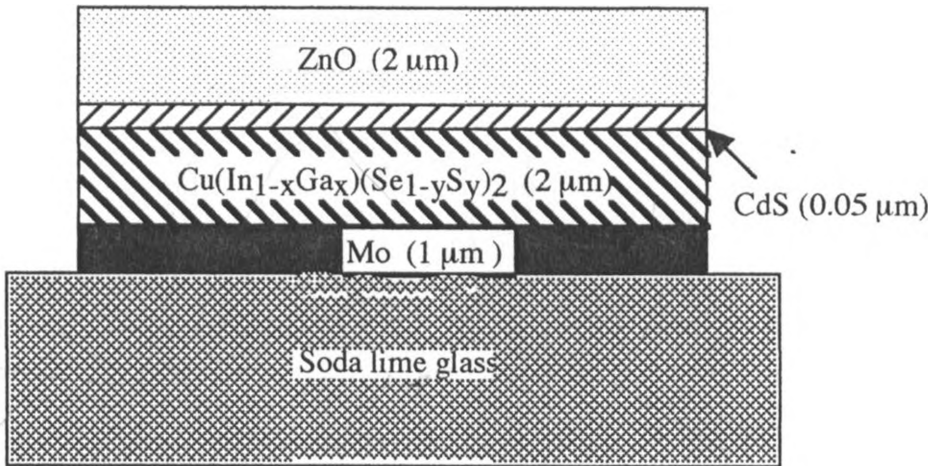
Figure 1.4. Typical structure of CuInSe$_2$-based solar cell [Birkmire and Eser, 1997].
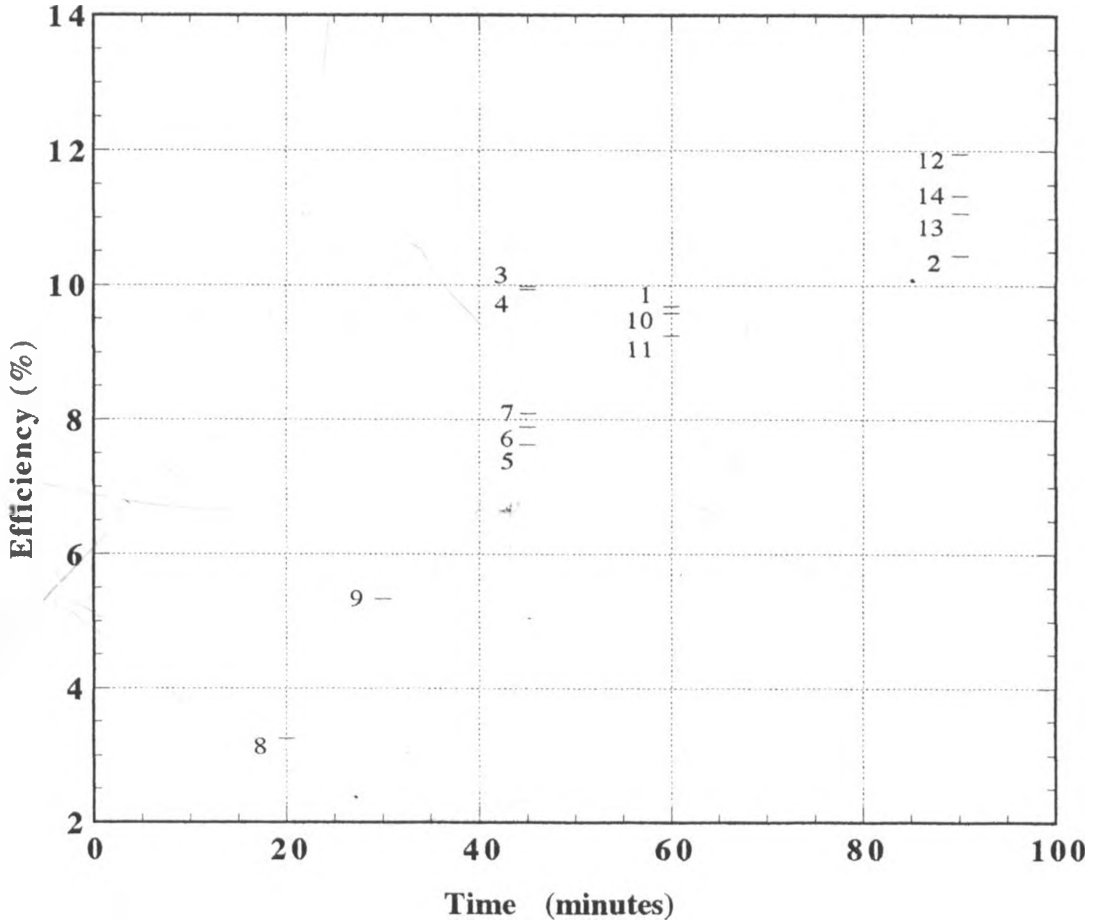
Figure 1.5. Efficiencies with reaction period for selected solar cells fabricated using IEC's CVD reactor. The numbers represent corresponding sample preparation conditions and results as given in table 1.4.

CHAPTER TWO

THEORY

2.1 CuInSe$_2$ Crystal Structure

CuInSe$_2$ belongs to the chalcopyrite form, a subset of the adamantine class. Normal adamantine structures have geometrical features of a wurtzite or zinc-blende or stacking variations of them [Parthe, 1967]. The lattice parameters of CuInSe$_2$ along with other physical properties are shown in table 2.1. Its crystal structure is shown in figure 2.1.

In the chalcopyrite compounds, the slight shift of the anionic sites results in tetragonal symmetry with the c-axis essentially twice the original cubic axis. The tetragonal crystal structure results from stacking of two zinc-blende structures along the z-axis. CuInSe$_2$ crystallizes in this form at room temperature and reverts to sphalerite above 800 °C.

2.2 CuInSe$_2$ Phase Diagrams

Phase diagrams can be used in predicting and identifying precursors, intermediates and final products formed.

There is little information on the Cu-In-Se ternary phase diagrams. It is difficult to produce the single crystal CuInSe$_2$ necessary for characterization of phases as:

- CuInSe$_2$ is not a congruently melting compound,

- the presence of chalcopyrite-sphalerite phase transition hinders the production of large crack-free crystals, and

- differential external expansion produces strained crystals, and even crystals possessing microcracks.

The available phase information is largely limited to the Cu_2Se-In_2Se_3 pseudo-binary, first studied in 1967 [Palatnik and Rogachera ,1967]. Their research indicate that considerable range of off-stoichiometry existed on the Indium-rich side of the stoichiometric $CuInSe_2$. However, they incorrectly identified the melting of $CuInSe_2$ to be congruent as several crystal growth experiments since have reported a non-homogeneous composition along directionally frozen ingots. They identified the sphalerite-chalcopyrite transition temperature as 810 °C. The pseudo-binary phase diagram for $CuInSe_2$ is shown in figure 2.2.

The sphalerite phase is stable only at temperatures higher than 570 °C, whereas the chalcopyrite structure is stable from room temperature up to 810 °C. However, below 780 °C the stability region of the chalcopyrite phase is on the indium-rich side of perfect stoichiometry. The chalcopyrite phase is also retained in the direction of excess Se, although deviation from stoichiometry toward excess Cu results in the formation of secondary Cu_2Se phase.

2.3 Model Equations for CuInSe₂ Film Growth during Selenization

A brief discussion on model development for $CuInSe_2$ film growth during selenization will be given in this section. Detailed treatment is given elsewhere [Orbey et. al.,

1997; Verma et. al., 1996]. The reaction pathway leading to the formation of $CuInSe_2$ includes two phases - liquid phase In with dissolved Cu, and solid Cu-In phase ($Cu_{11}In_9$) - in the initial film structure (i.e. when Se delivery begins). This is presented in table 2.2. The simplified assumptions used in model development are:

- The mass transfer from the gas phase is not the controlling mechanism;

- Selenium diffusion is fast;

- Selenium is in large excess and hence its concentration in the growing film is constant;

- No spatial variations of species compositions in the growing film;

For the growing film control volume (figure 2.3), the mass balance for any i^{th} species may be expressed as

$$\frac{dn_i}{dt} = r_d(i) - r_r(i) + r_{rxn}(i)V_f \tag{2.1}$$

where $r_d(i)$ is the rate of delivery of species i to the film (mol min^{-1}), $r_r(i)$ is the rate of removal of species I (mol min^{-1}), n_i is the number of moles, $r_{rxn}(i)$ is the rate of reaction of the ith species (mol min^{-1} cm^{-3}), t, is the time of reaction and V_f is the film volume (cm^3). For all the species except selenium, the rate of delivery is zero. The rate of removal is also zero for all the species except In_2Se, which may have sufficient vapor pressure at typical selenization temperatures to evaporate. Considering the amount of evaporated In_2Se to be negligible (this may not be the case for different reaction condition), Equation (2.1) for In, In_2Se, InSe, $Cu_{11}In_9$, Cu_2Se and $CuInSe_2$ reduces to

$$\frac{d([i]V_f)}{dt} = r_{rxn}(i)V_f \tag{2.2}$$

Equation (2.2) must be combined with the reaction rate expressions for each species. As an example, considering the depletion of In $(2In + Se \rightarrow In_2Se, k_2)$ to be first order, the following rate expression is assumed

$$r_{rxn}(In) = -2k_2[Se][In] \tag{2.3}$$

where k_2 is the reaction rate constant for In species.

Designating the reactant selenium species in the growing film as 'Se' to represent any selenium species which may be present, for Se, equation (2.1) becomes

$$\frac{d([Se]V_f)}{dt} = r_d(Se) + r_{rxn}(Se)V_f \tag{2.4}$$

The overall mass balance equation for the growing film is

$$\frac{d(\rho_f V_f)}{dt} = r_d(Se)MW_{Se} \tag{2.5}$$

where ρ_f is the film density (g cm^{-3}) and MW_{Se} is molecular weight of selenium. The mass balance equations for the chemical equations in table 2.2 are given in table 2.3.

The temperature dependence of a specific reaction rate constant k_i is represented by the Arrhenius equation

$$k_i = k_{i0} \exp(-E_{ai}/RT) \tag{2.6}$$

where k_{i0} is the frequency factor, E_{ai} is the activation energy, R is the gas constant and T, is the absolute temperature. Using experimentally determined values for k_{i0} and E_{ai} (table 2.4) and the Arrhenius equation, prediction of moles of pertinent species with reaction period can be predicted at any desired reaction temperature.

2.4 Phase Concentration using X - Ray Diffraction Data

The number of moles for a phase can be calculated using XRD intensity. The analysis is based on the principle that the diffraction pattern of a particular phase in a mixture depends on the concentration of that phase in the mixture. In a diffractometer, the relationship between the intensity of a particular phase and its concentration is [Cullity, 1978]:

$$I_{dl} = \left[\frac{I_{0b} A \lambda^3}{32\pi r}\right]\left[\left(\frac{\mu_0}{4\pi}\right)^2 \frac{q^4}{me^2}\right]\left[\frac{1}{v^2}\right]|F_{sf}|^2 P_{mf}\left(\frac{1+\cos^2 2\theta}{\sin^2 \theta \cos \theta}\right)\left[\frac{T_{tf}}{2\mu_l}\right] \tag{2.7}$$

where I_{dl}: integrated intensity per unit length of diffraction line (joules $\text{sec}^{-1}\text{m}^{-1}$)

I_{0b}: intensity of incident beam (joules $\text{sec}^{-1}\text{ m}^{-2}$)

A: cross-sectional area of incident beam (m^2)

λ: wavelength of incident beam (m)

r: radius of diffractometer circle (m)

μ_0: $4\pi \times 10^{-7}$ m kg C^{-2}

q: charge on electron (C)

m_e: mass of electron (kg)

v: volume of unit cell (m³)

F_{sf}: structure factor

p_{mf}: multiplicity factor

θ: Bragg angle

T_{tf}: temperature factor

μ_l: linear absorption coefficient (m⁻¹)

For a multi-phase mixture, the above equation simplifies to

$$I_i = \frac{K_i \phi_i}{\mu_m}$$ (2.8)

where I_i is the intensity of the selected angle of the ith phase, K_i is the XRD intensity per mole for species i, ϕ_i is the volume fraction of the ith phase and μ_m is the linear mass absorption coefficient of the mixture. K_i can be determined using an independent method (see appendix A).

The relative amount of any phase for selenized CuIn bilayer can be estimated from XRD pattern using the following relation [Verma, 1993]:

$$\phi_i = \frac{\frac{I_i}{K_i}}{\sum_i \frac{I_i}{K_i}}$$ (2.9)

where $I_i = Cu_{11}In_9$, In_2Se, $InSe$ and $CuInSe_2$ and ϕ_i represents the volume fraction of any one of these four phases.

The mass fraction of various species, w_i, is

$$w_i = \frac{\dfrac{I_i\rho_i}{K_i}}{\sum_i \dfrac{I_i\rho_i}{K_i}}$$

(2.10)

where ρ_i represents the density of the ith phase.

If M_i is the molecular weight of the ith phase, the mole fractions of different phases in the film is

$$x_i = \frac{\dfrac{I_i\rho_i}{K_iM_i}}{\sum_i \dfrac{I_i\rho_i}{K_iM_i}}$$

(2.11)

The concentration of species, c_i is given by

$$c_i = \frac{w_i}{M_i}\rho_f$$

(2.12)

where the film density ρ_f is averaged over the various species.

Finally, the number of moles for any species can be calculated by multiplying the concentration by the volume of the film.

2.5 Operation and Characteristics of Solar Cell

Solar cells are semiconductor devices that convert sunlight directly to electrical energy by using the photovoltaic process. Light absorbed by a semiconductor generate electron-hole pairs. These pairs are separated by an internal electric field across the solar cell junction which produces an electric current in the external circuit.

The efficiency of the operating solar cell depends on the balance between generation, recombination and carrier transport to the built-in field region, as well as its ability to separate both types of carriers effectively. Solar cells have finite series resistance, R_s, due to the bulk resistance of the semiconductor material, the contact resistance between the metallic contacts and the semiconductor and of the resistance of the metallic contacts itself. The leakage current across the p-n junction around the edge of the cell occurs due to the presence of defects and is described in terms of a shunt resistance, R_{sht}.

The solar cell output can conveniently be examined through three main parameters(figure 2.4.)

- Short circuit current density, J_{sc};

- Open circuit voltage, V_{oc}; and

- Fill Factor, FF.

These parameters determine the efficiency and the circuit conditions to be used with the cells or an array of such cells.

As shown in figure 2.5, a solar cell can be modeled as an ideal diode in parallel with a light induced current generator, I_L, whose magnitude is a function of the generation of electron-hole pairs by the absorption of incoming light and the collection efficiency for these charge carriers. The current and voltage characteristics are given by

$$I = I_0 \left\{ \exp\left|\frac{q(V-IR_s)}{A_{Dqf}}\right| - 1 \right\} + \frac{(V-IR_s)}{R_{sh}} - I_L \qquad (2.13)$$

where I_o = dark current; $q = 1.6 \times 10^{-19} C$ (charge of an electron); V = Voltage; A_{Dqf} = diode quality factor; $k = 8.65 \times 10^{-5}$ eV/K (Boltzmann constant); T = Absolute temperature in Kelvin; I_L = light-generated current.

Assuming R_s is small and R_{sh} is large, equation 2.13 reduces to the standard diode equation representing the J - V characteristic as follows:

$$J = J_o \left[\exp(\frac{qV}{A_{Dqf}kT}) - 1 \right] - J_L \qquad (2.14)$$

J, J_0 and J_L in equation 2.14 are simply I, I_0, and I_L, respectively divided by the total area of the junction.

The short circuit current density, J_{sc}, is ideally the light-generated current measured at $V = 0$. The open circuit voltage V_{oc} is obtained by setting $J = 0$:

$$V_{oc} = \frac{kT}{q} \ln(\frac{J_{sc}}{J_o} + 1) \qquad (2.15)$$

The fill factor is a measure of the squareness of the J - V curve and the quality of the solar cell. It is given by:

$$FF = \frac{P_{mp}}{V_{oc}J_{sc}} = \frac{V_{mp}J_{mp}}{V_{oc}J_{sc}}$$
(2.16)

The conversion efficiency, η, is the ratio of the maximum electrical power, P_{mp}, to the total power of the incident light source, P_{in} :

$$\eta = \frac{P_{mp}}{P_{in}} = \frac{V_{oc}J_{sc}}{P_{in}} FF$$
(2.17)

2.6 Transport Mechanism in the Heterojunction

The optical and electronic properties of semiconductor junctions are controlled by various processes of generation and recombination of carriers, diffusion and drift. Transport of carriers across the heterojunction can be described in terms of the following mechanism (figure 2.6):

- Injection and diffusion in the quasi neutral zone;

- Transport via interface states (interface recombination);

- Transport via gap states in the space charge region (space charge recombination); and

• Tunneling.

The basic recombination process are mainly described as band-band recombination and recombination through intermediate centers. Band-band recombination mechanism is where an electron-hole pair recombine. An electron occupying a higher energy state undergoes transition from the conduction band to the valence band by emission of a photon or by transferring the energy to another free electron or hole in the Auger process.

Imperfections and impurities in the semiconductors can introduce energy levels in the forbidden gap. These intermediate levels allow two-step recombination processes such that electrons relax from conduction band energies to the defect level and then proceed on to the valence band annihilating a hole. Probability of transition depends on the position of the energy level in the gap and the defect density. Recently, recombination in the space charge region via states in band tails was identified as the dominant bucking current mechanism [Klenk and Schock, 1994].

J - V curves can be approximated by analytical numerical calculations [Klenk, 1993]. Current transport in a semiconductor can be described by few coupled differential equations. The transport of electrons and holes is given by the sum of the drift and diffusion process (one dimensional, stationary case):

$$g_n = qn\mu_n E + qD_n \frac{dn}{dx} \qquad (2.18)$$

$$g_p = qp\mu_p E + qD_p \frac{dp}{dx} \qquad (2.19)$$

Applying the equations of continuity

$$\frac{1}{q}\frac{dg_n}{dx} = -G_n + R_n$$
(2.20)

$$\frac{1}{q}\frac{dg_p}{dx} = G_p - R_p$$
(2.21)

and the Poisson's equation (assuming shallow doping levels)

$$J = J_o[\exp(\frac{qV}{A_{Dqf}kT})-1]-J_L$$
(2.22)

where J_o and A_{Dqf} depend on the dominate recombination mechanism.

The number of electron-hole pairs collected at each wavelength relative to the number of photons incident on the surface at that wavelength determines the spectral response of the device, also known as the quantum efficiency, Q:

$$Q = \frac{J_L(\lambda)}{q\Gamma(\lambda)}$$
(2.23)

The "internal" spectral response is defined as the number of electrons-hole pairs collected at zero applied voltage relative to the number of photons entering the material while the "external" response is just the internal one modified by reflection of light from the surface of the device. To obtain an analytical approximation of the spectral response the following assumptions are made in addition to the equations given above.

- 1) Each absorbed photon generates one electron-hole pair;

- 2) Neglecting the influence of minority carriers;

- 3) Complete collection in the space charge layer;

- 4) The Mo contact is acting as a high recombination surface (surface recombination velocity for electrons at back contact approach infinity).

The absorber is divided into the space charge region $\{0,w\}$ and field free zone $\{w,t_{CIGS}\}$, as shown in figure 2.7. With the assumptions made above, one gets ($w < x < t_{CIGS}$):

$$g_n = qD_n \frac{dn}{dx} \tag{2.24}$$

$$\frac{1}{q}\frac{dg_n}{dx} = G_n + R_n \ ; \ R_n = \frac{n}{\tau_n} \tag{2.25}$$

leading to the differential equation [Klenk, 1993]

$$\frac{d^2n}{dx^2} - \frac{n}{L^2} + G = 0 \ ; \ L = \sqrt{D_n\tau_n} \tag{2.26}$$

with the following boundary conditions according to 3) and 4) above:

$$n(w) = n(t) = 0 \tag{2.27}$$

and according to 1).:

$$G = \alpha_p \varphi_o \exp(-\alpha_p x) \quad \text{for illumination through the window (frontwall)} \tag{2.28}$$

$$G = \alpha_p \varphi_o \exp(-\alpha_p(t_{CIGS} - x)) \quad \text{for illumination through the back contact (backwall)} \tag{2.29}$$

Finally, the solution for the two cases is [Hovel, 1975]:

$$Q_F = 1 - \exp(-\alpha w) \left| \frac{1}{1+\alpha L} - \frac{\alpha L}{\alpha^2 L^2 - 1} \frac{\exp(-\alpha d_{cr}) - \exp(-d_{cr}/L)}{\sinh(d_{cr}/L)} \right| \tag{2.30}$$

$$Q_b = \frac{\alpha L}{\alpha^2 L^2 - 1} x \left| \frac{1 - \exp(-\alpha d_{cr})\cosh(d_{cr}/L)}{\sinh(d/L)} - \alpha L \exp(-\alpha d_{cr}) \right| \\ + \exp(-\alpha d_{cr})(1 - \exp(-\alpha w)) \tag{2.31}$$

If recombination at the back contact can be neglected (d_{cr} approaches infinity), Q_F reduces to the well known expression [Liu and Sites, 1994]

$$Q_f = 1 - \frac{\exp(-\alpha w)}{\alpha L + 1} \tag{2.32}$$

with

w = depletion width

α = absorption coefficient for wavelength λ

d_{cr} = thickness of field free collection region

L = diffusion length

t_{CIGS} = thickness of CIGS: $t_{CIGS} = d_{cr} + w$

Q_F = Frontwall Quantum Efficiency

Q_b = Backwall Quantum Efficiency

Q_f = Frontwall Quantum Efficiency with d approaching infinity

G = Generation rate

Table 2.1. Properties of CuInSe$_2$ [Rocket and Birkmire, 1991]

Property	Value	Unit
Formula	CuInSe$_2$	
Molecular weight	336.28	
Density	5.77	g cm^{-3}
Color	gray	
Transition to sphalerite structure	810	°C
Melting temperature	986	°C
Symmetry	Chalcopyrite	
Space group	$I42d - D_{2d}^{12}$	
Lattice parameters		
a_0	0.5789	nm
c_0	1.162	nm
Thermal expansion coefficient (at 273 K)		
(a axis)	8.32×10^{-6}	K^{-1}
(c axis)	7.89×10^{-6}	K^{-1}
Thermal conductivity	0.086	W cm^{-1} K^{-1}
Specific heat[a]		
c_1	-7.67×10^{-4}	K^{-1}
c_2	4.06×10^{-6}	K^{-2}
c_3	4.3×10^{-6}	K^{-3}
Debye temperature	221.9	K
Microhardness (112 face)	3.2×10^{9}	N m^{-2}
Compressibility	1.4×10^{-11}	m^2 N^{-1}
Dielectric constant		
Low frequency	13.6 ± 2.4	
High frequency	8.1 ± 1.4	
Sound velocity (longitudinal)	2.2×10^{5}	cm s^{-1}
Electrical resistivity (polycrystalline thin films)		
Cu-rich	0.001	Ω cm
In-rich	>100	Ω cm
Mobility		
electrons (n=10^{14}-10^{17} cm^{-3})	100 - 1000 (at 300K)	cm^2 V^{-1} s^{-1}
holes (p=8×10^{15} - 6×10^{16} cm^{-3})	50 - 80 (at 300K)	cm^2 V^{-1} s^{-1}
Effective mass		
Electrons	0.09	m$_e$
Holes (heavy)	0.71	m$_e$
(light)	0.092	m$_e$
Energy gap (In-rich polycrystalline films)	1.02	eV
Temperature dependence of gap		
$dE_g/dT \, (77 - 300K)$	$-2 \pm 1 \times 10^{-4}$	eV K^{-1}
Pressure dependence of gap		
dE_g/dP	2.8×10^{-11}	eV Pa^{-1}

[a]Specific heat: $C_p(T) = 12R[F(\Theta_D/T) + c_1 T + c_2 T^2 + c_3 T^3]$, where R is the molar gas

constant and F is the Debye function.

Table 2.2. Reaction pathways for $CuInSe_2$ formation [Orbey et. al., 1997]

Reaction set with CuIn

$2\,In + Se \rightarrow In_2Se$	k_2
$In_2Se + Se \rightarrow 2\,InSe$	k_3
$2\,CuIn + 2\,Se \rightarrow Cu_2Se + In_2Se$	k_5
$2\,InSe + Cu_2Se + Se \rightarrow CuInSe_2$	k_7

Reaction set with $Cu_{11}In_9$

$2\,In + Se \rightarrow In_2Se$	k_2
$In_2Se + Se \rightarrow 2\,InSe$	k_3
$2\,Cu_{11}In_9 + 20\,Se \rightarrow 11\,Cu_2Se + 9\,In_2Se$	k_5
$2\,InSe + Cu_2Se + Se \rightarrow 2\,CuInSe_2$	k_7
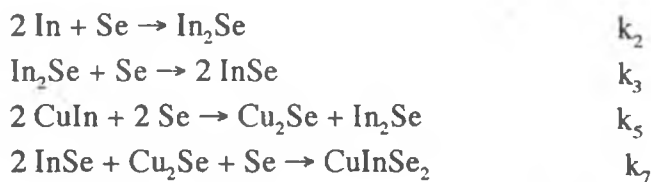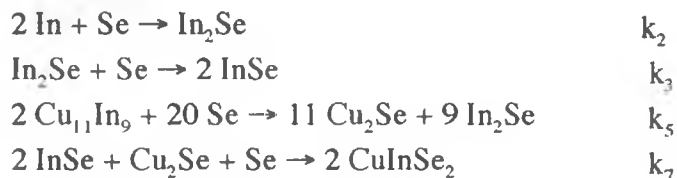
Table 2.3. Reaction analysis model equations [Verma et. al., 1996, Orbey et. al, 1997]

With $Cu_{11}In_9$ as the CuIn alloy

$$\frac{d([In]V_f)}{dt} = -2k_2[Se][In]V_f = -2k_2'[In]V_f$$

$$\frac{d([In_2Se]V_f)}{dt} = (k_2[Se][In] - k_3[Se][In_2Se] + 9k_5[Se][Cu_{11}In_9]))V_f = (k_2'[In] - k_3'[In_2Se] + 9k_5'[Cu_{11}In_9])V_f$$

$$\frac{d([InSe]V_f)}{dt} = (2k_3[Se][In_2Se] - 2k_7[Se][InSe][Cu_2Se])V_f = (2k_3'[In_2Se] - 2k_7'[InSe][Cu_2Se])V_f$$

$$\frac{d([Cu_{11}In_9]V_f)}{dt} = -2k_5[Se][Cu_{11}In_9]V_f = -2k_5'[Cu_{11}In_9]V_f$$

$$\frac{d([CuInSe_2]V_f)}{dt} = (2k_7[Se][InSe][Cu_2Se])V_f = (2k_7'[InSe][Cu_2Se])V_f$$

$$\frac{d([Cu_2Se]V_f)}{dt} = (11k_5[Se][Cu_{11}In_9] - k_7[Se][InSe][Cu_2Se])V_f = (11k_5'[Cu_{11}In_9] - k_7'[InSe][Cu_2Se])V_f$$

Table 2.4. Experimental values for frequency factor and activation energy [Orbey et. al., 1997; Verma et. al., 1996]

Reaction Rate constant	Frequency factor	Activation Energy (kJ/mol)
k'_3 (min^{-1})	4.9×10^4	66
k'_5 (min^{-1})	1.1×10^7	100
k'_7 (cm^3 mol^{-1} min^{-1})	2.0×10^3	25
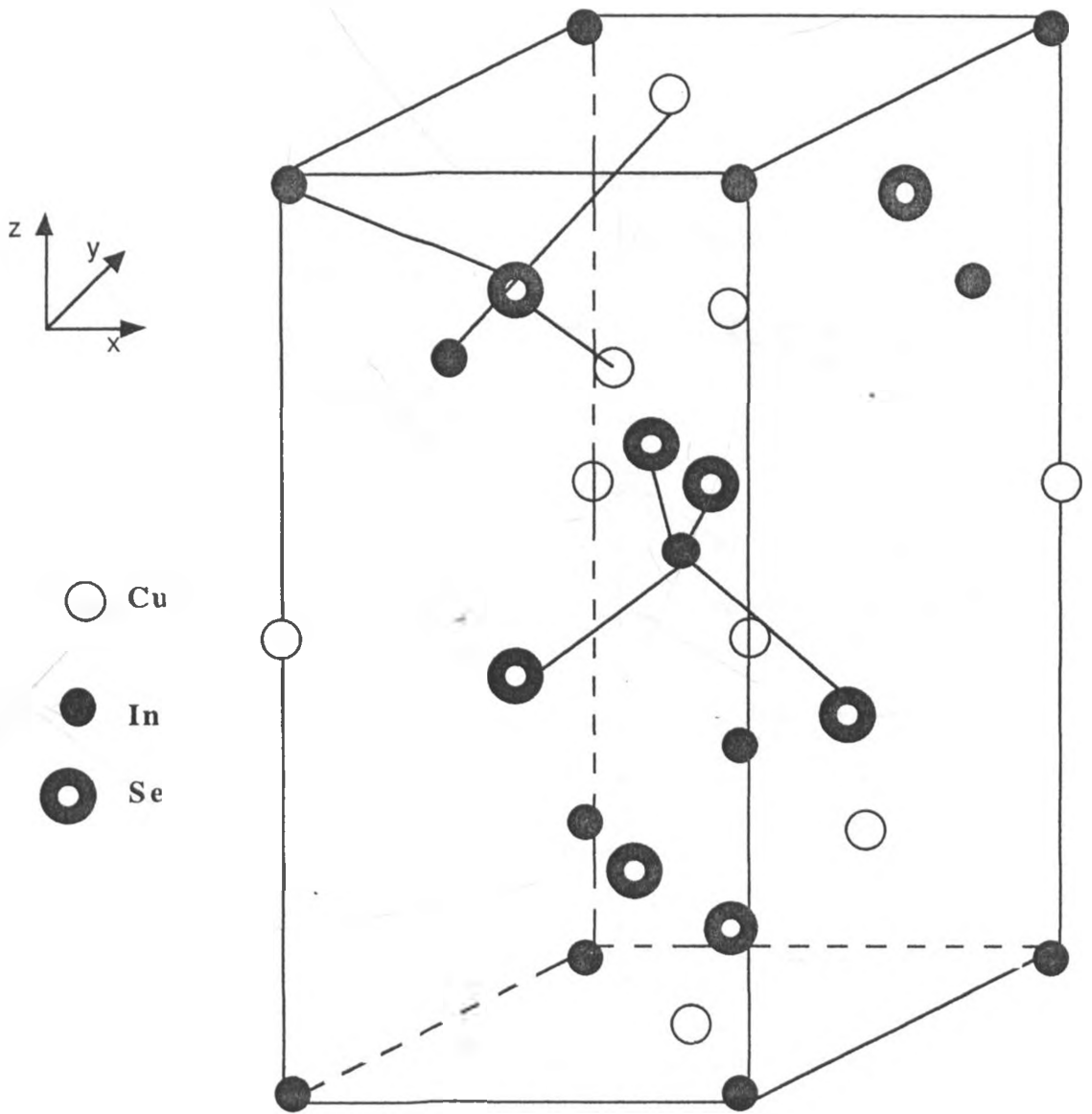
Figure 2.1. Crystal structure for CuInSe$_2$.
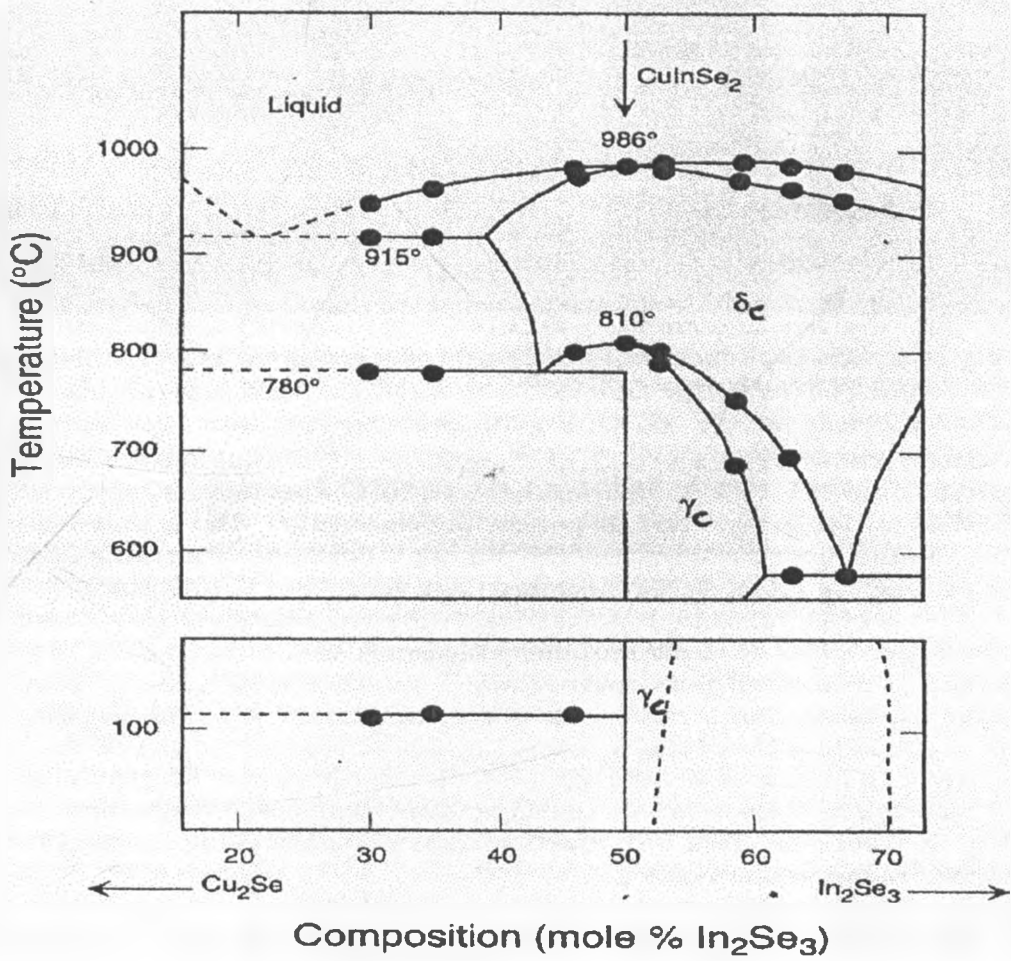
Figure 2.2. Pseudo-binary Cu_2Se/In_2Se_3 phase diagram [Fearheiley, 1986].

rate of delivery

$r_d(i)$

rate of removal

$r_r(i)$

rate of reaction

$r_{rxn}(i)$

SUBSTRATE

sodalime glass with 1μm Mo
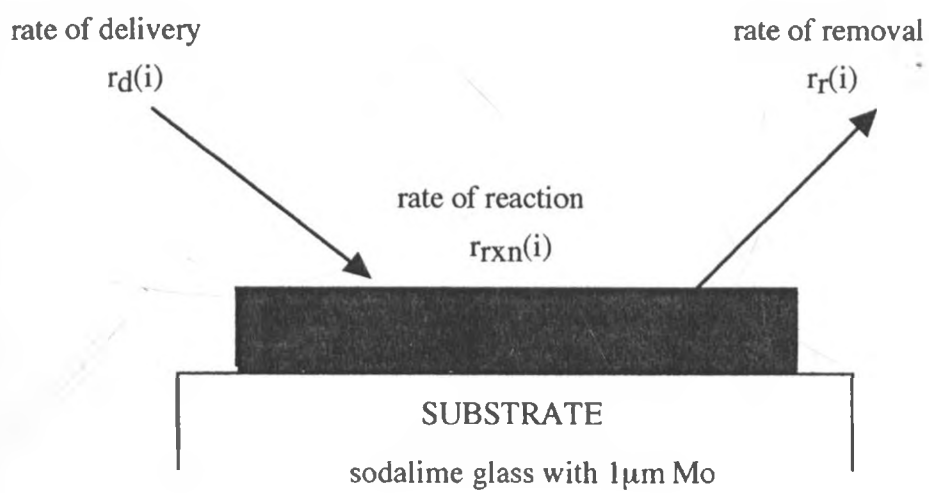
Figure 2.3. Control volume definition in film growth.
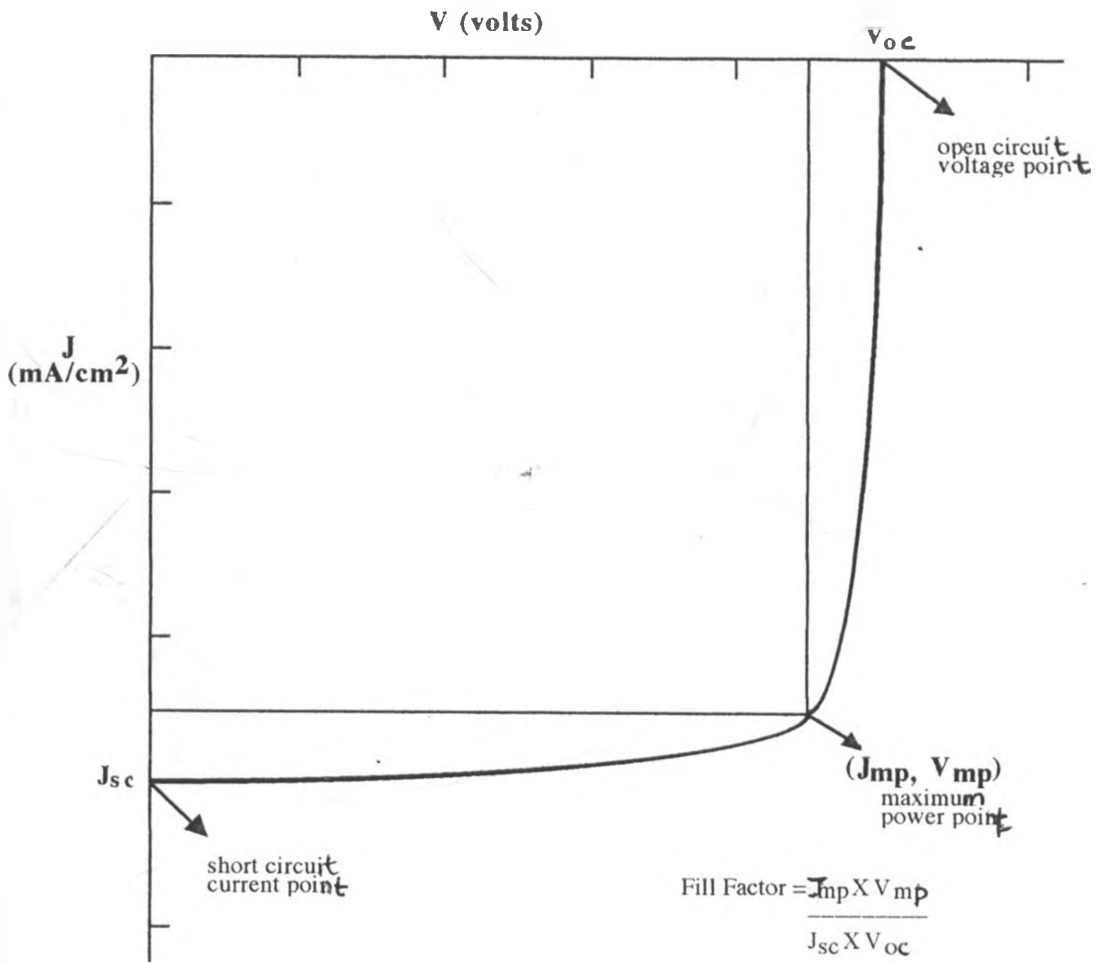
Figure 2.4. Solar cell parameters.
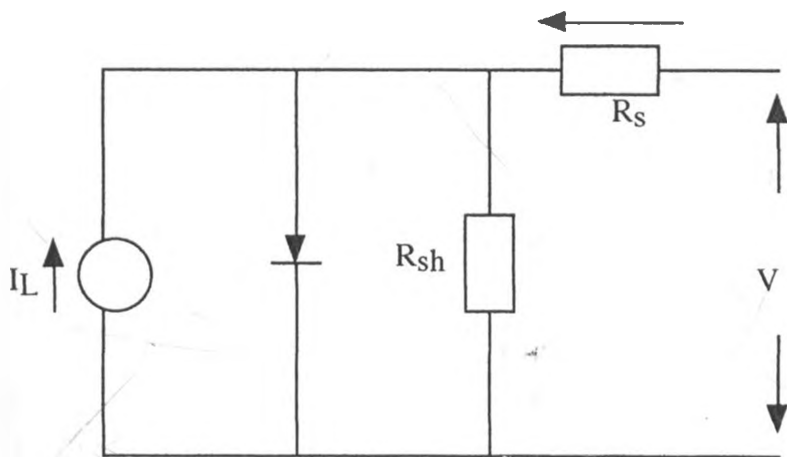
Figure 2.5. A model for a solar cell.
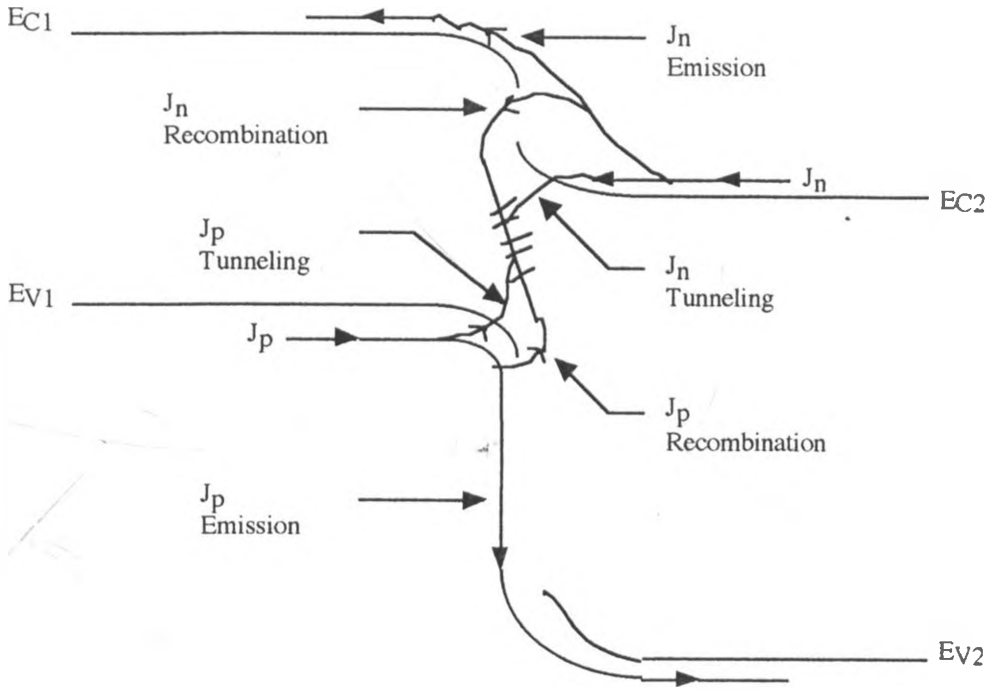
Figure 2.6. Possible current transport mechanisms in a p-n heterojunction.
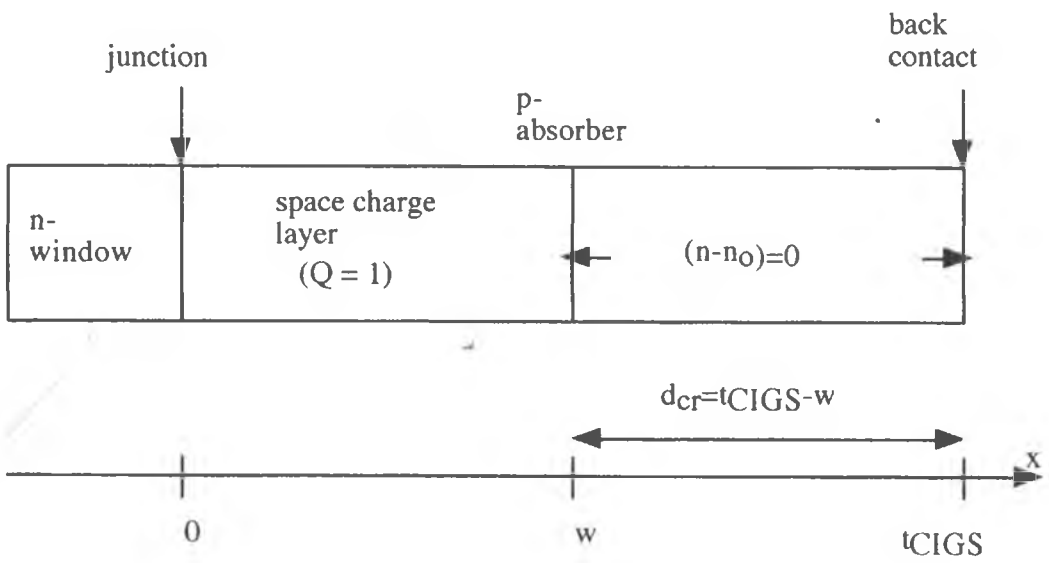
Figure 2.7. Geometry for analytical approximations of photo-current collection.

CHAPTER THREE

EXPERIMENTAL TECHNIQUES

3.1 Substrate Preparation

Substrate preparation involves cutting glass substrates to required size as well as cleaning them.

In this work, two cleaning procedures were used depending on which laboratory the work was carried out. At the Solar Energy Laboratory, University of Dar es Salaam, soda-lime glass measuring, $76 \times 26 \times 1$ mm^3 used as substrates were cleaned in detergent, rinsed with deionised water, cleaned in ultrasonic cleaner for 20 minutes, rinsed with alcohol and finally dried in ethanol vapor. At IEC, University of Delaware, the soda-lime glass measuring $25.4 \times 25.4 \times 1.5$ mm^3, were cleaned in warm ultrasonically stirred soap solution for 3 minutes, rinsed in cold deionized tap water for few minutes, cleaned in an ultrasonically stirred deionized hot water bath, and finally dried in a dry-nitrogen and in an oven maintained at about 82 °C.

3.2 Metallic Mo, Cu, In and CuIn Bilayer

All the Mo, Cu and In layers deposition were carried out using DC magnetron sputtering. All the targets were water cooled and Ar was used as the sputtering gas. Prior to each deposition, presputtering was done for about 5 to 30 minutes; during which the substrate was shielded by a shutter. Presputtering was necessary in order to remove surface contaminants from the target. Since three different sputtering

systems were used in this work, only a general schematic diagram of a sputtering unit is shown in figure 3.1.

3.2.1 Mo Deposition.

A CVC AST 601 system was used for Mo deposition on $25.4 \times 25.4 \times 1.5$ mm^3 soda-lime glass using a Mo target (99.99 % purity, 203.2 mm diameter, 6.4 mm thick). A 1 μm Mo film thick was deposited in two-layer process because of adherence and conductivity considerations. The first layer (0.1 μm) was deposited under conditions of low power, producing a film that adheres well to the soda-lime substrate. This layer has a high sheet resistance. The second layer (0.9 μm) adheres well to the first layer and has a low sheet resistance. This second layer could not be distinguished from the first layer and it grew quasiepitaxially on the first layer. Typical sheet resistance for the total Mo layer is in the range 0.22 to 0.27 Ω/sq.

The CVC AST 601 system consists of a deposition chamber which accommodates six 203.2 mm diameter circular targets at the bottom. The targets are isolated from each other by built-in metal shields around each target. The substrate holders are circular-shaped and capable of holding ten $25.4 \times 25.4 \times 1.5$ mm^3 substrates placed in each of the six slots in a carousel that rotates above the targets. Shutters are used to start and stop the deposition of material onto the substrates. The target to substrate distance was maintained at 50.8 mm. The deposition chamber was evacuated using a roughing pump and a cryogenic pump. The base pressure in the chamber can be as low as 1.0 ×

10^{-7} mbar for overnight pumping. Typical run conditions for the Mo deposition are shown in table. 3.1.

3.2.2 Metallic Cu and In Layers

A Balzers 250 BAE sputtering system was used for metallic Cu and In films deposition on 76 x 26 x 1 mm^3 soda lime glass. Cu and In targets used were 99.99 % pure, 50 mm diameter and 6.4 mm thick.

The Balzers system can accommodate two 50 mm diameter planar magnetrons. The system has a radiant heater for substrate heating, two automatic gas regulators for measuring argon and a reactive gas (e.g. O_2 or H_2) flow rates. It is also equipped with 1 kW DC / 0.5 kW RF power sources and a quartz crystal for thickness monitoring. In this research, the sputtering pressure was varied by controlling the Ar flow rate (see appendix B for relationship between Ar flow rate and sputtering pressure for our equipment). A manually operated shutter was used to start and stop the deposition of material on a substrate. Substrate to target distance is 150 mm. The evacuation of the sputtering chamber was done by using a roughing and turbomolecular pump. Typical run conditions for Cu and In are shown in tables 3.2 and 3.3, respectively.

3.2.3 CuIn Bilayer: Deposition and Elemental Thickness.

CuIn bilayers were deposited sequentially without breaking vacuum by a Lesker super III DC magnetron sputtering system on 25.4 × 25.4 × 1.5 mm^3 molybdenum-coated soda-lime glass. The Cu target was 99.99 % pure, 152.4 mm diameter and 6.4 mm thick. A copper cup filled with In served as an Indium target. The thicknesses of Cu and In depended on the desired $CuInSe_2$ thickness and Cu/In ratio of the $CuInSe_2$

absorber film. In this work, the Cu/In ratio was kept constant at 0.8. The elemental layer thicknesses used are shown in table 3.4. For details on elemental thickness calculations for a fixed Cu/In ratio, see appendix, C.

The Lesker super III system consists of a deposition chamber which accommodates four 152.4 mm diameter circular targets at the bottom. Cylindrical shields are used to isolate the targets. The substrate holders (trays) are square-shaped and capable of holding nine $25.4 \times 25.4 \times 1.5$ mm^3 substrates placed in each of the four slots in a carousel. The tray positions can be switched by a semi - automatic step motor which can rotate the carousel a quarter turn. It is also possible to deposit while the carousel is rotating above the targets. Shutters, one on each target, are used to start and stop the deposition of material onto the substrates by use of pneumatic switches. The target to substrate distance was maintained at about 15 cm. The deposition chamber is evacuated using a roughing pump and a cryogenic pump. These pumps are automatically switched by a valve sequencer which reacts to pressure readings of the ionization gauge. The base pressure in the chamber can be as low as 1.0×10^{-7} mbar. Typical run conditions for the Cu and In deposition are shown in tables 3.5 and 3.6 respectively.

3.3 Selenization

IEC CVD reactor was used for selenization of all the samples. Figure 3.2 shows the entire selenization system. Details of the reactor design and procedure is given by Verma (1993).

The CuIn layers, placed on a substrate holder in a tubular quartz with a heating jacket, were reacted in a 0.35 % H$_2$Se in an Ar/O$_2$ atmosphere (O$_2$/H$_2$Se = 0.01) for 15 - 90

minutes at reaction temperatures of 350 -500 °C. Two samples were made for each reaction period and temperature; one was for film characterization and the other one for solar cell fabrication.

After loading the samples, the reactor was evacuated to pressures of $< 2.6 \times 10^{-3}$ mbar to remove excess moisture and oxygen. A residual gas analyzer (RGA) was used to check the desired vacuum level. The reactor was then filled with Ar/O_2 to atmospheric pressure. After establishing the proper gas flow rates, the temperature of the reactor was ramped for 10 minutes to desired reaction temperature and then allowed to react for the desired reaction time. At the end of the experimental run, the samples were allowed to cool slowly in Ar atmosphere for about one hour before been unloaded. The procedure was repeated for all other reaction temperatures and periods.

3.4 Film Characterization

3.4.1 Structural Characterization

3.4.1.1 Thickness

Numerous methods are available for thin film thickness determination. However, some methods are not useful for some materials since they are destructive. In this work, three methods were employed for thin film thickness measurement. Quartz crystal was used to monitor the thickness of the films. For films where accuracy was not of concern, thickness monitored using the quartz crystal was enough but for those where accurate thickness was needed, thickness calibration to get exact physical thickness using the dektak and weighing method was done. Mo, Cu and ZnO films are smooth and hard and therefore a dektak was good enough for thickness

measurement. Indium layer is very soft and has large-sized morphology and therefore weighing method was used for thickness estimation. Weighing method was also found to be most suitable for estimating $CuInSe_2$ thin films thickness as the film were not smooth and they were grown on Mo coated glass substrates. In both cases of thickness estimation by weighing method, bulk densities of In and $CuInSe_2$ were assumed to be the same as for films. CdS thickness was estimated from the fall off of the quantum efficiency of $CuInSe_2$/CdS device at 400 nm which is attributed to absorption in the CdS [Sharfaman, 1998].

3.4.1.1.1 Quartz Crystal Monitor

The quartz crystal monitor employs the theories by Mason (1956), and Warner and Stockbridg (1963) who showed that a change in frequency, Δf_q, due to a deposit of mass, m_f, added to the area, A_q, of the antinodal surface of a mechanical resonator is given by

$$\Delta f_q = -f_q \frac{K_q m_f}{\rho_q A_q d_q} \qquad (3.1)$$

where K_q is a constant (≈ 1) for a quartz crystal, m_f is the mass of the film, d_q is the quartz crystal thickness, f_q is the frequency of the fundamental resonance of a thickness mode for an AT cut crystal, and ρ_q is the density of quartz.

Analysis of the loaded crystal as one dimensional composite resonator of quartz and deposited film led to the equation [P/N 102800]:

$$t_f = \frac{\rho_q}{\rho_f} N q \frac{T_l}{\pi R_z} \arctan\left[R_z \tan \pi \left(\frac{T_l - T_q}{T_l} \right) \right] \qquad (3.2)$$

where ρ_q is the density of quartz in g cm^{-3}, ρ_f is the density of the film in g cm^{-3}, $Nq =$ 1.668 × 10^5 msec^{-1}, T_l is the period of the loaded crystal, T_q is the period of the uncoated crystal and R_z is the acoustic impedance ratio which is obtained by dividing the acoustic impedance of quartz by the acoustic impedance of the deposited film.

The use of microprocessors allows equation 3.2 to be solved economically and implemented in the monitor.

3.4.1.1.2 Dektak

The Sloan Dektak apparatus scans the surface of a sample and measures thickness by profilometry. Here, a very thin diamond needle travels along the surface. The roughness and steps of the film is proportional to their depth. Figure 3.3 shows a typical trace for the Dektak. The expected accuracy of this technique is ± 10 %. Leveling of the sample holder is a must for accurate results.

3.4.1.1.3 Weighing Method

In weighing method, the actual film thickness is calculated by measuring the mass of the substrate before and after deposition and using the equations

$$\rho_f = \frac{m_f}{V_f} \qquad (3.3)$$

and

$$V_f = l_f b_f t_f, \tag{3.4}$$

where ρ_f, m_f, V_f, l_f, b_f and t_f are density, mass, volume, length, breadth and thickness of film, respectively. The film thickness, t_f, will be given by:

$$t_f = m_f / (l_f b_f \rho_f) \tag{3.5}$$

where $l_f b_f$ is the area of the film.

Density of bulk material was assumed in the calculations using equation 3.5 above. Errors in film thickness estimation can occur due to non uniformity of the films. These were minimized by considering four samples and taking an average.

3.4.1.2 Scanning Electron Microscopy (SEM)

Amray model 1810 Scanning Electron Microscope was used for morphological analysis of the films. Photomicrographs were taken using Polaroid Type 52 film and a Sony Video Graphic Monitor (Model UP 870 MD).

3.4.1.3 Energy Dispersive Spectroscopy (EDS)

Energy dispersive spectroscopy was used to measure the average atomic composition of each film. The instrument was primarily used to determine the Cu/In ratio in the $CuInSe_2$ films. The EDAX model 9800 system was attached to the AMRAY 1810 SEM. Under standard conditions of detection, the accelerating voltage was set at 20

kV, the sample was mounted at 20 ° tilt angle, the magnification was set at 1000× and the counts were integrated over 200 live seconds in the slow scan mode. The accompanying software calculates the integrated counts for the different elements by curve fitting, and has the ability to calculate the compositions based on standards (in the QUAN mode) or by using the available pure intensity factors for elements (in the SUPERQUAN mode). All reported composition values for $CuInSe_2$ in this research was in SUPERQUAN mode. The pure intensity factors in the SUPERQUAN mode were tuned to reflect the elemental compositions of the $CuInSe_2$ thin films in the range of compositions 25 % at. Cu, 25 % at. In, and 50 % at. Se. The expected accuracy of this technique in determining the film composition close to the calibration standards of the stoichiometric $CuInSe_2$ is ± 1 %.

3.4.1.4 Transmission Electron Microscopy (TEM)

A Joel 1010 microscope was used to perform transmission electron microscopy. The acceleration voltage and magnification were set at 100 kV and 50000x, respectively. Samples for this investigation were 34 nm thick metallic Cu films deposited on 3 mm diameter copper grids pre-coated with amorphous carbon film. The shapes and sizes of the grains were studied by direct measurements on the dark field micrographs. The dark field imaging uses diffusely scattered electrons and is advantageous in the sense that the image is quite insensitive to sample (i.e. film) tilt and microscope deforms. Bright field micrographs were also important for comparison purposes.

3.4.1.5 X Ray Diffraction (XRD)

A philips/Nareko scanning 2θ diffractometer was used to analyze selenized samples to

identify the phases in the films. X-rays scans were performed for $2\theta = 20$ to $80°$ for a

step size of $0.05°$ and integrated for 4 s. per step using Cu Kα radiation. To resolve

closely spaced peaks, high resolution scans were carried out at a step size of $0.02°$

integrated for 10 s per step. The current and voltage settings were 20 mA and 35 kV

respectively. IGOR software was used to plot 2θ versus intensity and to calculate d

spacing of maximum of each peak according to

$$d = \frac{\lambda_{\alpha 1}}{2 \sin \theta} \tag{3.6}$$

where $\lambda_{\alpha 1} = 1.540562\text{Å}$ is the wavelength of the Cu Kα radiation. The relationship to

predict the diffraction angle of any set of planes is described in appendix D.

Phases were identified by matching the XRD peaks with those tabulated in the Joint

Council for Powder Diffraction Studies (JCPDS) cardfile.

3.4.1.5.1 Estimation of Mole Intensities using XRD Data

XRD results were used to estimate approximate number of moles fractions of the

product species formed on the Mo coated soda lime substrate. In this research, we are

dealing with film layers (SL/Mo/CuInSe$_2$), for which it is not always possible to

prepare calibrated samples, and orientation effects may not be negligible. However,

approximate methods can be developed. Method used by Verma (1993) with some modification was used in this work. The details are given in section 2.4 and appendix A.

Unnormalized[*] peak intensities were used to estimate the mole intensities as this was found to be more accurate by earlier workers at IEC [Birkmire, 1998]. Only CuInSe$_2$ and InSe species moles were estimated as these were the only species in the CuInSe$_2$ film growth model observed in our samples. Although multiple peaks for both CuInSe$_2$ and InSe were observed in the XRD traces, only strong peaks are sufficient for mole estimation. The CuInSe$_2$ peak at $2\theta = 26.60$ ° (d-spacing = 3.35Å, hkl = 112) and InSe peak at $2\theta = 21.31$ ° (d-spacing = 4.17Å, hkl = 004) were the ones considered in the species moles estimation.

3.4.2 Electrical and Optical Characterization

3.4.2.1 Sheet Resistance and Resistivity

Four point probe method was used for sheet resistance measurements. The four point probe system consists of four equally spaced pins which can be pressed on the film surface for measurement of voltage across and current through the film. From the equation

$$R_{sq} = \frac{\pi V}{I \ln 2} \qquad (3.7)$$

---

[*] The peak intensities were not normalized (i.e. peak intensities were not divided with the intensity of Mo peak).

where R_{sq} is the sheet resistance, V is the voltage between the inner pins and I is the current through the film. It follows that for $I \ln 2 = \pi$, R_{sq} will be equal to the measured voltage. Resistivity was calculated by multiplying the sheet resistance by the film thickness [Mwamburi, 1994].

3.4.2.2 Spectrophometry

The optical transmission and reflection of the films were measured using a Perkin Lambda 9 spectrophotometer equipped with an integrating sphere and a specular reflectance/transmittance accessory. Specular transmittance and reflectance were measured for metallic films. For background correction, air and freshly evaporated aluminium films were used as reference for transmittance and reflectance measurements, respectively. The angle of incidence for reflectance measurements was 15 °C. For $CuInSe_2$ films, an integrating sphere accessory was used for total transmittance and reflectance measurements with $BaSO_4$ used as a reference. Spectral ranges of 300 to 2500 nm and 700 to 1500 nm were used for metallic films and $CuInSe_2$ films respectively.

3.5 Device Fabrication

Solar cells were fabricated by sequential deposition of CdS, bilayer ZnO, and Ni/Al grids on the soda lime glass/Mo/$CuInSe_2$. A schematic diagram for the complete cell structure is shown in figure 3.4

3.5.1 CdS Layer

A 40 nm thick CdS layer was deposited by chemical bath deposition. The bath, prepared using nanopure de-ionized water, contained Cadmium sulfate ($CdSO_4$), Thiourea (($NH_2)_2CS$) and Ammonium hydroxide($NH_4)OH$) as reactants and their concentrations were as follows:

$[CdSO_4] = 0.015$ M

$[(NH_2)_2CS] = 1.5$ M

$[(NH_4)OH] = 30$ %

The bath was placed in water maintained at 85 °C. The samples were rinsed in nanopure deionised water, suspended in a bath containing 150 ml nanopure deionised water, 28 ml ($NH_4)OH$ and 22 ml $CdSO_4$ for 1 minute after which 22 ml of ($NH_2)_2CS$ was added and a further 4.5 minutes suspension of the samples done. Finally, the samples were removed from the bath and rinsed in de-ionized water for 15 to 20 seconds. All the procedures above were conducted in rapid succession and 5.5 minutes was the total time the samples were kept in the bath.

3.5.2 ZnO Layer

The ZnO was deposited in two layers by RF sputtering from $ZnO:Al_2O_3$ (2 % Al_2O_3 by weight) target using the CVC AST 601 system. The first layer was deposited with a sputter gas composition of 2 % O_2 in Ar to give 50 nm thick layer. Its sheet resistance was of order 10^6 Ω/sq. This was followed by a layer deposited with a sputter gas composition of 0.1% O_2 in Ar to give a 500 nm thick layer. The sheet resistance and transmittance for the bilayer layer ZnO were 18 to 20 Ω/sq. and 87 to 88

% respectively. Table 3.7 shows the typical run conditions for the ZnO bilayer deposition.

3.5.3 Ni/Al Front Contact

Electron-beam evaporation was used to sequentially deposit 100 nm Ni and 3 µm Al to form Ni/Al grids with ˜5 % shading loss. The system used consists of a diffusion pumped bell jar equipped with Air/Temescal/ model STIH-270-1 four pocket gun powered by model CV-8 power supply. Inside the e-gun hearth, an electron source produces electrons which are focused on the crucible thereby evaporating the source material. The deposition thickness is monitored by a kronos oscillating quartz crystal monitor. This evaporation is not useful for large area deposition because of non-uniform thickness caused by point symmetry of the design. Typical run conditions are as shown in table 3.8.

Cell areas were delineated by mechanical scribing to give individual cells with area 0.49 cm^2.

3.6 Device Characterization

3.6.1 Light and Dark I-V

Current-voltage measurements give the solar cell parameters such as short circuit current, open circuit voltage, maximum power, fill factor and efficiency. Further analysis of I-V data can give series resistance, shunt resistance, as well as information on current transport mechanism and junction properties.

The I - V data acquisition was made by a Labview computer program. The ORIEL arc lamp light source was calibrated for AM1.5 (or 100 mW cm^{-2}) using a reference single crystal silicon cell at the National Renewable Energy Laboratory, USA.

3.6.2 Spectral Response

Spectral response measurements determine the wavelength dependence of the quantum efficiency (Q) of the solar cell devices. The measurement can provide a considerable amount of qualitative and quantitative information on the device configuration, material properties such as diffusion length [Phillips J. E., 1990], and device properties [Phillips and Roy, 1988].

The Institute of Energy Conversion spectral response system was used in this work. The system consists of an ORIEL arc lamp white light source, a monochromator, and a mechanical chopper operating at 70 Hz. A white light bias (d.c.) is also used to simulate the AM 1.5 radiation. The cell was exposed to the white light and the chopped monochromatic light at wavelengths varying from 400 to 1400 nm in steps of 10 nm. The generated current from the monochromatic light allows computation of quantum efficiency. All the spectral response measurements were carried out at zero voltage bias.

Table 3.1. Sputtering conditions for Mo on soda-lime glass

Target	Mo (1st layer)	Mo (2nd layer)
Base pressure (mbar)	1.6×10^{-7}	1.6×10^{-7}
Sputtering pressure (m bar)	2.1×10^{-2}	6.7×10^{-3}
Current (A)	2	2
Voltage (V)	235 - 240	275 - 280
Power (W)	480 - 470	550 - 560
Deposition rate (Å sec^{-1})	2.8	2.8

Table 3.2. Sputtering conditions for Cu on soda-lime glass

Target	Cu
Base pressure (m bar)	3.0×10^{-6}
Ar flow rate (ml/min.) / sputtering pressure (m bar)	$20 / 2.4 \times 10^{-3}$
DC Power (W)	190
Voltage (V)	519 - 521
Current (A)	0.36 -0.37
Deposition rate (nm sec^{-1})	0.40

Table 3.3. Sputtering conditions for In on soda-lime glass

Target	In
Base pressure (m bar)	3.0×10^{-6}
Ar flow rate (ml/min.) / sputtering pressure (m bar)	$70 / 5.8 \times 10^{-3}$
DC Power (W)	200
Voltage (V)	517 - 520
Current (A)	0.34 - 0.36
Deposition rate (nm sec^{-1})	1.18

Table 3.4. Corresponding Cu and In thicknesses for CuIn precursors.

Precursor	Elemental thickness (μm)	
	Cu	In
(Cu : 0.2500 μm; In : 0.6909 μm)	0.2500	0.6906
(Cu : 0.1250 μm; In : 0.3453 μm)	0.1250	0.3453
(Cu : 0.938 μm; In : 0.2591 μm)	0.0938	0.2591
(Cu : 0.625 μm; In = 0.1727 μm)	0.0625	0.1727

Table 3.5. Sputtering conditions for Cu on Mo-coated soda-lime glass (SL/Mo)

Target	Cu
Base pressure (mbar)	1.9×10^{-7}
Sputtering pressure (m bar)	6.7×10^{-3}
Power (W)	200
Voltage (V)	441 - 443
Current (A)	0.46 - 0.47
Deposition rate (Å sec^{-1})	4.8

Table 3.6. Sputtering conditions for In on Mo - coated soda-lime glass (SL/Mo)

Target	In
Base pressure (mbar)	1.9×10^{-7}
Sputtering pressure (m bar)	6.7×10^{-3}
Current (A)	0.6
Voltage (V)	427 - 430
Power (W)	260 - 262
Deposition rate (Å sec^{-1})	6.4

Table 3.7. Typical run conditions for ZnO bilayer

Target	ZnO (1st layer)	ZnO (2nd layer)
Base pressure (mbar)	2.0×10^{-6}	2.0×10^{-6}
Sputtering pressure (mbar)	4×10^{-3}	4×10^{-3}
O_2 gas	2% in Ar	0.1% in Ar
RF power (forw/refl) (W)	900 / 35	900 / 35
Voltage (V)	2.48	2.48
Deposition rate (Å sec^{-1})	16.7	16.7

Table 3.8. Typical run conditions for Ni/Al grids

Material	Ni	Al
Targeted thickness (Å)	1000	30,000
Deposition rate (Å/sec.)	18	45
Kronos thickness (Å)	1000	30,000
Emission control set	0.65	0.63
Base pressure (mbar)	1.5×10^{-6}	1.7×10^{-6}
Deposition pressure (torr)	2.1×10^{-6}	2.7×10^{-6}
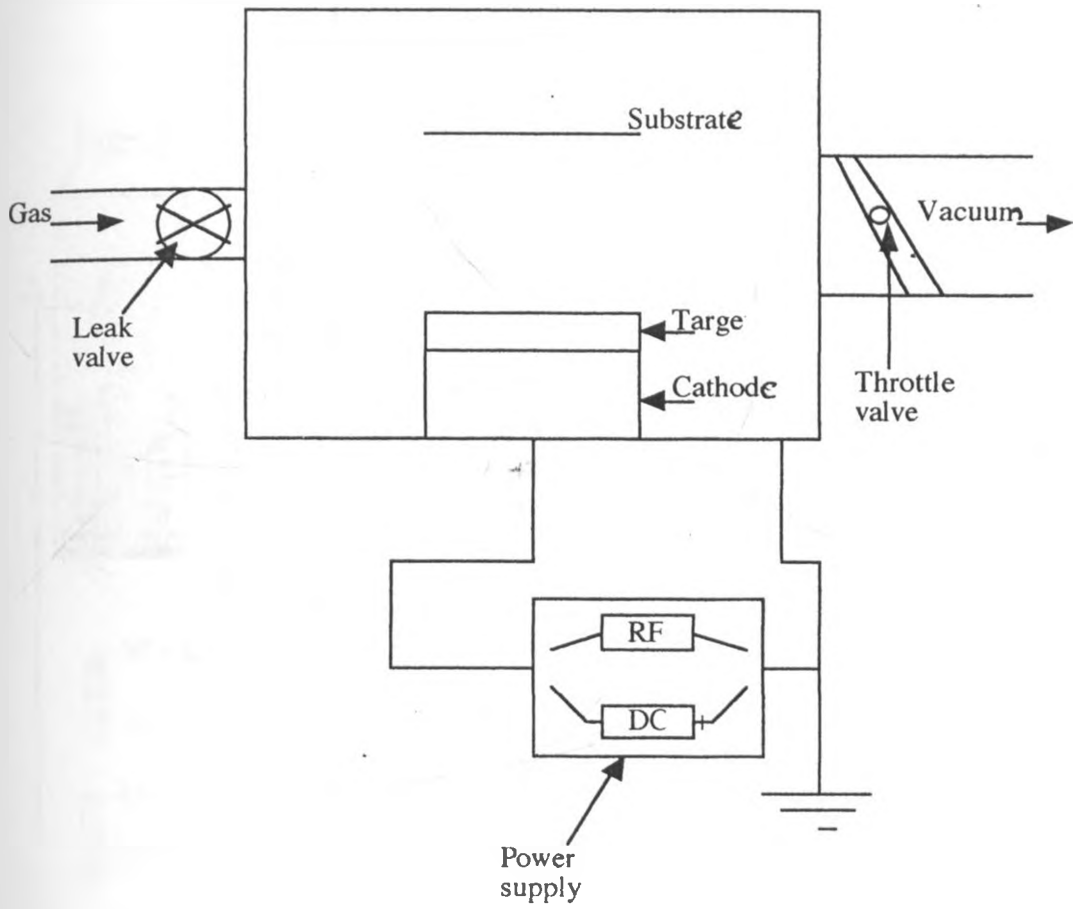
Figure 3.1 General schematic diagram of a sputtering system.

89
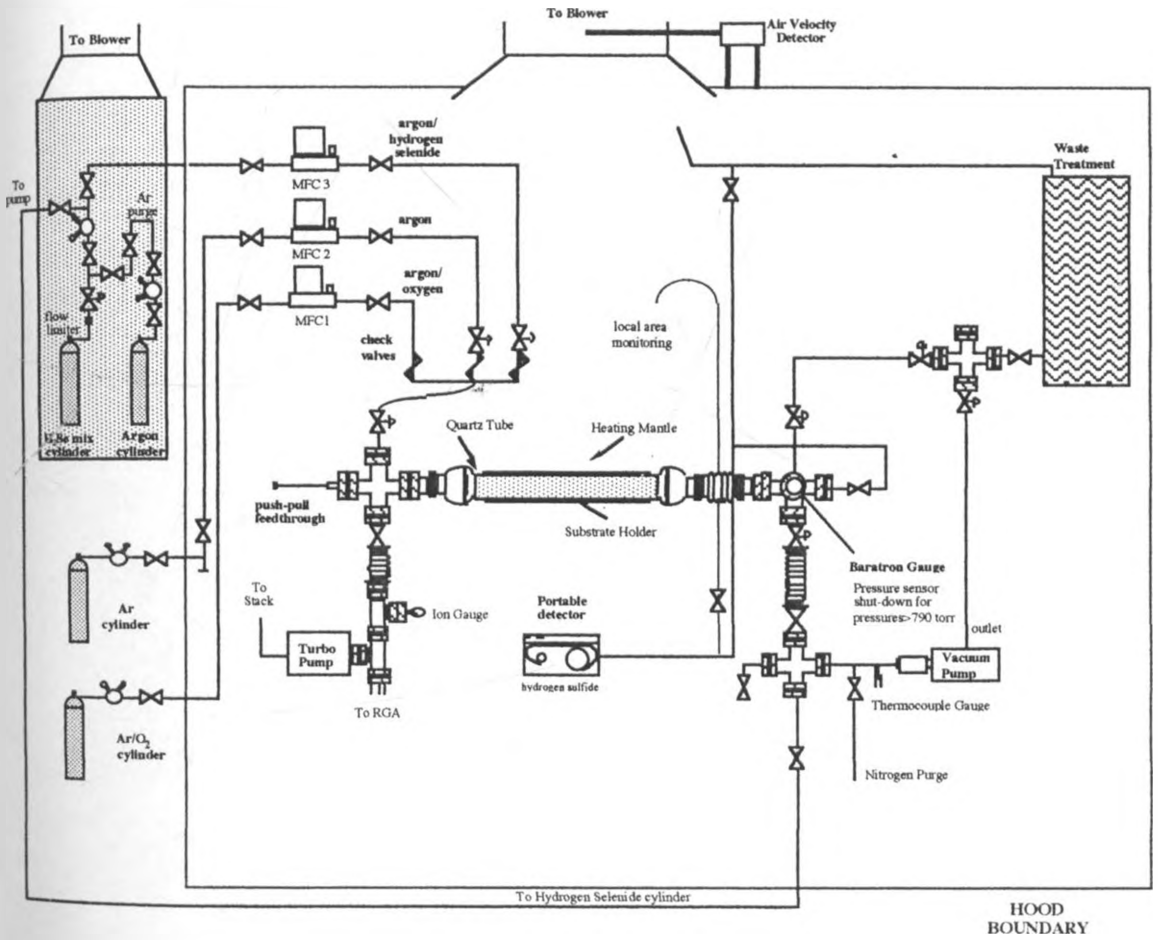
Figure 3.2. Schematic drawing of the selenization reactor.
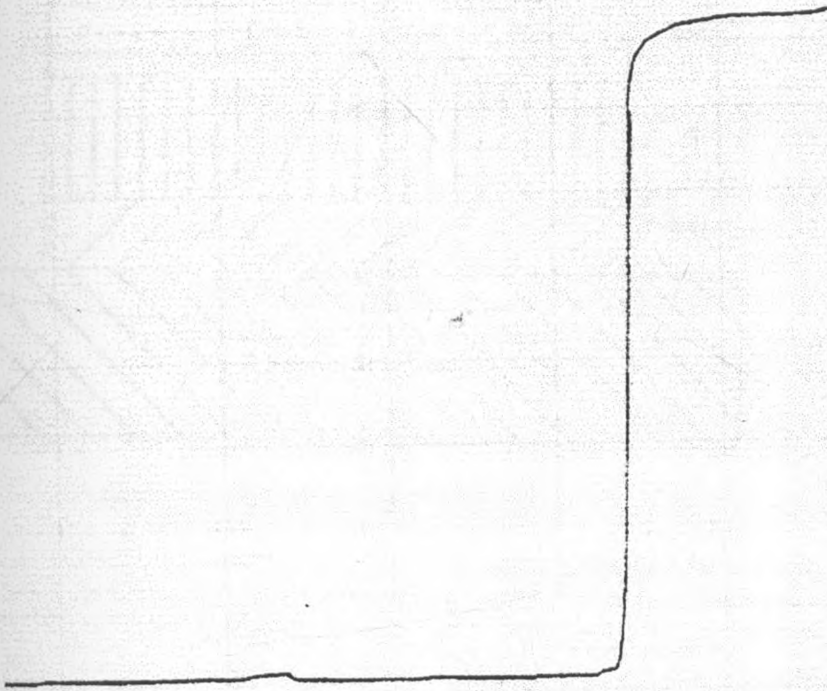
Figure 3.3. Typical trace for a dektak

Al (3 μm)
Ni (100 nm)
ZnO (550 nm)
CdS (40 nm)
CuInSe2

Mo (1 μm)

Soda lime glass
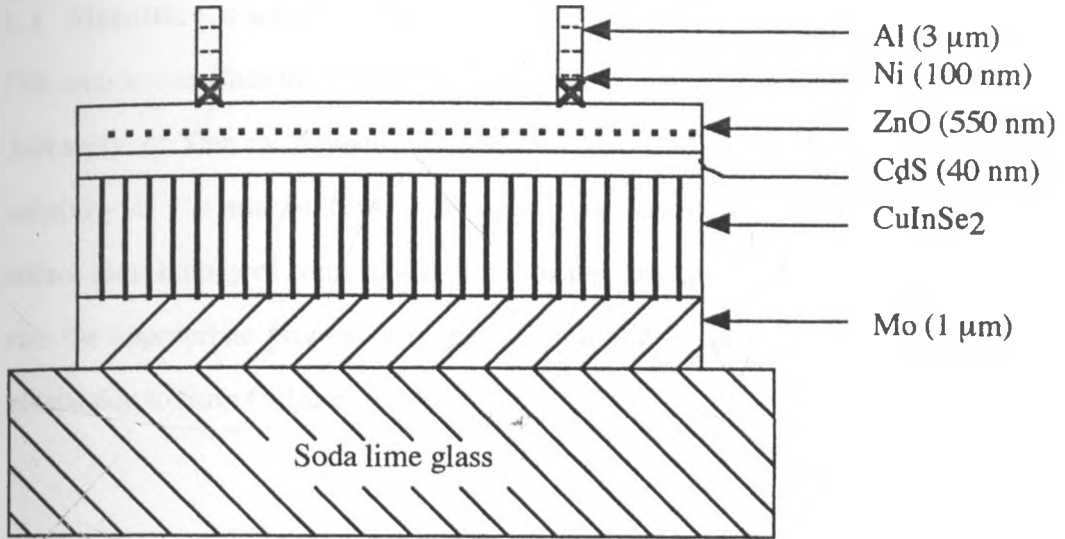
Figure 3.4 Solar cell structure. CuInSe₂ thicknesses used in this work were 2.2, 1.4, 0.8 or 0.6 μm.

CHAPTER FOUR

RESULTS AND DISCUSSION

4.1 Metallic Cu and In Films

This section describes the results of studies carried out at the Solar Energy Laboratory, University of Dar es Salaam, Tanzania. The studies involved the variation of resistivity of Cu and In films with sputtering conditions. Optical properties and surface morphology of some of the films are also presented. These results provide us with the appropriate properties of metallic Cu and In films in the CuIn bilayer for selenization to form $CuInSe_2$ films.

4.1.1 Cu Films

The resistivity of Cu films was found to decrease with decreasing sputtering pressure, increasing film thickness, increasing magnetron power, and decreasing base pressure. Figure 4.1 shows the variation of resistivity and deposition rate with sputtering pressure. The resistivity increased from 2.8 to 5.2×10^{-8} Ωm while the deposition rate decreased from 0.36 to 0.22 nmsec^{-1} when sputtering pressure was increased from 1.7 to 7.9×10^{-3} mbar. The increase in resistivity with increasing sputtering pressure is caused by multiple scattering due to increase in collisions between Cu atoms and Ar ions in the chamber which results in low adatom surface diffusion. The low adatom diffusion means that the growing thin film is not able to overcome the effects of geometric shadowing resulting into films with open boundaries which exhibit high resistivities [Musil et. al., 1995]. Increase in sputtering pressure in the sputtering chamber also results into an increase in residual gas (water vapor and its dissociation

products outgassed from the chamber surface) [Craig and Harding, 1981B]. It was suggested that this might involve agglomeration of as deposited surface layers of the films. The decrease in deposition rate with increasing sputtering pressure can also be due to more Ar-Cu collisions and thermolization as is the case for a-Si [Thompson, 1984].

Figure 4.2 shows that resistivity decreases with increase in deposition temperature. This agrees with other workers [Musil et. al, 1985; Craig and Harding, 1981B] where they observed a decrease in resistivity with deposition temperature. They explained their results in terms of low adatom mobility at room temperature and a well developed crystallization process at higher deposition temperature responsible for high and low resistivities, respectively. TEM micrographs for Cu films (figure 4.3) deposited at different temperatures showed an increase in grain size at high deposition temperature. The increase in grain size resulted in decrease of grain boundaries which explain the decrease in resistivity with increase in deposition temperature. Low resistivity for thicker Cu films is expected as they exhibit properties similar to those of bulk material.

Figure 4.4 shows that resistivity of copper films decreases with increase in magnetron power. The decrease in resistivity from 4.5×10^{-8} Ωm to 2×10^{-8} Ωm with increase in magnetron power from 50 W to 300 W is due to higher surface diffusion caused by higher deposition rate and in turn minimal agglomeration. The higher deposition rate is caused by higher kinetic energies of the incident coating atoms when operating at higher magnetron powers.

Variation of Cu film resistivity for the 34 nm thick Cu film with base pressure is shown in figure 4.5. Low base pressure produced low resistivity films which was expected because of less impurities at low vacuum pressures. Poor vacuum usually

results in target oxidation (poisoning) which is transferred to the film. Oxidation can also occur at the film surface due to oxygen partial pressures present in the chamber.

4.1.2 Indium Films

Except for variation with magnetron power and base pressure, the resistivity of In films behaved differently to that of Cu films. The resistivity decreased abruptly for sputtering pressure of 1.7 to 3.0×10^{-3} mbar and remained almost constant for sputtering pressure of between about 4.5 and 7.9×10^{-3} mbar (figure 4.6). This cannot be explained at the moment but the decrease in deposition rate from 0.85 to 0.52 nmsec^{-1} for sputtering pressure increase from 1.7 to 7.9×10^{-3} mbar can be explained the same way as for Cu films. The resistivity of the films deposited at room temperature were found to decrease abruptly with increase in thickness. Figure 4.7 shows that resistivity change is of the order 10^9 for a change of film thickness from 33 nm to 221 nm. This can be because of the discontinuous nature observed for thinner In film hence higher resistivity than the thicker films. The color of the film was also observed to change with the thickness (see table 4.1). This can be attributed to changes in texture for different In thickness (figure 4.8). SEM picture (figure 4.8) for In films of different thicknesses shows fewer grain boundaries for thicker films than for thinner films. This suggests that thicker In films are more continuous and compact than thinner films.

Figure 4.9 shows reflectance data for DC sputtered In films for different thicknesses. Consistent red shift of the edges at the higher energy side with increase in film thickness is observed. This can explain the change in color of the films for different thicknesses. Reflectance is higher for thinner films in the visible region (i.e. $\lambda = 300$ -

700 nm. The decrease in reflectance for thicker films in the visible range can be associated with island growth mechanism for In film with thicker films exhibiting large grain sizes hence low specular reflectance. This has been confirmed by SEM pictures (figure 4.8) of In films of different thicknesses.

Figure 4.10 shows the variation of resistivity with deposition temperature for 221 nm thick films. The resistivity is in the range of 16.0 to 40.0 x 10^{-8} Ωm at deposition temperature between 25 and 120 °C, increases abruptly from about 40.0 x 10^{-8} Ωm to 4.0 x 10^{-4} Ωm (change of order 10^{11}) for deposition temperature of about 150 to 200 °C. Generally the films exhibit abrupt change from low resistivity to high resistivity for deposition temperature between 140 to 160 °C. This might be due to change of In film from solid phase to liquid phase; the melting temperature of In is about 157 °C [Kaye and Laby, 1971]. A similar abrupt change has been observed for variation of resistivity with thickness (see figure. 4.7).

4.2 CuIn Bilayers

Both as grown and heat treated CuIn bilayers had the same surface morphology. Figure 4.11 shows a typical SEM picture for CuIn bilayer on a Mo coated soda lime glass. The surface morphology clearly shows separated indium islands. This morphology is consistent with other workers [Marudachalam, 1996; Verma, 1993] for indium films deposited by sputtering and evaporation. The indium islands are preferred to be closely separated or interconnected otherwise they might limit lateral diffusion during selenization of the precursors. Increase of deposition rate for In film

while keeping that of Cu film the same improves the morphology of the CuIn bilayer (figure 4.12).

The phases present in as grown CuIn bilayer on Mo coated soda lime glass are In, Cu, CuIn (figure 4.13). CuIn bilayers on Mo coated soda lime glass heat treated in Ar at 200 °C for 30 minutes exhibited In, $Cu_{11}In_9$ and an unidentified phase (figure 4.14). These XRD results are consistent with initial phases assumed in the kinetic model.

Other workers observed a combination of slightly different phases from ours for both as grown and annealed CuIn bilayers. Cu, In, and $CuIn_2$ phases were observed for CuIn bilayers deposited by electron beam evaporation and on annealing at 200°C for 30 minutes, $Cu_{11}In_9$ and In phases resulted [Verma, 1993]. Gupta et. al., (1994) observed Cu, In, Cu_4In, and Cu_7In_4 for thermal evaporated CuIn bilayers. Annealing the bilayers in vacuum at 200°C for 15 minutes preserved the phases observed but the amount of Cu_7In_4 increased. RF sputtered CuIn bilayers at room temperature yielded $Cu_{11}In_9$, $CuIn_2$, In and Cu phases [Parretta and Rubino, 1995]. On annealing at 150 °C for one hour, only $Cu_{11}In_9$ and In phases were observed.

4.3 $CuInSe_2$ Films

This section describes the surface morphology, composition, phases observed, and optical properties for the $CuInSe_2$ thin films fabricated in this work. Comparison of kinetic model with XRD data and a semi quantitative description of $CuInSe_2$ formation with selenization parameters and precursor thickness are also presented.

CuIn elemental precursor thickness and their corresponding average thickness after selenization are given in table 4.2. The selenized CuIn precursor (i.e. CuInSe$_2$ films) thicknesses are 2 to 3 periods more than that of as grown CuIn precursors. This is due to volume expansion during selenization in agreement with other workers [Alberts and Swanepoel, 1996]. In the next sections, the results (tables, graphs and text) have been presented either in terms of the precursor thickness or the average CuInSe$_2$ thickness for simplicity.

4.3.1 Influence of Precursor Thickness on the Reaction Period for Fixed Reaction Temperature

Samples prepared at reaction temperature of 350 °C were used for studying the effect of precursor thickness on the reaction period for formation of CuInSe$_2$ films as more changes especially in composition of selenized CuIn precursors were observed. The main features considered are phases, surface morphology and composition.

Table 4.3 shows XRD data with reaction period for different precursor thickness. The phases present in the selenized CuIn bilayers are CuInSe$_2$, InSe, and two unidentified peaks. Precursor thickness (Cu : 0.2500 µm; In : 0.6906 µm) exhibited CuInSe$_2$ and InSe phases for all reaction periods and one unidentified phase (peak $^{++}$) for reaction periods of 15 and 30 minutes. Precursor thicknesses of (Cu : 0.1250 µm; In : 0.3453 µm) and (Cu : 0.0938 µm; In : 0.2591 µm) exhibited single phase CuInSe$_2$ for reaction periods from 30 to 90 minutes. Both CuInSe$_2$ and InSe phases were observed for reaction period of 15 minutes. Single phase CuInSe$_2$ only was observed for precursor thickness (Cu : 0.0625 µm; In : 0.1727 µm) for all reaction periods.

For reaction periods studied in this work, the order in which the phases were observed with respect to reaction period agree with earlier workers [Orbey et. al., 1998; Orbey et. al., 1997; Verma et. al., 1996; Verma, 1993]. This is consistent with the kinetic model where $CuInSe_2$ formation by selenization of CuIn bilayers occurs in three stages. Metallic phases appear first, followed by selenides and then finally ternary selenides. Metallic phases ($Cu_{11}In_9$ and In) and In_2Se are usually observed for reaction periods less than 15 minutes.

An analysis of the effect of precursor thickness on the formation of $CuInSe_2$ films at fixed reaction temperature and period is given in table 4.4. It is only the thinner precursor (Cu : 0.0625 μm; In :0.1727 μm) which exhibited single phase of $CuInSe_2$ for reaction period of 15 minutes.

It is clear from tables 4.3 and 4.4 that, for thinner samples at short reaction periods, second phases are not present. This is probably because we were not able to detect the second phases by XRD. The samples are about 0.6 μm thick and hence might have a small fraction of the second phase.

Table 4.5 shows composition data with reaction period for different precursor thicknesses selenized at reaction temperature of 350 °C. Its graphical representation is given in figure 4.15. Within experimental errors, the at. %'s for Cu, In and Se and the Cu/In ratio did not change with reaction period for a given $CuInSe_2$ thickness at reaction temperature of 350 °C. Hence the results for one reaction period can be taken to be a representative of all reaction periods investigated at this temperature. Changes in at. % with precursor thickness are mainly due to Cu and Se. At. % of In is constant

at about 24 to 25 % range for all precursor thicknesses. At. % Cu and Se vary from about 26 to 19 % and 49 to 57 %, respectively for precursor thickness decrease from (Cu : 0.2500 μm; In : 0.6906 μm) to (Cu : 0.0625 μm; In : 0.1727 μm) (i.e. $CuInSe_2$ thickness decrease from 2.2 to 0.6 μm). EDS measurements for $CuInSe_2$ thicknesses less than 1.0 μm might have errors [Rocket and Birkmire, 1991]. However, for $CuInSe_2$ films of more than 1.0 μm thick with selenium content less than 50 % can be attributed to an incomplete chalcogenization of metallic layers.

Although the intended Cu/In ratio for the Cu/In bilayers is maintained at 0.8 (see table 4.6 showing confirmed EDS data for heat treated CuIn bilayers of different thickness), the Cu/In ratio for the selenized precursors was found to be higher for thicker $CuInSe_2$ films and closer to the intended Cu/In ratio for thinner films. These results suggest that either there is more In loss in selenizing thicker CuIn bilayer than thinner ones or the EDS measurements for thinner $CuInSe_2$ have errors. Absence of In loss for thinner CuIn precursors might be explained in terms of the shorter periods needed to fully react thinner CuIn bilayer, hence complete reaction takes place before In loss starts occurring. Parretta [1995] also observed indium loss at 350 °C when he used closed spaced vapor transport process in selenizing CuIn bilayers. At this temperature, he also observed decomposition of the $Cu_{11}In_9$ phase. The decomposition of $Cu_{11}In_9$ phase probably lets indium free to evolve as In_2Se in the gas phase or to form $CuInSe_2$ thin film. In loss during selenization is consistent with published values of vapor pressures of In_2Se and Se_2 over $CuInSe_2$ [Strel'chenko et. al., 1969]. In_2Se exhibits a considerably higher vapor pressure than Se_2 over a wide temperature range for nominally stoichiometric $CuInSe_2$. The same explanation was given for In loss during vacuum vapor phase crystal growth at temperatures above 400

°C for both the three source evaporation [Jackson et. al, 1987] and the hybrid sputtering and evaporation [Rocket et. al., 1988] process. For the 0.6 µm thick CuInSe$_2$ films, the Cu/In ratios values measured are slightly less than the intended values. This might be due to the EDS experimental errors in measuring the composition for thinner film, otherwise we believe that the Cu/In ratio is 0.8 (same as the one intended). To achieve higher accuracy, EDS system must be thermally and electronically stable and films must be in excess of 1 µm thick and compositionally homogeneous [Rocket and Birkmire, 1991].

It is difficult to correlate surface morphologies with precursor thickness or reaction period but one predominant feature is the difference in morphologies for a fully reacted precursor and one which is partially reacted [figure 4.16]. Fully reacted precursors have small compact grains of about 1.5 to 3 µm diameter. The precursors which are partially reacted consists of big grains of diameter ranging from 4 to 8 µm. Some precursors which are partially reacted exhibit cavity like structures. This can be explained in terms of better crystallization for fully reacted films.

4.3.2 Influence of Reaction Temperature on the Reaction Period for Fixed Precursor Thickness

The phases observed for reaction temperatures and periods investigated in this work are CuInSe$_2$, InSe, MoSe$_2$, and two unidentified peaks (table 4.7). Figure 4.17 shows XRD traces for a CuInSe$_2$ samples which exhibited most of the phases observed in this work. MoSe$_2$ phase was only found in films selenized at reaction temperature of 500 °C. The unidentified peaks did not exhibit any pattern; they were

scattered randomly. The presence of $MoSe_2$ phase at high reaction temperature is consistent with an earlier work by Marudachalam, 1998, where he observed the phase for selenized Mo coated 7059 glass at 550 °C for 90 minutes (figure 4.18).

No correlation was found for composition of $CuInSe_2$ films with respect to reaction temperature (table 4.8). This is in contradiction with that of Satoshi et. al., (1993) where In loss was observed to increase with reaction temperature.

Surface morphology of selenized CuIn precursors was found to change with reaction temperature. Figure 4.19 shows typical SEM morphologies for CuIn precursors selenized at different reaction temperatures. Precursors reacted at reaction temperatures of 350 and 400 °C had almost the same surface morphologies with grain sizes of between 2 and 4 µm diameter. At reaction temperature of 450 °C, destruction of film morphology is observed as the films are non uniform. Complete destruction is observed at reaction temperature of 500 °C especially for CuIn precursor thickness of (Cu : 0.1250 µm; In : 0.3453 µm). The films are characterized by wide cracks. This can be attributed to higher reaction rate constant for higher temperature (see table E.1 in appendix E for calculated reaction rate constants for different reaction temperatures) leading to rapid and uncontrolled incorporation of Se into the CuIn bilayer and the corresponding volume expansion during selenization.

4.3.3. Comparison of Kinetic Model with XRD Data

$CuInSe_2$ and InSe number of moles calculations were used to compare the kinetic model and XRD data. In the kinetic model mole calculations, only In and $Cu_{11}In_9$

phases were assumed present in the CuIn bilayer before selenization. The initial number of moles calculations in the CuIn precursors are given in table E.2 in appendix E. Discretizing the mass balance equations in table 2.3 and using $V_f = \sum_i N_i \dfrac{MW_i}{\rho_i}$ for the film volume, the number of moles for each phase was obtained by multiplying the film volume by its concentration. Details of moles calculations using XRD data are given in section 3.4.1.5.1.

Comparison of kinetic model and XRD data was only done for reaction temperatures of 350, 400 and 450 °C and all precursor thickness in case of $CuInSe_2$ phase. It was not done at reaction temperature of 500 °C because of the presence of $MoSe_2$ phase which is not in the kinetic model equations (table 2.3). For InSe phase, it was only done for (Cu : 0.2500 µm; In : 0.6906 µm) precursors reacted at 350 °C as these were the only samples with InSe phase in all reaction periods investigated.

Figure 4.20 shows predicted and experimental number of moles of $CuInSe_2$ versus reaction period for reaction temperatures of 350, 400 and 450 °C. Both predicted and experimental number of moles plateau after some reaction period with the asymptote reaching faster for higher reaction temperature. This is consistent with higher reaction rate constants calculated for different reaction temperatures (appendix E). Although the plateuing of predicted number of moles is independent of precursor thickness, experimental number of moles show that thinner precursors moles plateau faster than the thicker precursors. These results suggest that there is a second process that is involved in the reaction which will depend on film thickness. Most likely, the assumption that there is excess Se as the reaction approaches to completion probably is not valid. Towards the end of the reaction, the reaction is mostly limited by diffusion

of Se into the film. That is, the Se must diffuse into the film (which is mostly $CuInSe_2$) to react with binary phases. For reaction temperature of 450 °C, time resolution is poor hence no difference in period to reach asymptote for both (Cu : 0.2500 μm; In : 6906 μm) and (Cu : 0.1250 μm; In : 0.3453 μm) precursors. Generally, predicted and experimental number of moles agree best for thinner precursors reacted for more than 30 minutes.

Predicted and experimental number of moles for InSe versus reaction period for reaction temperatures of 350 °C is shown in figure 4.21. Good agreement , especially in shape for reaction periods of 15 to 30 minutes is observed between predicted and experimental curves. Experimental curve for reaction periods of 45 to 90 minutes suggests that InSe phase depletion is faster than that predicted in the model.

4.3.4. Optical Properties

In this work, the only optical measurement reported for $CuInSe_2$ films with respect to selenization conditions and $CuInSe_2$ thickness is reflectance. This is because $CuInSe_2$ films were grown on Mo coated soda lime glass. Attempts to grow $CuInSe_2$ on half coated soda lime glass with molybdenum so as to measure both transmittance and reflectance for $CuInSe_2$ films on uncoated soda lime glass for absorption coefficient calculations was unsuccessful as the films had different surface morphologies (figure 4.22). In addition, the $CuInSe_2$ films on uncoated soda lime glass were not uniform; visually some parts were more transparent than others. However, in spite of the non uniformity of $CuInSe_2$ film sample on uncoated soda lime glass, an idea of absorptance with wavelength of the $CuInSe_2$ film was obtained from transmittance and reflectance data. Figure 4.23 shows total transmittance for bare soda lime glass and

CuInSe$_2$ on soda lime glass. Absorptance and total reflectance for CuInSe$_2$ film on soda lime glass are also shown. The CuInSe$_2$ film on soda lime glass clearly exhibits strong absorption (between 0.80 and 0.83) in the wavelength range 700 to 1200 nm and low absorption (between 0.20 and 0.25) for wavelength greater than 1300 nm.

Figure 4.24 shows a reflectance spectra for CuInSe$_2$ on Mo coated soda lime glass. As expected, it shows a dependence on reaction period and thickness. Reflectance is higher for films reacted for long periods (figure 4.24a) for wavelength range investigated in this work. This is consistent with the morphologies observed in figure 4.16 and the discussion in the last paragraph of section 4.3.1 for fully reacted precursors and those which are partially reacted (short reaction periods). Films with smooth and compact grains of small grain size should have higher reflectance than films with rough grains containing cavity like structures. The same explanation can be given for reflectance data with precursor thickness (figure 4.24b).

CuInSe$_2$ film on uncoated soda lime glass is almost opaque (transmittance < 0.05) and transmittance for uncoated soda lime glass is almost constant at about 0.9 (figure 4.23) for wavelength range 700 to 1200 nm. This therefore means that reflectance data in this wavelength range can give us information about absorption of CuInSe$_2$ films. Using relation, $A_{ab} = 1 - (T_{trasm} + R_{refl})$, where A_{ab} is the absorptance, T_{transm} is the total transmittance and R_{refl} is the total reflectance, the films can be said to exhibit strong absorption for thicker CuInSe$_2$ films and lower reaction periods. These observations, especially with respect to CuInSe$_2$ thickness, are mainly attributed to surface texture as explained in the preceding paragraph. Transmission and reflectance do not depend on thickness. The magnitudes and shapes of the spectra are comparable with similar films grown at ENEA, Italy[Parretta, 1993]. The reflectance spectra clearly shows two zones: one for high wavelengths (λ > 1300 nm) with reflectance in

the range 25 to 35 %, and another one for low wavelengths (λ < 1300 nm) in which the reflectance decreases steeply and then gradually approaches 15 %. These zones correspond to the weak and strong absorption regions, respectively for CuInSe$_2$ thin films in agreement with the absorptance curve for CuInSe$_2$ films in figure 4.23.

The reflection from a surface depends on the index of refraction of the media that the light is incident on and the media it is entering, in our case air and CuInSe$_2$. For a semiconductor, there is a change in index as you go from the high absorption region (i.e. light having energy greater than the band gap) to the transparent region (light having energy less than the band gap). Thus, the steep increase in reflection for $\lambda \approx$ 1200 to 1300 nm is due to a change in the index of refraction [Hecht, 1998].

4.3.5 Semi Quantitative Description of the Effect of Reaction Period, Reaction Temperature and Precursor Thickness on Formation of CuInSe$_2$ Films

In order to give a semi quantitative description on what is happening with respect to one parameter in CuInSe$_2$ formation, it is important to keep the other parameters fixed.

• Effect of reaction period at fixed reaction temperature and precursor thickness.

Assuming that reactions which occur early in selenization at high temperatures are similar to those at low temperatures for longer periods and using results for other workers [Orbey et. al., 1997; Verma et. al., 1996; Verma, 1996] for reaction periods

less than 15 minutes, the following progressive description with respect to reaction period can be given:

1. At the start of selenization process, CuIn bilayer is converted to solid $Cu_{11}In_9$ and liquid In phase through diffusion and interdiffusion.
2. $Cu_{11}In_9$ plus In reacts with Se to form $InSe_2$ and Cu_2Se.
3. In reacts with Se to evolve as In_2Se in the gas phase or InSe.
4. InSe plus Cu_2Se react with Se to form $CuInSe_2$
5. Completion of the reaction is most likely limited by diffusion which depends on the precursor thickness.
6. $CuInSe_2$ crystal growth from large and rough islands of diameter 4 to 8 µm with cavity like structures and boundaries to smooth and compact crystals of grain size 2 to 4 µm.

- Effect of reaction temperature at fixed reaction period and precursor thickness.

Reaction rate increases with temperature. The period to fully react the precursors depends on reaction temperature; less period is required at higher temperature and vice versa. Rapid and uncontrolled incorporation of Se into the CuIn bilayer leading to non uniformity of $CuInSe_2$ films starts at 450 °C due to high reaction rate. At reaction temperature of 500 °C, apart from destruction of film due to high reaction rate, $MoSe_2$ phase starts appearing as well.

- Effect of precursor thickness at fixed reaction temperature and period

Reaction rate is the same. The period for the film to fully react is independent of the thickness of the precursors. Measured Cu/In ratio of selenized CuIn precursors changes with precursor thickness.

4.4 CuInSe$_2$ Solar Cells

Solar cell parameters for all solar cells fabricated in this work is shown in table 4.9. Analysis of the device performance with respect to reaction period, reaction temperature and CuInSe$_2$ thickness is given in subsequent sections.

4.4.1 Device Performance with respect to Reaction Period and Temperature

Efficiency versus reaction period curves for different reaction temperatures are shown in figure 4.25. A trend is observed for efficiency at reaction temperatures of 350 and 400 °C where efficiency increases with reaction period. This is consistent with CuInSe$_2$ and InSe moles calculated using both the XRD data and kinetic model (figures 4.20 and 4.21) where the number of moles for CuInSe$_2$ were found to increase with reaction period and the InSe phase was found to deplete with reaction period after its formation. Although the presence of InSe phase implies incomplete selenization, the highest efficient cell (10.6 %) in this work was obtained for an absorber layer with a trace of InSe phase (compare tables 4.3 and 4.9). This means that good devices with efficiencies greater than 10 % can be obtained provided the number of moles for InSe phase is less than 2×10^6. Efforts by other workers

[Verma, 1993] to fabricate solar cells with CuIn precursors reacted for longer reaction periods (period > 90 minutes) showed that the increase in efficiency was negligible and hence uneconomical.

Efficiencies for reaction temperatures of 450 and 500 °C with reaction period were almost constant. They varied from 6.5 to 7.5 % and 2.0 to 3.5 % for reaction temperatures of 450 and 500 °C, respectively. Low efficiencies for reaction temperature of 500 °C is consistent with XRD data where $MoSe_2$ phase was found to be present in all the samples. Non uniformity and cracking of the $CuInSe_2$ films due to high reaction rate is also believed to be a contributing factor to the low efficiencies at reaction temperature of 450 and 500 °C, respectively (compare figures 4.25 and 4.19).

Light and Dark J - V curves for solar cells fabricated using $CuInSe_2$ thin films selenized for different periods is shown in figure 4.26. The curves bulge outwards with increasing reaction period and this can be seen to mainly due to change in open circuit voltage and fill factor. For solar cell using $CuInSe_2$ films selenized for 15 minutes, in addition to change in open circuit voltage, a change in short circuit current is also observed. This may be due shorting between Mo back contact and Al/Ni front contact due to incomplete reacted CuIn bilayer.

Quantum efficiency curves from the spectral response measurements of the solar cells fabricated using absorber layer selenized for 15, 30 and 60 minutes is shown in figure 4.27. Both curves are typical of $CuInSe_2$ solar cells. The integrated quantum efficiencies are 28.76, 29.00 and 34.92 mA for absorber layer selenized for 15, 30 and 60 minutes, respectively. The fall-off of quantum efficiency curve for absorber

layer selenized at 15 and 30 minutes might be due to a change in absorber structure due to incomplete selenization process.

4.4.2 Device Performance with respect to Reaction Temperature at Fixed Reaction Period and Precursor Thickness

To understand the effect of reaction temperature at fixed reaction period and precursor thickness for $CuInSe_2$ based solar cells, figure 4.28 was plotted. At reaction period of 15 minutes, efficiency for solar cell with precursor thickness (Cu : 0.2500 μm; In : 0.6906 μm) was zero for all reaction temperatures except for reaction temperature of 500 °C where it was 3.8 %. For precursor thickness of (Cu : 0.1250 μm; In : 0.3453 μm), the solar cell efficiency increased from 0.0 to 6.7 % for increase in reaction temperature from 350 to 450 °C and then decreased to 3.2 % for reaction temperature of 500 °C.

At reaction periods of 60 minutes, for both precursor thicknesses, solar cell efficiencies increased for reaction temperature from 350 to 400 °C and then decreased for reaction temperatures of 450 and 500 °C.

For precursor thickness of (Cu : 0.2500 μm; In : 6906 μm), it increased from 0.0 to 9.6 % for increase in reaction temperature from 350 to 400 °C and then decreased to 4.8 for reaction temperature of 500 °C. The efficiency of the cells using precursor (Cu : 0.1250 μm; In : 0.3453 μm) increased from 9.8 to 10.5 % for increase in

reaction temperature from 350 to 400 °C and then decreased to 3.0 % for reaction temperature of 500 °C.

Assuming a good device has efficiency greater than 8 % is obtained using fully reacted CuIn precursors and correlating this with the $CuInSe_2$ films results obtained, three explanations can be given for these device results. Firstly, low reaction temperatures require long reaction periods while high reaction temperatures require shorter reaction periods. Secondly, although the period for the films to fully react is independent of the precursor thickness, the periods for predicted and experimental varied slightly. This has been explained in terms of a second process that is involved in the reaction which depends on film thickness (see section 4.3.3 for details). Lastly, at reaction temperatures greater than 400 °C, apart from changes in structure for selenized CuIn bilayers (i.e. destruction of $CuInSe_2$ films), $MoSe_2$ phase formation also deteriorates the device performance. The film destruction, which is more predominant for thinner precursor, is due to high reaction rate constants at higher reaction temperature in the $CuInSe_2$ formation during selenization.

Solar cell efficiencies with reaction temperature could not be explained in terms of $CuInSe_2$ film composition because no correlation was found between composition and reaction temperature (see table 4.8).

4.4.3   Device Performance with respect to Reaction Period at Fixed Reaction Temperature

Device performance with respect to reaction period at fixed reaction temperature for precursors of different thicknesses is given in figure 4.29. Trends similar to device

performance with respect to reaction period for different reaction temperature are observed (compare with figure 4.25). Solar cell efficiencies for precursors (Cu : 0.1250 µm; In : 0.3453 µm) and (Cu : 0.0938 µm; In : 0.2591 µm) increased with reaction period. This can be explained the same way as for device performance with respect to reaction period for reaction temperatures 350 and 400°C (section 4.4.1).

For the thicker precursor (Cu : 0.2500 µm; In : 0.6906 µm), the solar cell efficiency is zero for all reaction periods except for reaction period of 90 minutes where it is 2.3 %. The zero efficiencies might be attributed to shorting between the Mo back contact and the Ni/Al grids due to incomplete reacted precursors. The low efficiency at reaction period of 90 minutes might be associated with the second process that is involved in selenization which depends on precursor thickness (see section 4.3.3 for details).

Solar cell efficiency for the thinner precursor (Cu : 0.0625 µm; In : 0.1727 µm) is independent of reaction period. Efficiencies lie between 7.0 and 8.0 % for all reaction periods. These results suggest that for each precursor thickness, there is a limit in efficiency which can be obtained. The limit in efficiency is not directly dependent on precursor thickness but it might be a balance between precursor thickness and probably absorption of light especially for thinner precursors.

From table 4.5, the average Cu/In ratio are 1.05, 0.94, 0.85, and 0.78 for selenized precursors (Cu : 0.0625 µm; In : 0.1727 µm), (Cu : 0.1250 µm; In : 0.3453 µm), (Cu : 0.0938 µm; In : 0.2591 µm), (Cu : 0.0625 µm; In : 0.1727 µm), respectively. The slightly In rich selenized precursors (Cu/In = 0.94) produced the best cells which is in agreement with other workers [Rocheleau et. al., 1987].

4.4.4 Device Performance with respect to Precursor Thickness at Fixed Reaction Period

The graphical presentation and explanation in this section has been given in terms of $CuInSe_2$ absorber thickness (i.e. selenized CuIn thickness) for simplicity. For corresponding precursor thicknesses, refer to table 4.2. Figure 4.30 shows graphs for efficiency versus $CuInSe_2$ thickness for different reaction periods. Generally, efficiency exhibit two patterns with increase in $CuInSe_2$ thickness from 0.6 to 2.2 μm; one pattern is for reaction periods of 15 and 30 minutes and the other for reaction periods of 60 and 90 minutes. Efficiency decreases with increase in thickness for reaction periods of 15 and 30 minutes (figure 4.30). For 60 and 90 minutes reaction periods, efficiency increase with thickness up to maximum of about 10 % for thickness of 1.4 μm and decreases abruptly to 2.28 % and 0.00 % for reaction periods of 90 and 60 minutes, respectively for film thickness of 2.2 μm.

Although the maximum efficiencies were not reached for reaction periods of 15 and 30 minutes for $CuInSe_2$ thicknesses investigated in this work (figure 4.30), the trend suggests that for each reaction period there is a limiting $CuInSe_2$ thickness which gives the highest efficiency. Assuming that higher efficiencies are obtained for fully reacted CuIn bilayers during selenization, these results tell us that for each reaction period, there is an limiting $CuInSe_2$ thickness for which CuIn bilayer selenization is complete hence higher device performance. The most interesting result is the 7.41 % efficiency for reaction period of 15 minutes and temperature of 350 °C. This gives us hope as decreasing the temperature, reaction period and $CuInSe_2$ thickness is the challenge for further $CuInSe_2$ research. The decrease in cell efficiency for $CuInSe_2$ layer less than

1.4 μm thick reacted for 60 and 90 minutes might be due to absorption of light not taking place properly either due to $CuInSe_2$ absorber layer being too thin or $CuInSe_2$ thin film properties changing unfavorable as regards to light absorption. Results for less reaction periods (15 and 30 minutes) are, however, contrary, leading us to believe that less reaction periods tends to arrest this problem. Attempts to calculate absorption coefficients for our absorber layer in order to provide information on the above results were unsuccessful as explained in section 4.3.4.

With respect to film composition, the efficiency is generally higher for $CuInSe_2$ films which are slightly In rich. This consistent with data from other workers [Rocheleau et. al., 1987].

Table 4.1. Appearance and resistivity of DC sputtered In films for different thicknesses. Base pressure, power and sputtering pressure were maintained constant at 3.0 x 10^{-6} mbar, 100 W and 5.8 × 10^{-3} mbar, respectively.

Thickness (nm)	Appearance	Resistivity (Ωm)
33	Light brown	1.400×10^2
65	Silvery	1.050×10^2
85	Light blue	2.351×10^0
117	Gray	4.771×10^{-3}
169	White	4.695×10^{-7}
221	White	3.120×10^{-7}
429	White	2.520×10^{-7}

Table 4.2. Relative Cu and In thicknesses and corresponding average CuIn thickness after selenization.

Cu (μm)	In (μm)	Selenized CuIn (μm)
0.2500	0.6906	2.2
0.1250	0.3453	1.4
0.0938	0.2591	0.8
0.0625	0.1727	0.6

Table 4.3. XRD data with reaction period for different precursor thicknesses.
Reaction temperature was 350 °C.

Precursor thickness	Reaction period (Min.)	Phases
(Cu : 0.2500 μm; In : 0.6906 μm)	15	$CuInSe_2$, InSe 1 unidentified peak [++]
	30	$CuInSe_2$, InSe 1 unidentified peak[++]
	60	$CuInSe_2$, InSe
	90	$CuInSe_2$, InSe
(Cu : 0.1250 μm; In : 0.3453 μm)	15	$CuInSe_2$, InSe
	30	$CuInSe_2$
	60	$CuInSe_2$
	90	$CuInSe_2$
(Cu : 0.0938 μm; In : 0.2591 μm)	15	$CuInSe_2$, InSe
	30	$CuInSe_2$
	60	$CuInSe_2$
	90	$CuInSe_2$
(Cu : 0.0625 μm; In : 0.1727 μm)	15	$CuInSe_2$
	30	$CuInSe_2$
	60	$CuInSe_2$
	90	$CuInSe_2$

[+] d=1.86
[++] d=3.03

Table 4.4. XRD data with precursors thickness. Reaction period and temperature
were 15 minutes and 350 °C, respectively.

Precursor thickness	Phases
(Cu : 0.2500 μm; In : 0.6906 μm)	$CuInSe_2$, InSe 1 unidentified peak [++]
(Cu : 0.1250 μm; In : 0.3453 μm)	$CuInSe_2$, InSe
(Cu : 0.0938 μm; In : 0.2591 μm)	$CuInSe_2$, InSe
Cu : 0.0625 μm; In : 0.1727 μm)	$CuInSe_2$

[+] d=1.86
[++] d=3.03

Table 4.5 . Composition data for CuIn precursor of different thicknesses selenized at reaction temperature of 350 °C. Intended Cu/In ratio for all thickness is 0.8. CuInSe$_2$ film thickness is given.

Precursor thickness	Reaction period (min.)	CuInSe$_2$ thickness (µm)	% Cu	% In	% Se	Cu/In
(Cu : 0.2500 µm; In : 0.6906 µm)	15	2.2	25.6	25.7	48.8	1.00
	30		26.2	24.4	49.4	1.07
	60		25.4	24.2	50.4	1.05
	90		26.6	24.2	49.3	1.09
(Cu : 0.1250 µm; In : 0.3453 µm)	15	1.4	23.8	25.4	50.8	0.94
	30		23.9	25.1	51.0	0.95
	60		23.0	25.1	51.9	0.92
	90		23.6	25.2	51.2	0.94
(Cu : 0.0938 µm; In : 0.2591 µm)	15	0.8	21.7	25.0	53.3	0.87
	30		21.6	25.1	53.3	0.86
	60		21.9	26.2	52.0	0.84
	90		21.4	26.1	52.5	0.82
(Cu = 0.0625 µm; In : 0.1727 µm)	15	0.6	18.8	24.4	56.9	0.77
	30		19.4	24.6	56.1	0.79
	60		18.5	23.8	57.7	0.78
	90		18.5	24.2	57.3	0.76

Table 4.6. EDS data for heat treated CuIn bilayers of different thicknesses. Intended Cu/In ratio was 0.8. Heat treatment was done in Ar gas at 200 °C for 30 minutes.

Precursor thickness	Cu (at. %)	In (at. %)	Cu/In Ratio
(Cu : 0.2500 µm; In : 0.6906 µm)	44.40	55.60	0.80
(Cu : 0.1250 µm; In : 0.3453 µm)	43.13	56.87	0.76
(Cu : 0.625 µm; In : 0.1727 µm)	44.33	55.67	0.80

Table 4.7. XRD data with reaction period for different reaction temperatures. Precursor thickness is (Cu : 0.1250 μm; In : 0.3453 μm).

Reaction temperature (°C)	Reaction period (Min.)	Phases
350	15	$CuInSe_2$, InSe
	30	$CuInSe_2$
	60	$CuInSe_2$
	90	$CuInSe_2$
400	15	$CuInSe_2$, InSe
	30	$CuInSe_2$
	45	$CuInSe_2$, 2 unidentified peaks[+, ++]
	60	$CuInSe_2$, 2 unidentified peaks[+, ++]
450	15	$CuInSe_2$
	30	$CuInSe_2$
	45	$CuInSe_2$
	60	$CuInSe_2$, 2 unidentified peaks[+, ++]
500	15	$CuInSe_2$, $MoSe_2$, 2 unidentified peaks[+, ++]
	45	$CuInSe_2$, $MoSe_2$
	50	$CuInSe_2$, $MoSe_2$
	60	$CuInSe_2$, $MoSe_2$

[+] d=1.86
[++] d=3.03

Table 4.8. Cu/In ratio data for selenized CuIn precursors at different reaction temperatures. Precursor thickness is (Cu : 0.2500 μm; In : 0.6906 μm).

Reaction temperature (°C)	Cu/In Ratio	
	Reaction period = 15 min.	Reaction period = 60 min.
350	1.00	1.05
400	1.08	1.05
450	1.01	1.05
500	?	?

? = Films not uniform and cracked hence EDS results not good.

Table 4.9. Summary of solar cell parameters: Absorber (CuInSe$_2$) preparation conditions and thicknesses are given.

Reaction temp. (°C)	Reaction period (min.)	Absorber[*] thickness (μm)	V_{oc}	J_{sc}	FF	η
350	15	2.2	0.002	0.38	24.8	0.00
		1.4	0.0048	9.54	25.0	0.01
		0.8	0.2117	22.82	30.3	1.46
		0.6	0.4337	26.42	64.7	7.41
	30	2.2	0.0016	1.53	24.7	0.00
		1.4	0.3793	29.67	51.3	5.77
		0.8	0.3846	29.72	60.0	6.86
		0.6	0.4192	27.47	60.8	7.00
	60	2.2	0.0012	0.95	24.8	0.00
		1.4	0.4664	30.98	67.8	9.79
		0.8	0.4592	29.20	65.5	8.78
		0.6	0.4142	26.88	57.6	6.41
	90	2.2	0.2436	24.41	38.3	2.28
		1.4	0.4902	31.27	69.0	10.58
		0.8	0.4575	29.38	64.3	8.65
		0.6	0.4585	26.84	63.8	7.85
400	15	2.2	0.0046	3.29	25.0	0
		1.4	0.3190	29.64	33.9	3.20
	30	2.2	0.2676	30.35	40.1	3.25
		1.4	0.4248	31.86	62.2	8.42
	45	2.2	0.4570	33.37	61.7	9.40
		1.4	0.4551	31.55	66.2	9.51
	60	2.2	0.4594	33.14	63.1	9.60
		1.4	0.4681	32.31	69.3	10.49
450	15	2.2	0.0002	0.45	25.0	0
		1.4	0.3609	34.12	54.4	6.70
	30	2.2	0.3234	37.20	52.0	6.26
		1.4	0.3749	33.81	58.6	7.43
	45	2.2	0.3229	36.88	51.4	6.12
		1.4	0.3777	34.96	59.5	7.86
	60	2.2	0.3335	36.71	55.2	6.76
		1.4	0.3653	34.51	57.5	7.25
500	15	2.2	0.3330	26.30	43.9	3.84
		1.4	0.3250	21.62	44.9	3.16
	45	2.2	0.3107	20.42	46.5	2.95
		1.4	0.3199	16.12	43.1	2.22
	50	2.2	0.3304	28.20	42.2	3.93
		1.4	0.3031	19.30	42.2	2.47
	60	2.2	0.3535	28.53	47.5	4.79
		1.4	0.3092	20.08	47.7	2.96

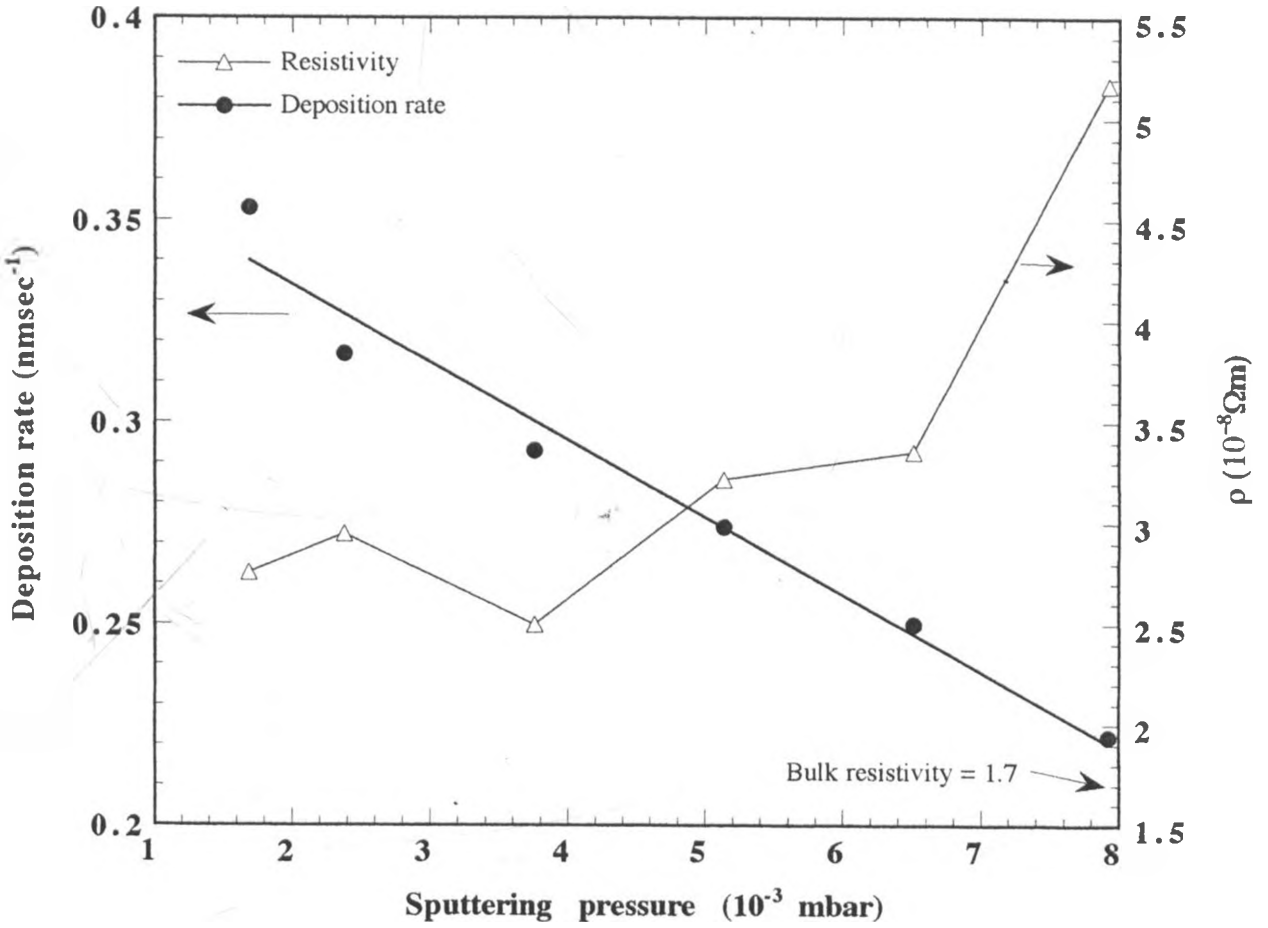[*] Relative Cu and In thicknesses before selenization are given in Table 4.2.

Figure. 4.1. Variation of resistivity and deposition rate with sputtering pressure for a 34 nm thick Cu film. Base pressure and power were maintained at 3.0×10^{-6} mbar and 190 W, respectively.
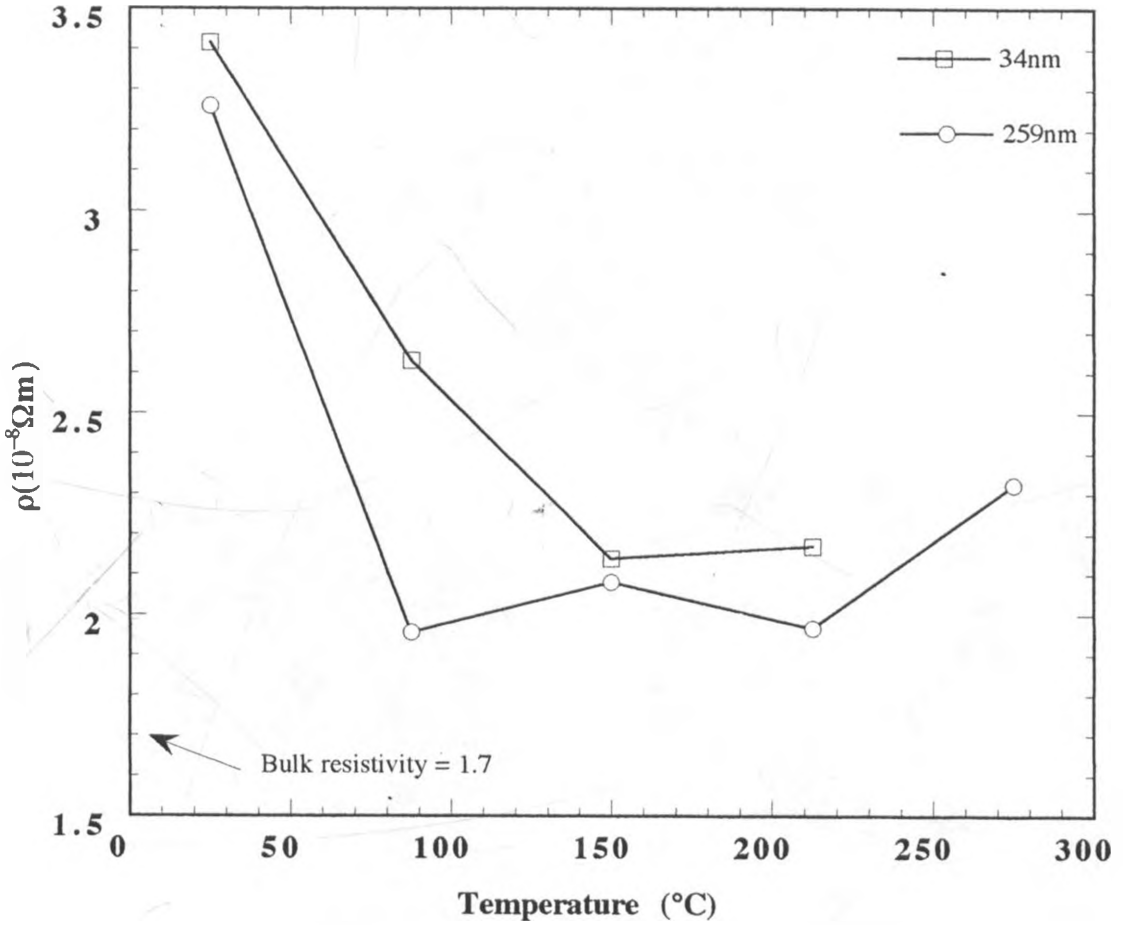
Figure 4.2. Variation of resistivity with deposition temperature for 34 and 259 nm thick Cu films. Base pressure, sputtering pressure and magnetron power were maintained at 3.0×10^{-6} mbar, 2.4×10^{-3} mbar, and 190 W, respectively.
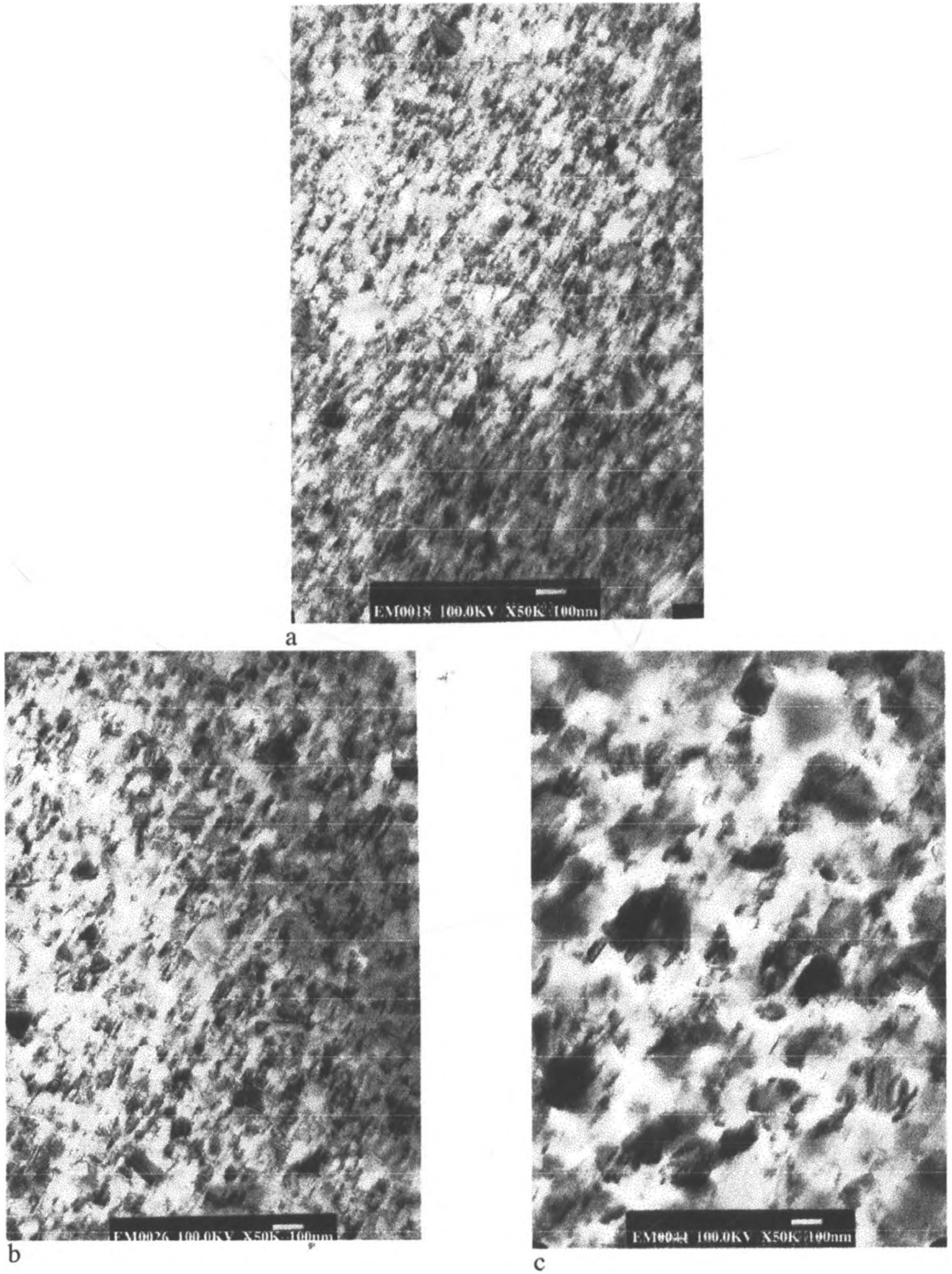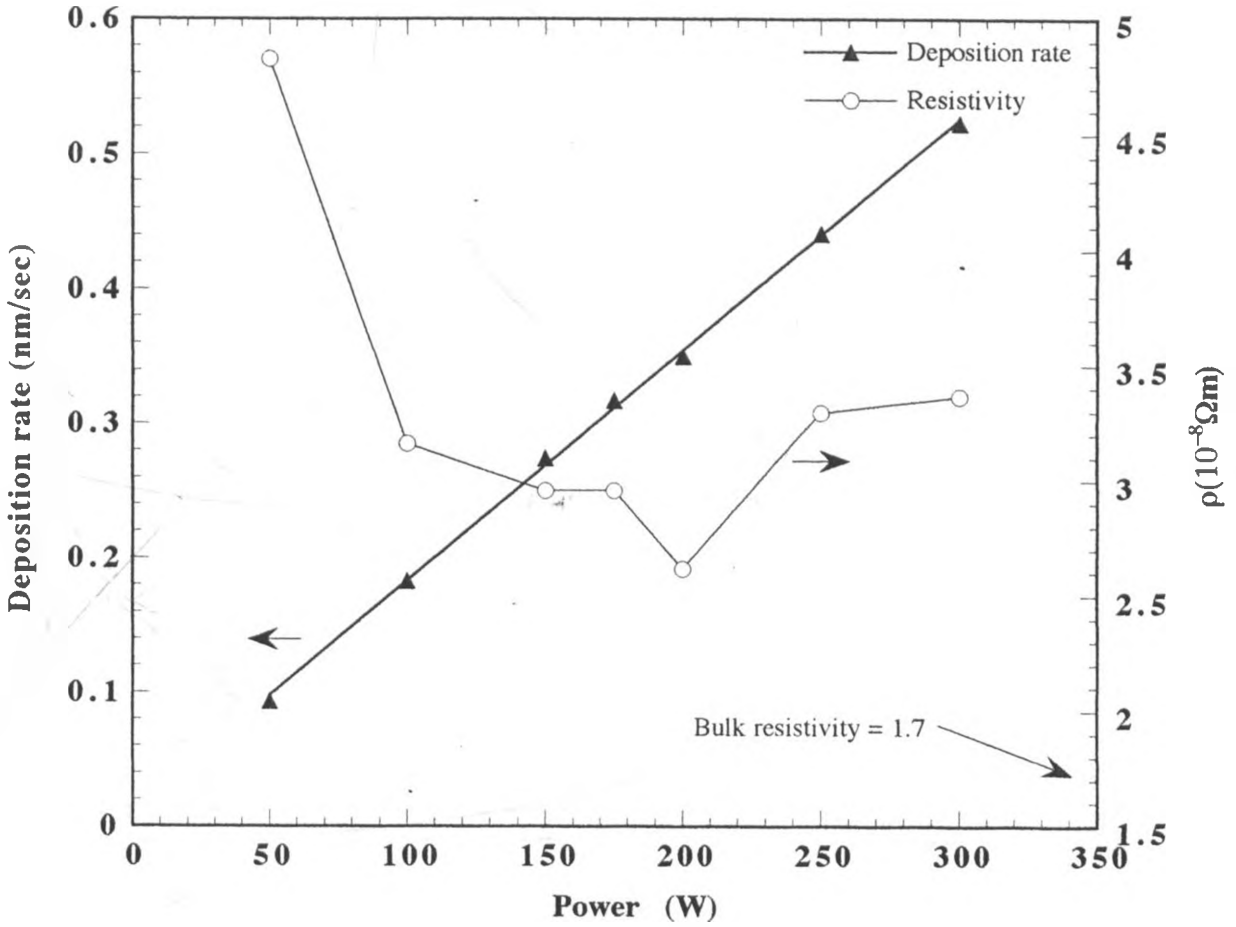
Figure 4.3. TEM micrographs for 34 nm Cu films deposited at (a) 25°C (b) 150°C (c) 275°C. Base pressure, sputtering pressure, and magnetron power were maintained at 3.0×10^{-6} mbar, 2.4×10^{-3} mbar, and 190 W, respectively.

Figure 4.4. Variation of resistivity and deposition rate with magnetron power for 34 nm Cu film. Base pressure and sputtering pressure were maintained at 3.0×10^{-6} mbar and 2.4×10^{-3} mbar, respectively.
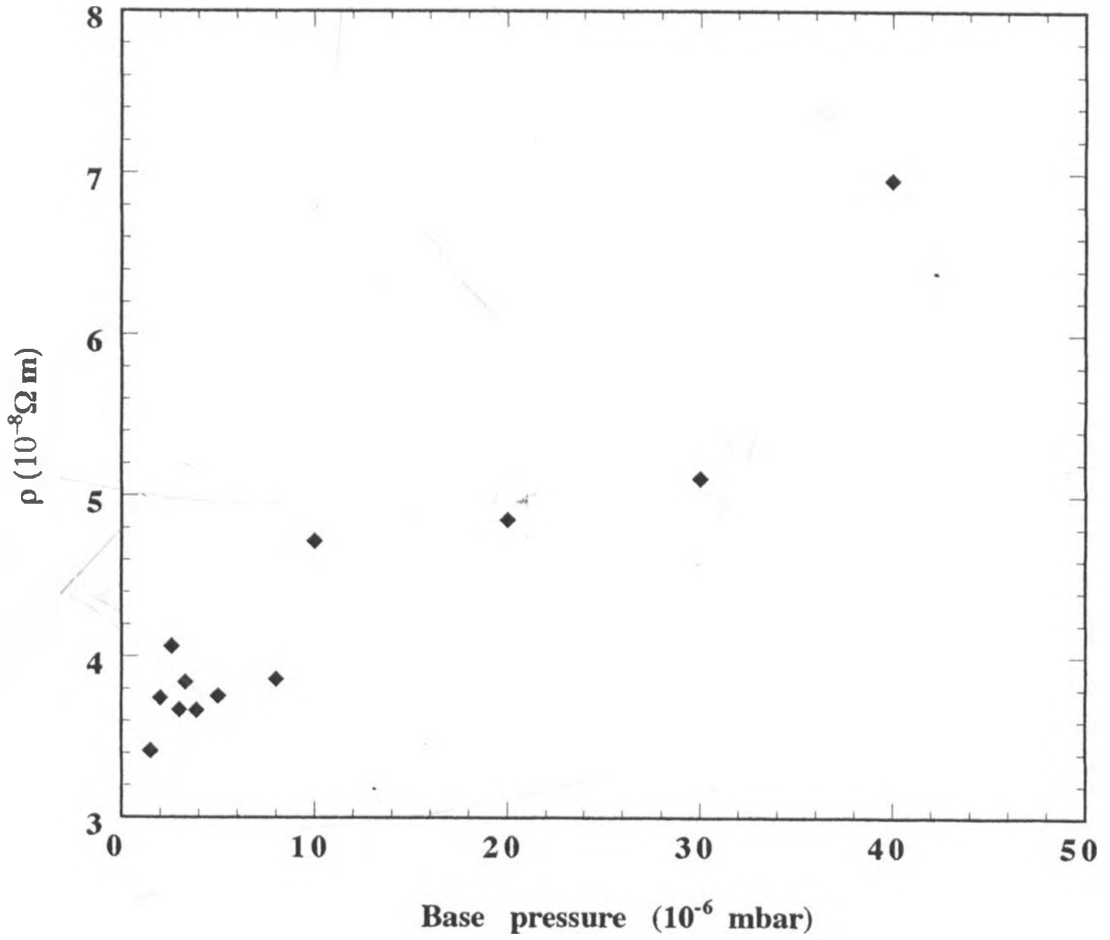
Figure 4.5. Variation of resistivity with base pressure for a 34 nm Cu film. Base pressure, sputtering pressure, and magnetron power were maintained at 3.0×10^{-6} mbar, 2.4×10^{-3} mbar, and 190 W, respectively.
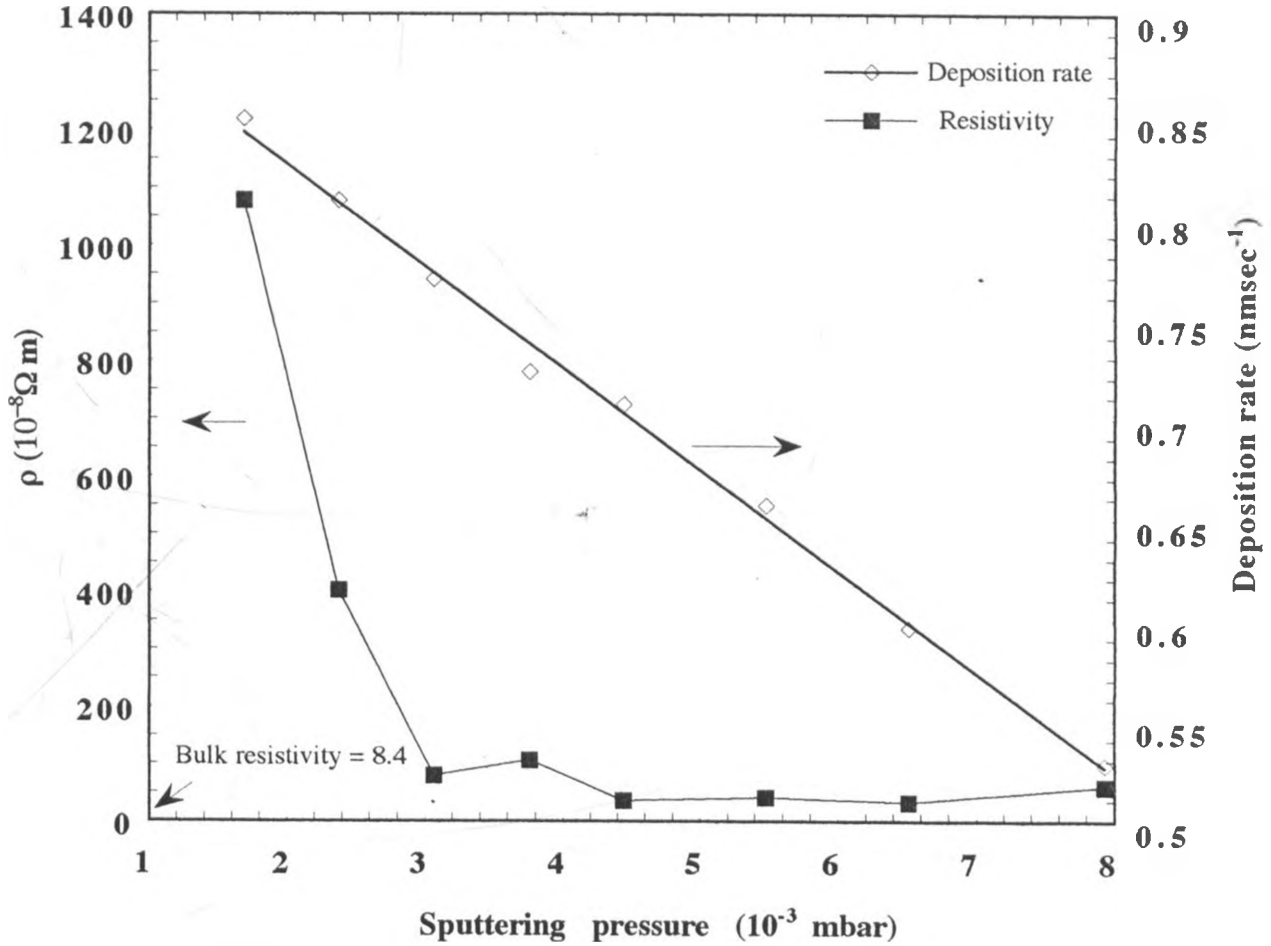
Figure 4.6. Variation of resistivity and deposition rate with sputtering pressure for DC sputtered In films. Base pressure, power and thickness were maintained at 3.0×10^{-6} mbar, 100 W and 221 nm, respectively.
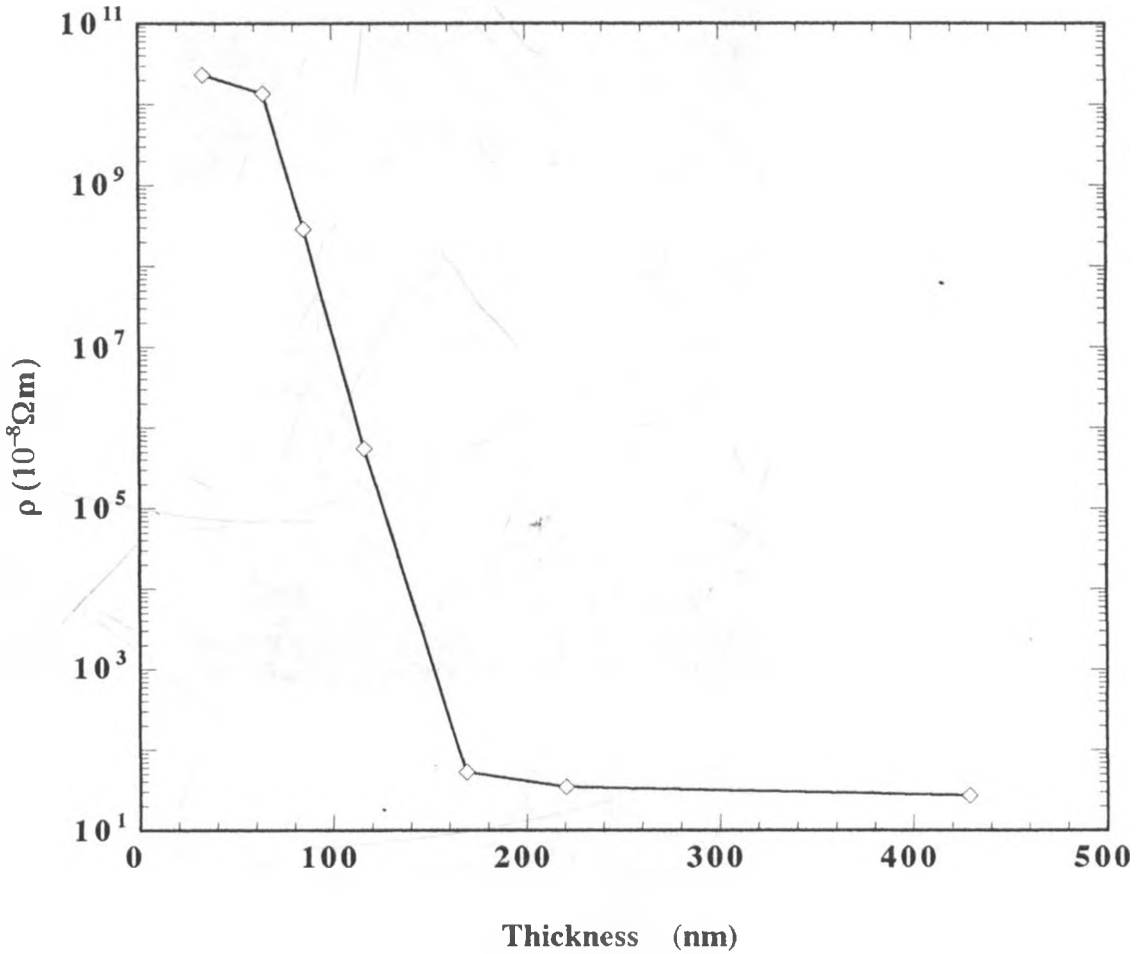
Figure 4.7. Variation of resistivity with thickness for DC sputtered In films. Base pressure, power and sputtering pressure were maintained constant at 3.0×10^{-6} mbar, 100 W, and 5.8×10^{-3} mbar, respectively.
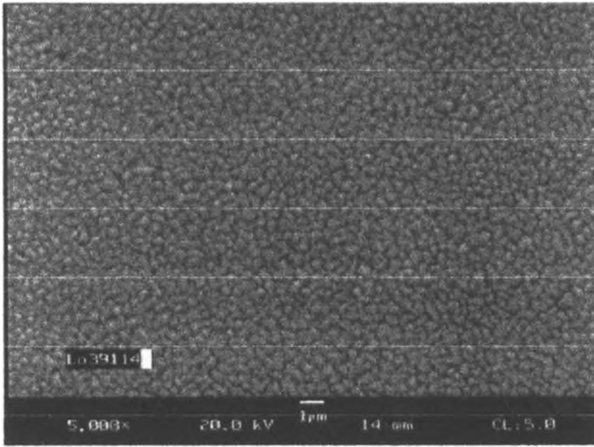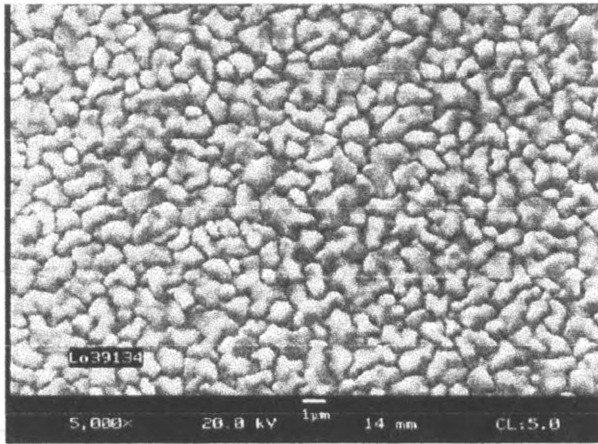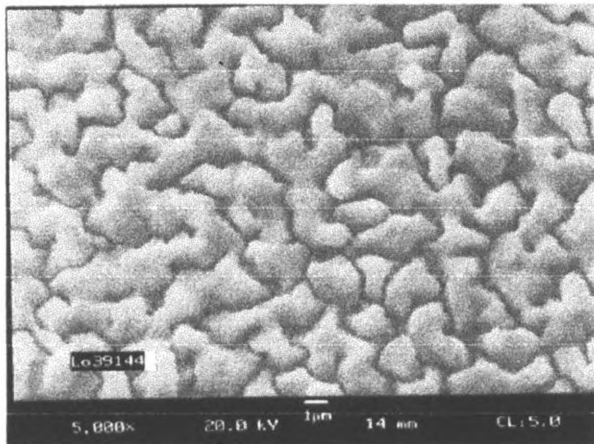
Figure 4.8. SEM pictures for In films of different thicknesses (a) 33 (b) 117
(c) 429 nm. Base pressure, power and sputtering pressure were 3.0×10^{-6} mbar, 100
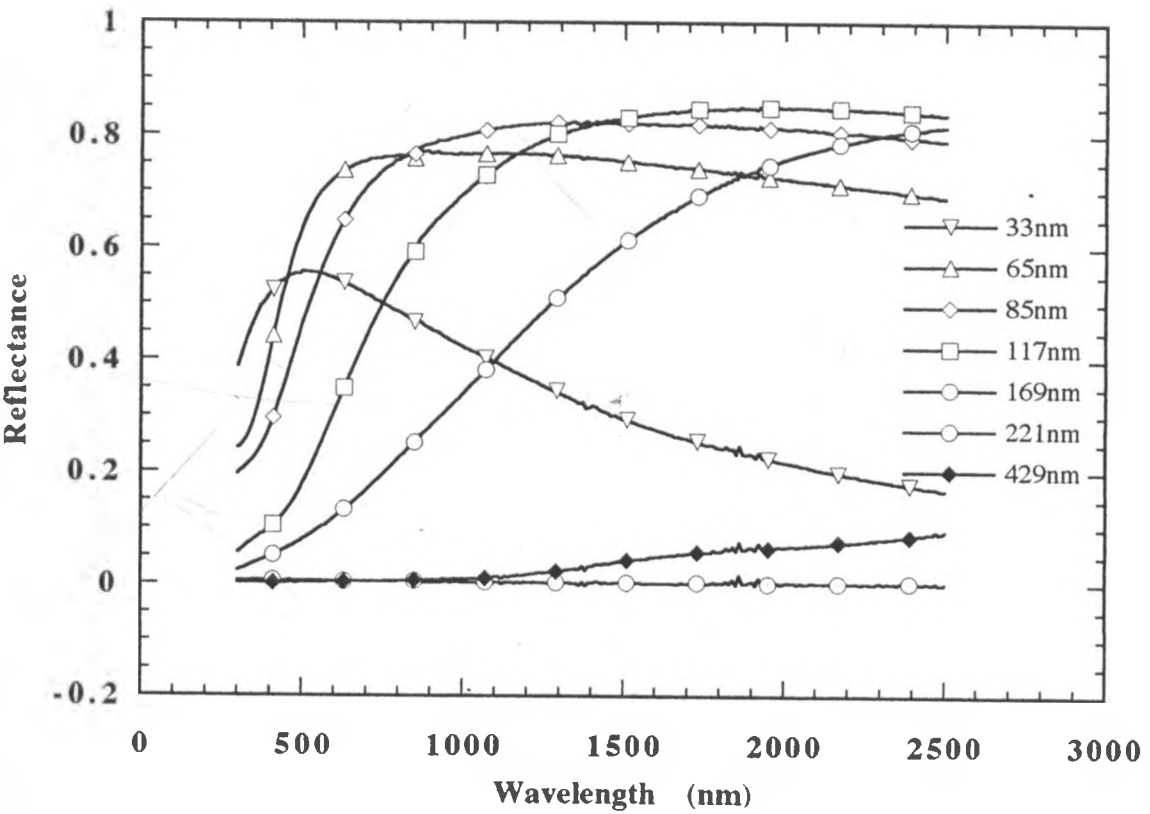W, and 5.8×10^{-3} mbar, respectively.

Figure 4.9. Reflectance data for DC sputtered In films. Base pressure, power, sputtering pressure and thickness were 3.0×10^{-6} mbar, 100 W, 5.8×10^{-3} mbar, and 33 to 429 nm, respectively.
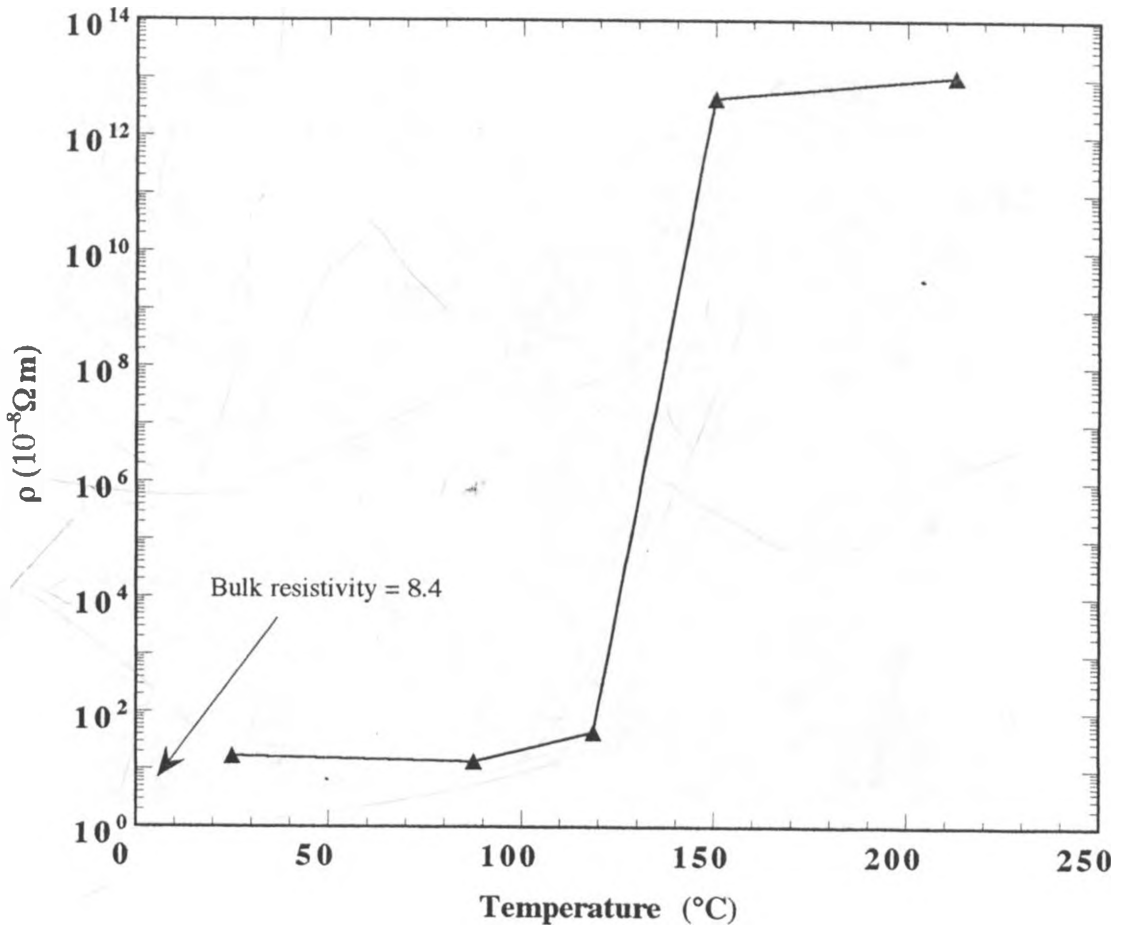
Figure 4.10. Variation of resistivity with deposition temperature for DC sputtered In films. Base pressure, sputtering pressure, thickness, and magnetron power were maintained at 3.0×10^{-6} mbar, 5.8×10^{-3} mbar, 221 nm, and 200 W, respectively.
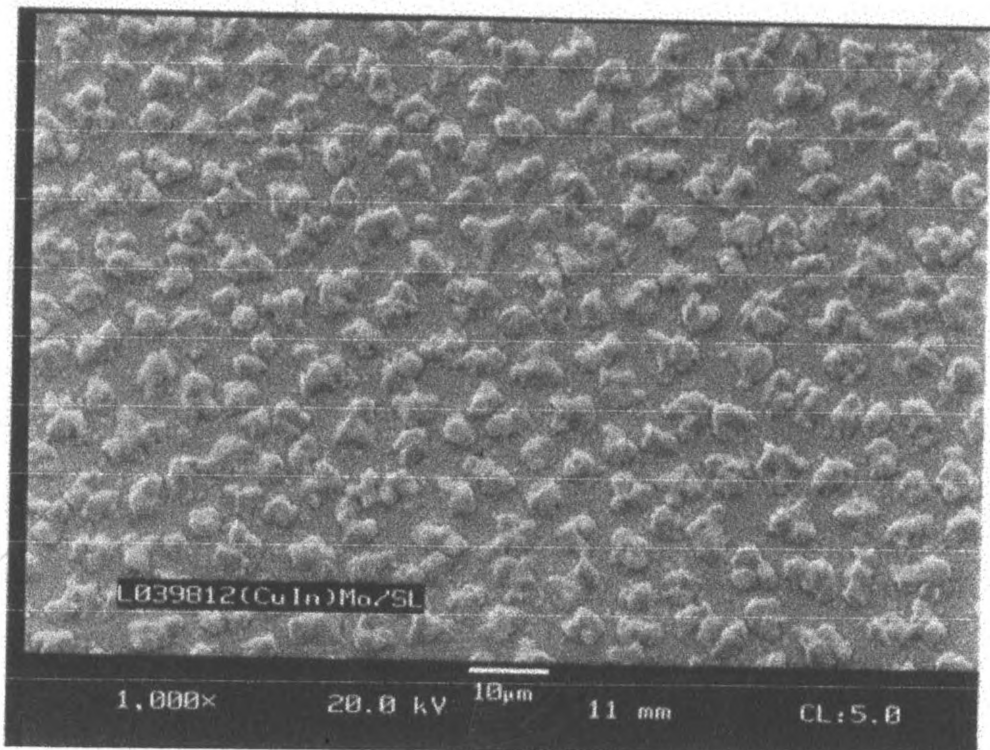
Figure 4.11. Typical SEM picture for a CuIn bilayer on Mo coated soda lime glass.

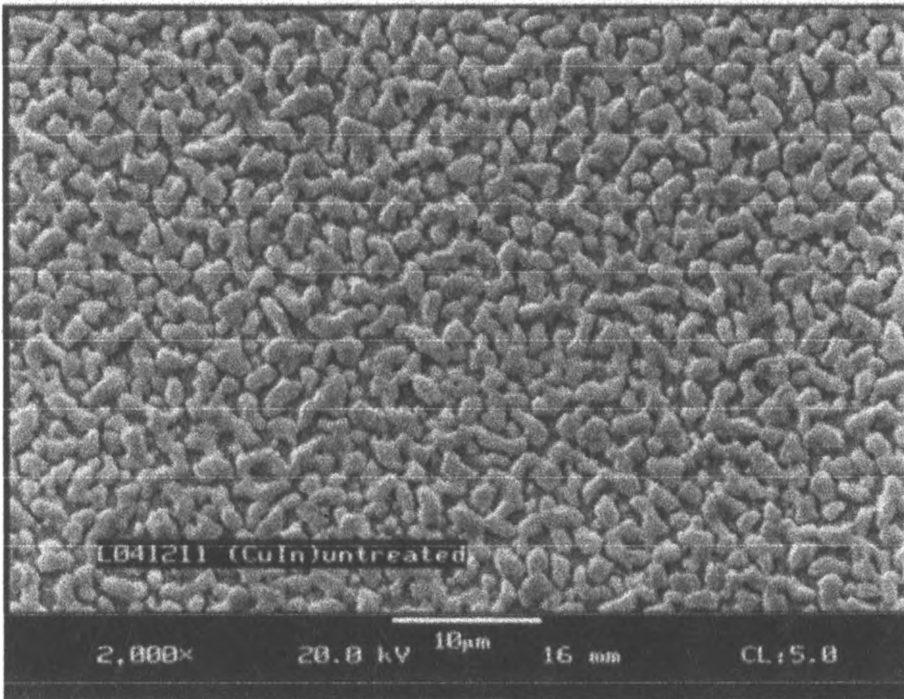Figure 4.12. SEM picture for a CuIn bilayer. Cu and In deposition rates were 4.8 and 15.8 Ås^{-1}, respectively.
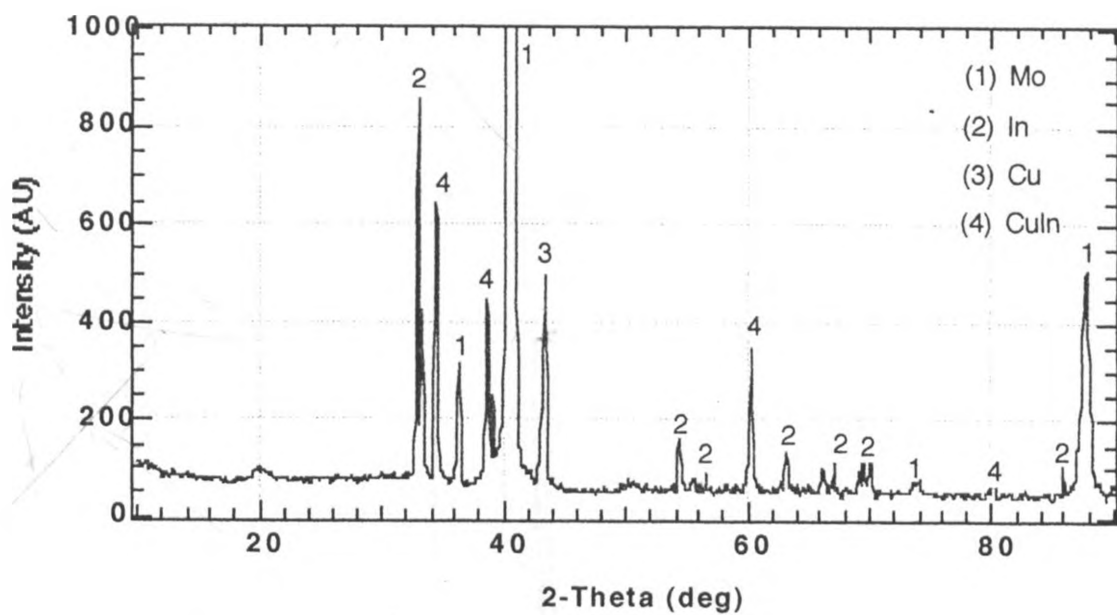
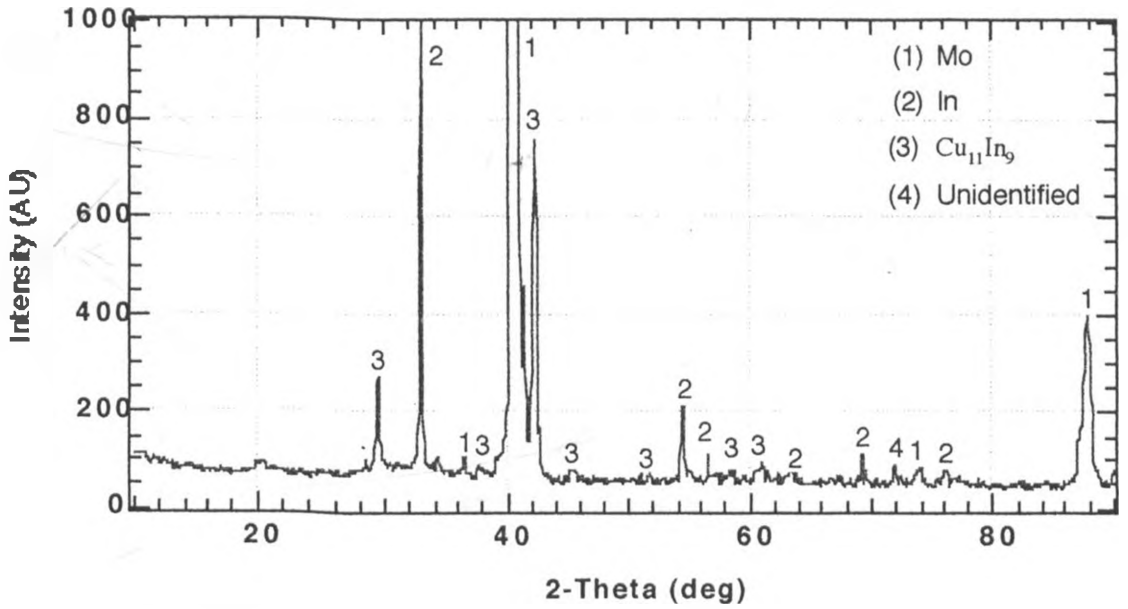Figure 4.13. XRD trace for as grown CuIn bilayer on Mo coated soda lime glass.

Figure 4.14. XRD trace for heat treated CuIn bilayer on Mo coated soda lime glass. d = 1.31 for unidentified phase.
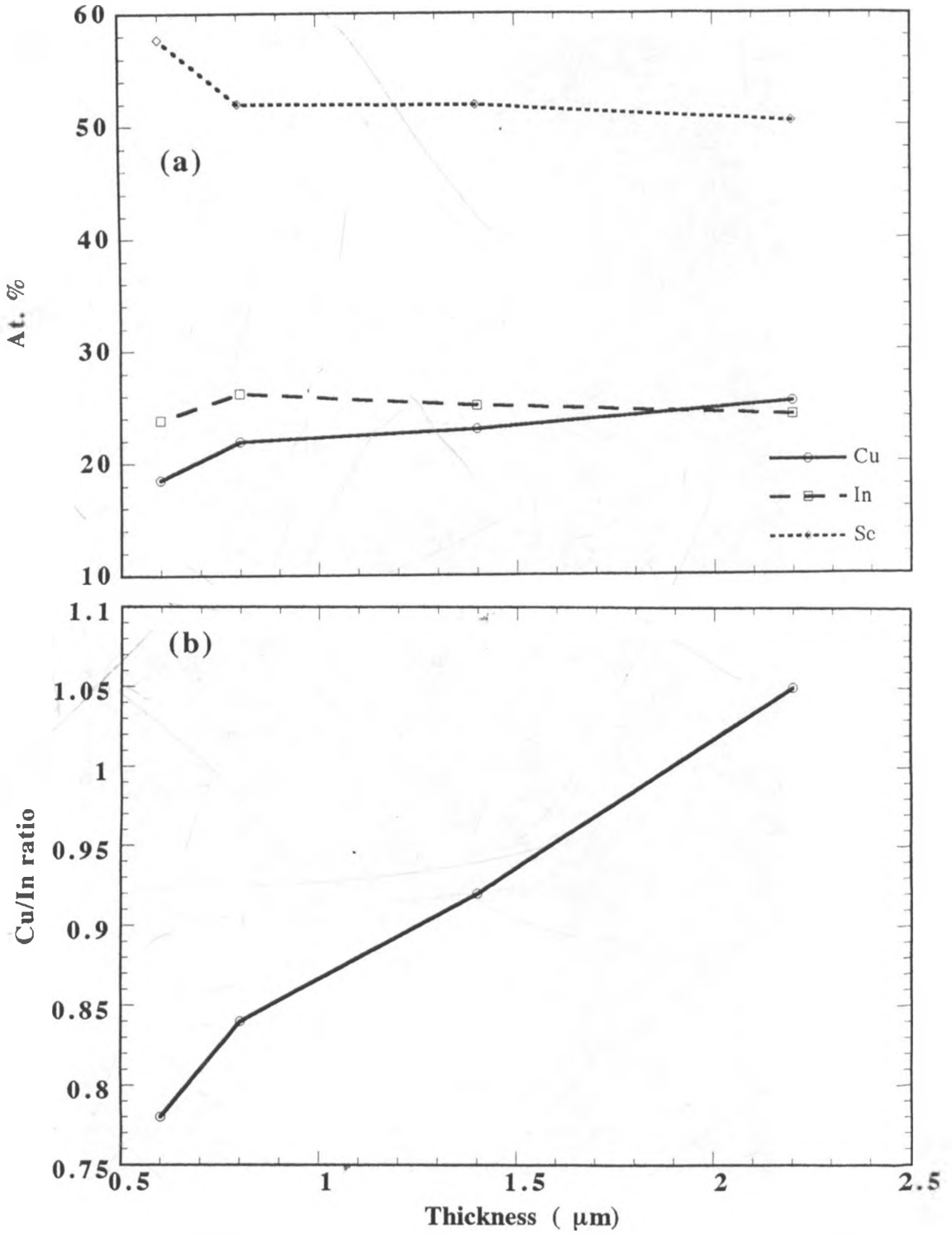
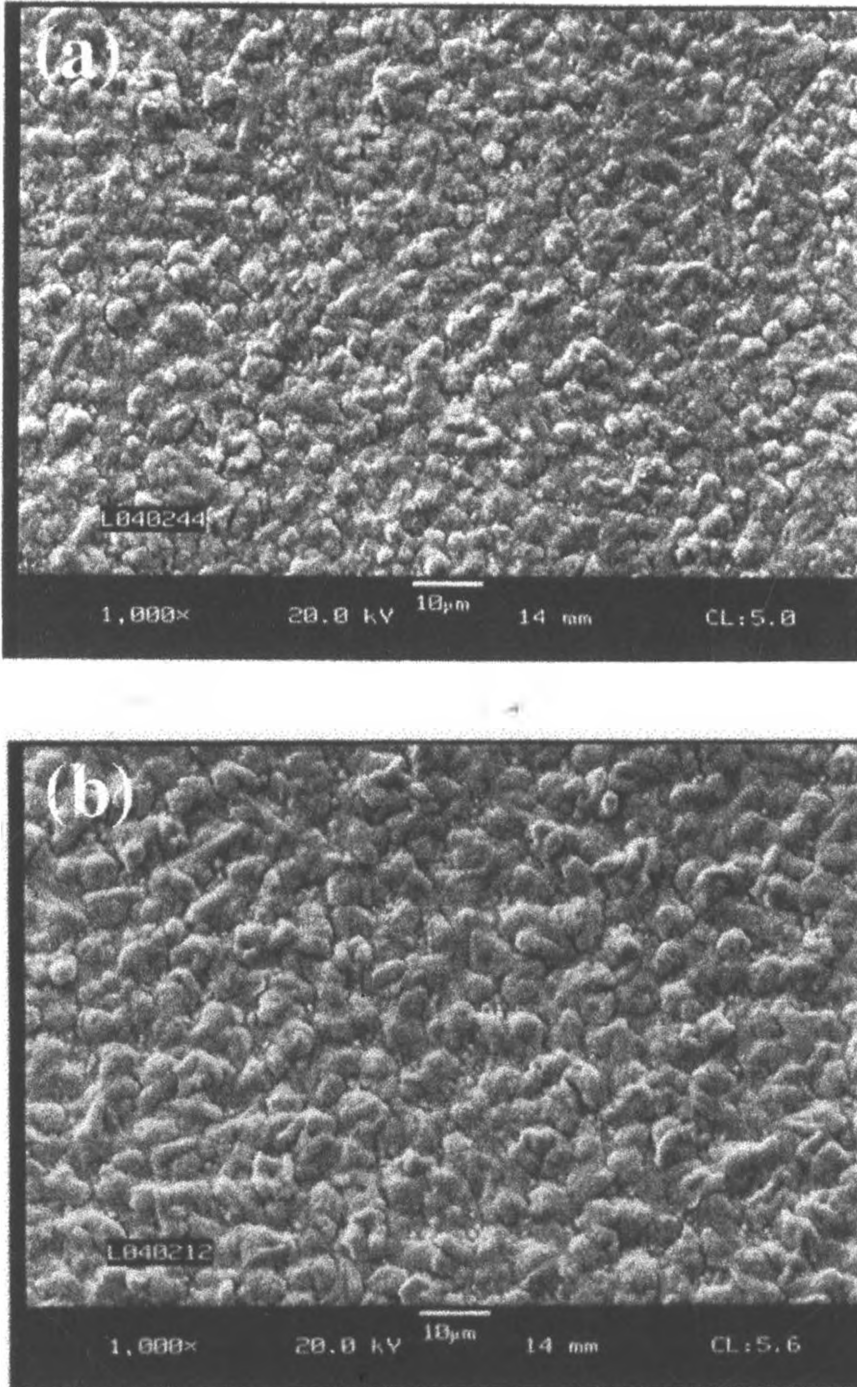Figure 4.15. Variation of (a) Cu, In and Se at. % (b) Cu/In ratio with absorber thickness.

Figure 4.16. SEM micrographs for fully reacted (a) and partially reacted(b) precursors. Reaction temperature was 350 °C.

(a) Precursor thickness and reaction period were (Cu : 0.1250 μm; In : 0.3453 μm) and 90 minutes, respectively.

(b) Precursor thickness and reaction period were (Cu : 0.2500 μm; In : 0.6906 μm) and 15 minutes, respectively.

(a)

(b)
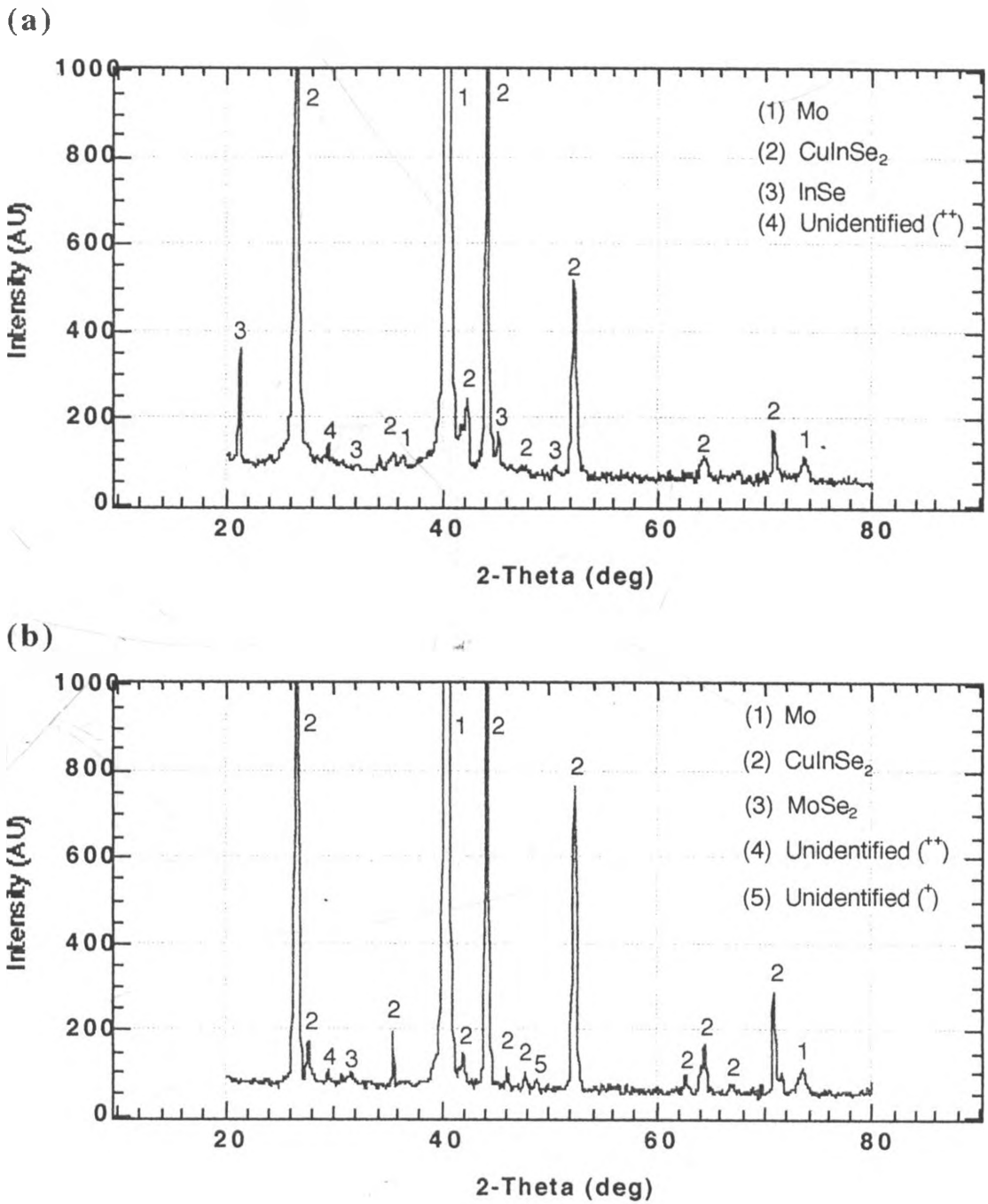
Figure 4.17. Typical XRD traces for selenized CuIn bilayer:

(a) Reaction temperature, reaction period and $CuInSe_2$ thickness were 350 °C, 30 minutes and 2.2 μm, respectively.

(b) Reaction temperature, reaction period and $CuInSe_2$ thickness were 500 °C, 45 minutes and 2.2 μm, respectively.
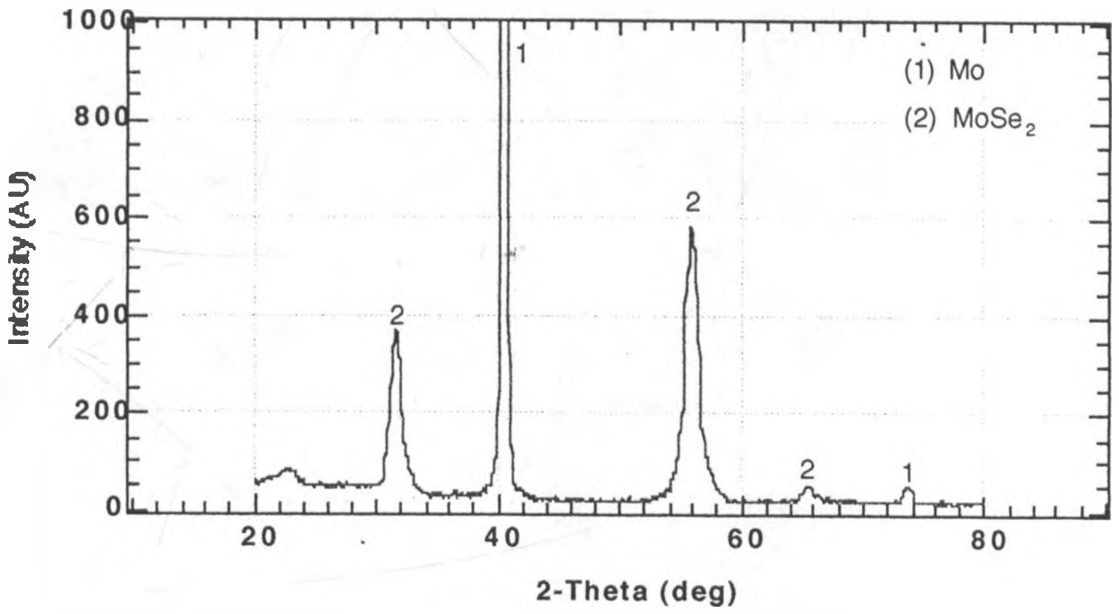
Figure. 4.18. XRD trace for Mo coated 7059 glass selenized for 90 minutes at 550 °C [Marudachalam, 1998].
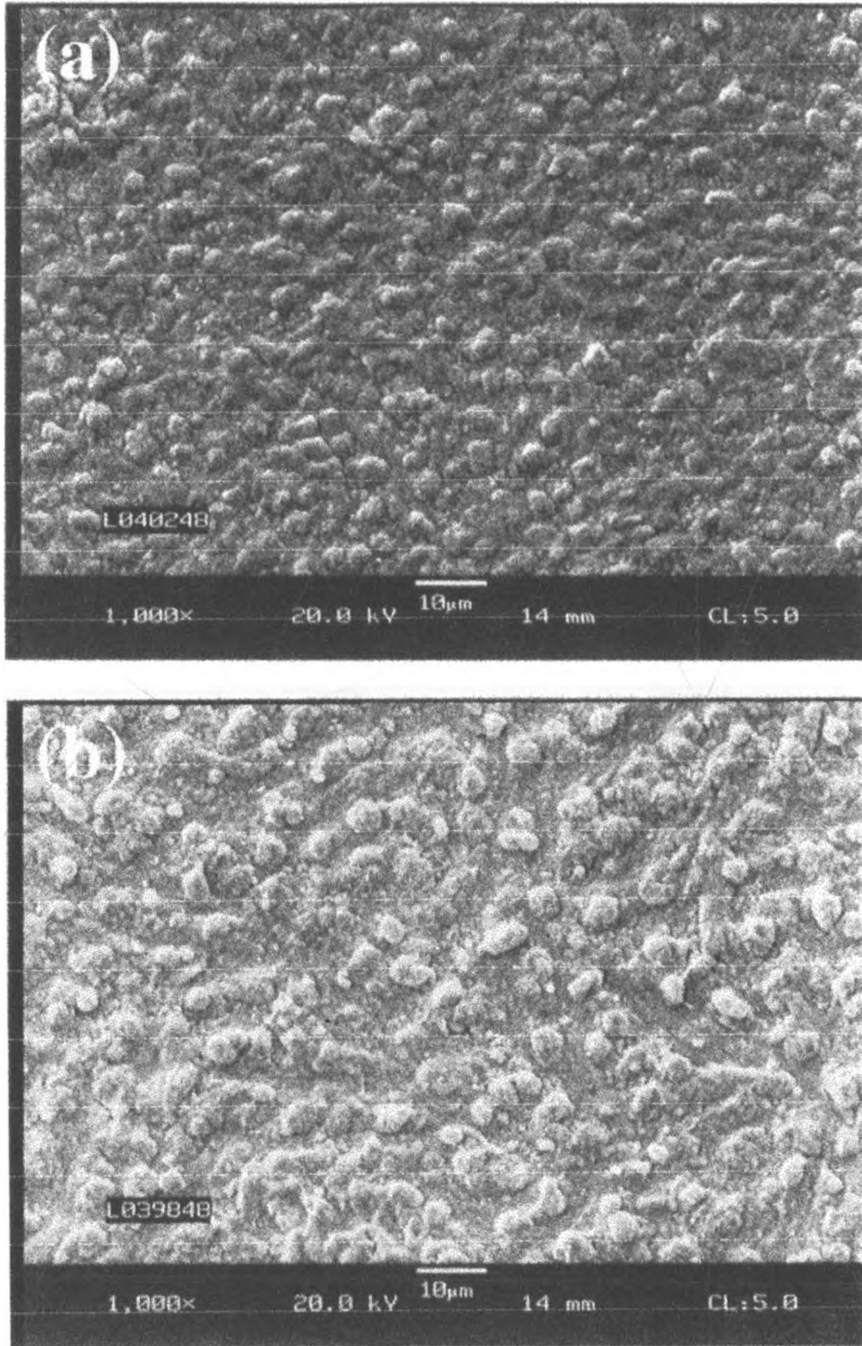
Figure 4.19 (continued next page)
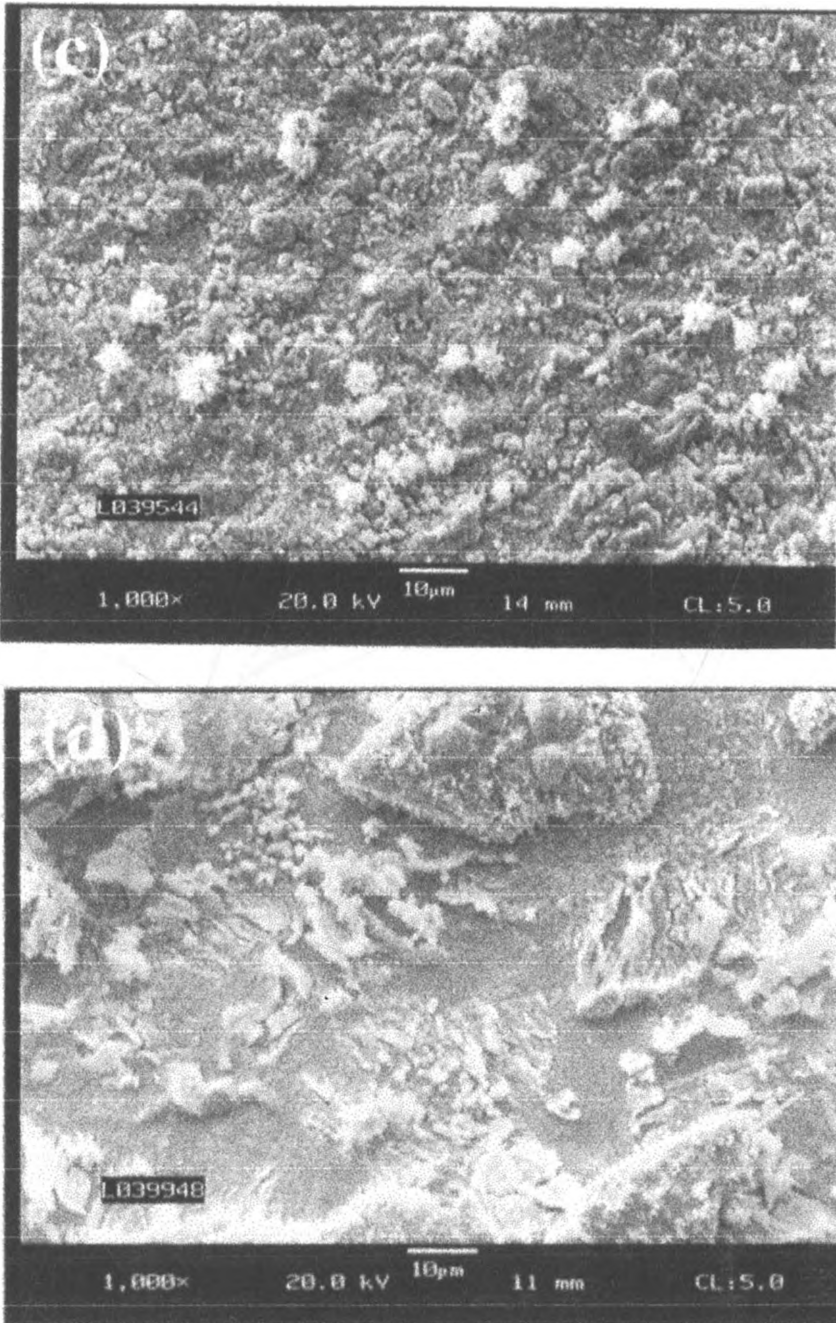
Figure 4.19 SEM pictures for CuInSe$_2$ films prepared at different reaction temperatures. Precursor thickness and reaction period were (Cu : 0.1250 μm; In : 0.3453 μm) and 60 minutes, respectively.

(a) 350 °C (b) 400 °C (c) 450 °C (d) 500 °C.
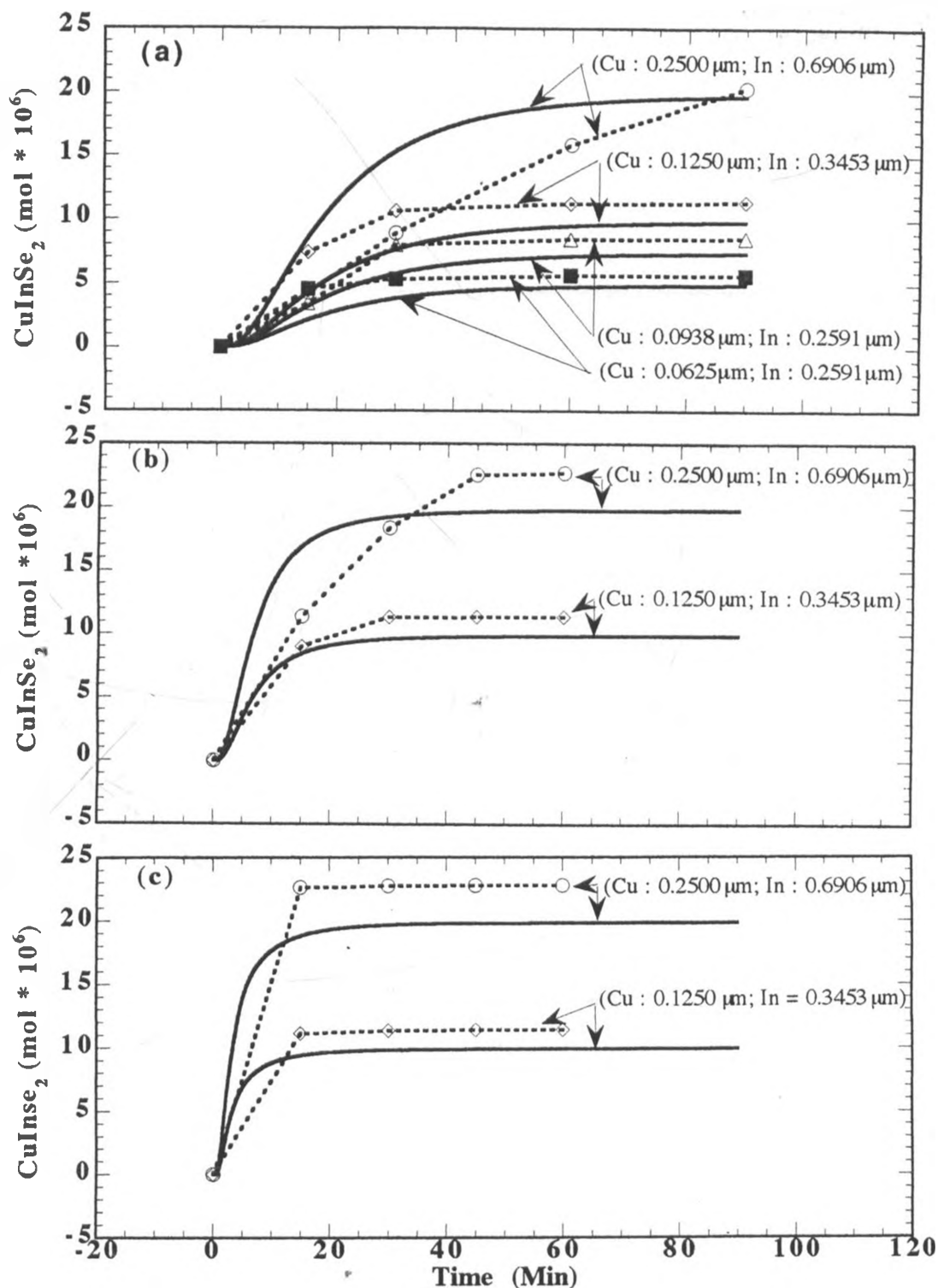
Figure 4.20. Predicted(solid lines) and experimental (dashed lines) number of moles versus reaction period for CuInSe$_2$ films obtained using different precursor thicknesses. Reaction temperature were: (a) 350 °C. (b) 400 °C. (c) 450 °C.
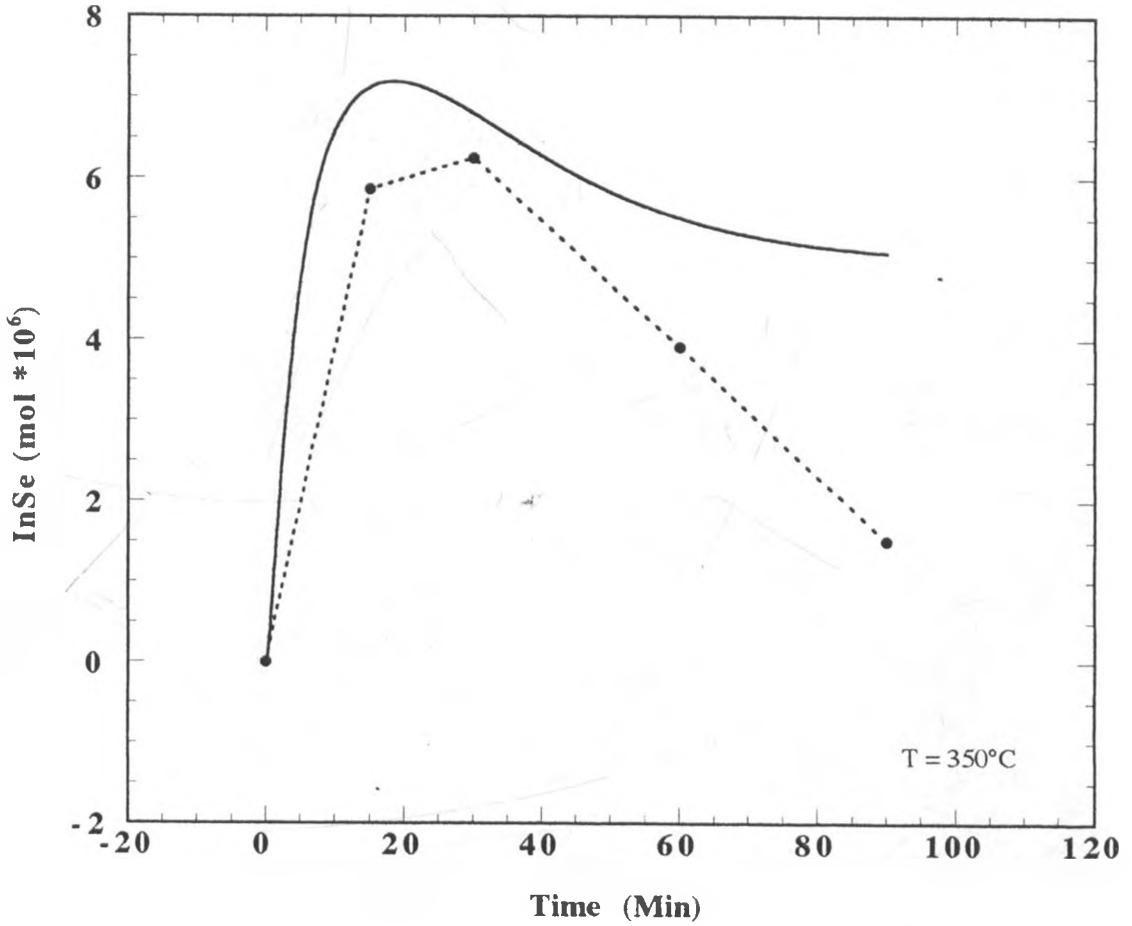
Figure 4.21. Predicted (solid lines) and experimental (dashed lines) number of moles of InSe versus reaction period for 2.2 μm CuInSe$_2$ films. Reaction temperature was 350 °C.
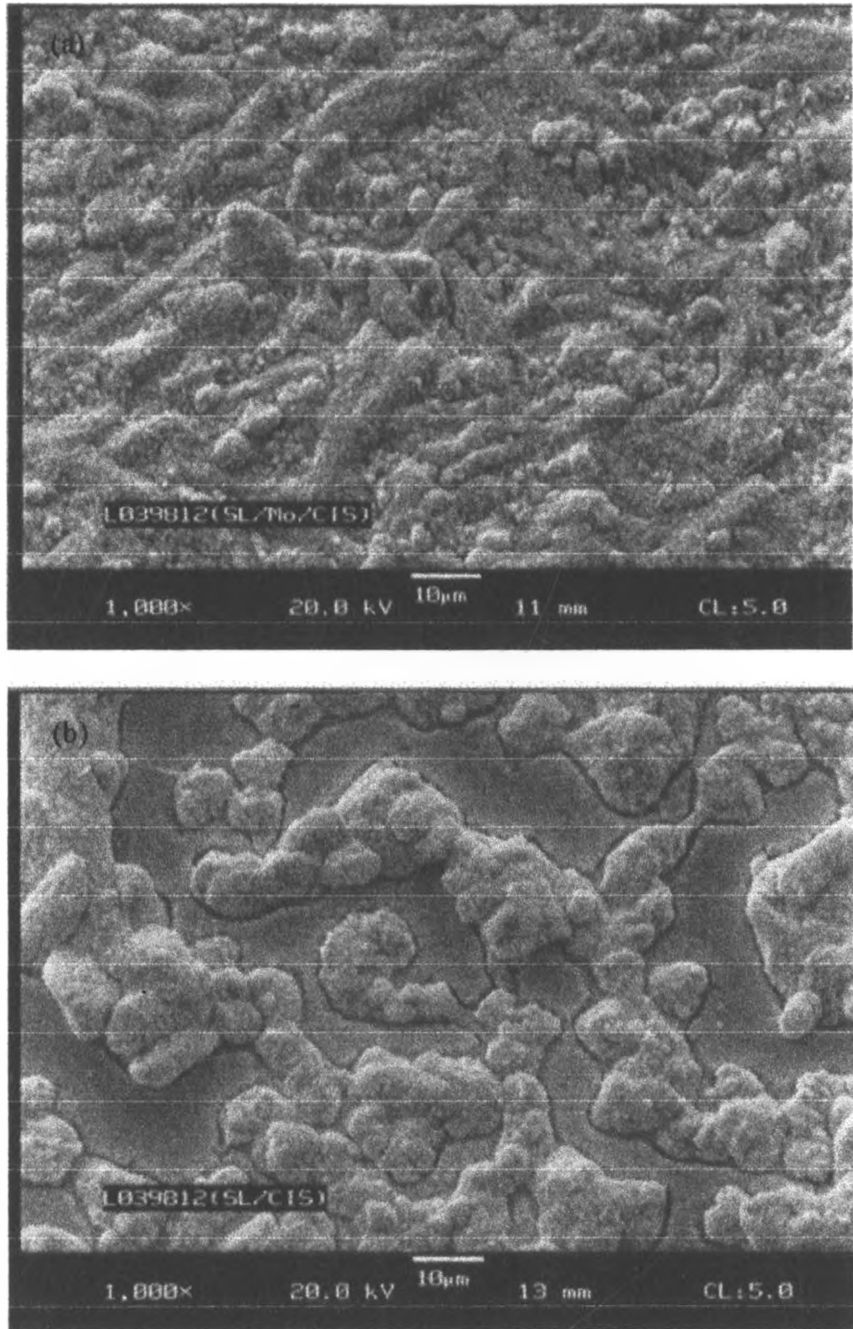
Figure 4.22. Typical CuInSe$_2$ morphologies:
(a) On Mo coated soda lime glass   (b) On uncoated soda lime glass
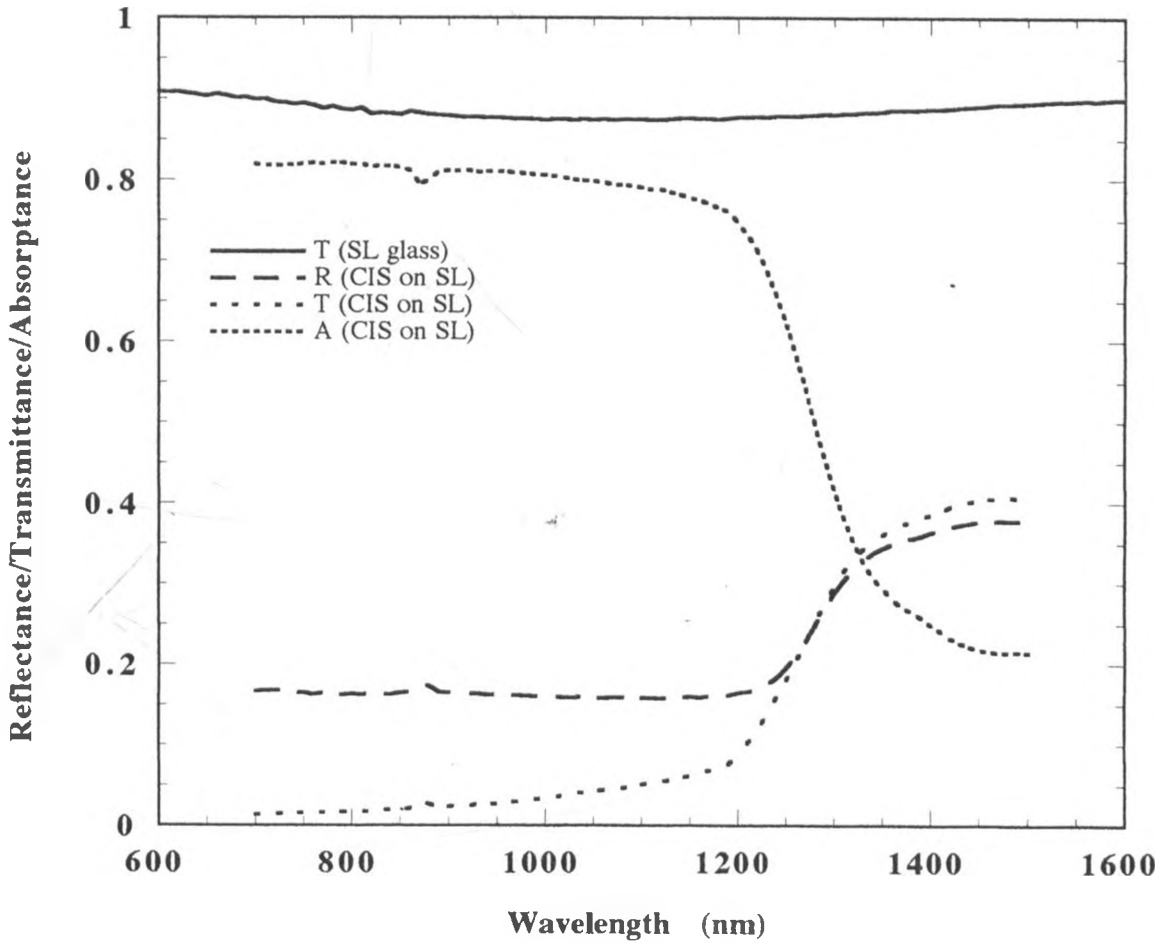
Figure 4.23. Total transmittance/reflectance/absorptance with wavelength for CuInse₂ films on soda lime glass. Transmittance for bare soda lime glass is also given.
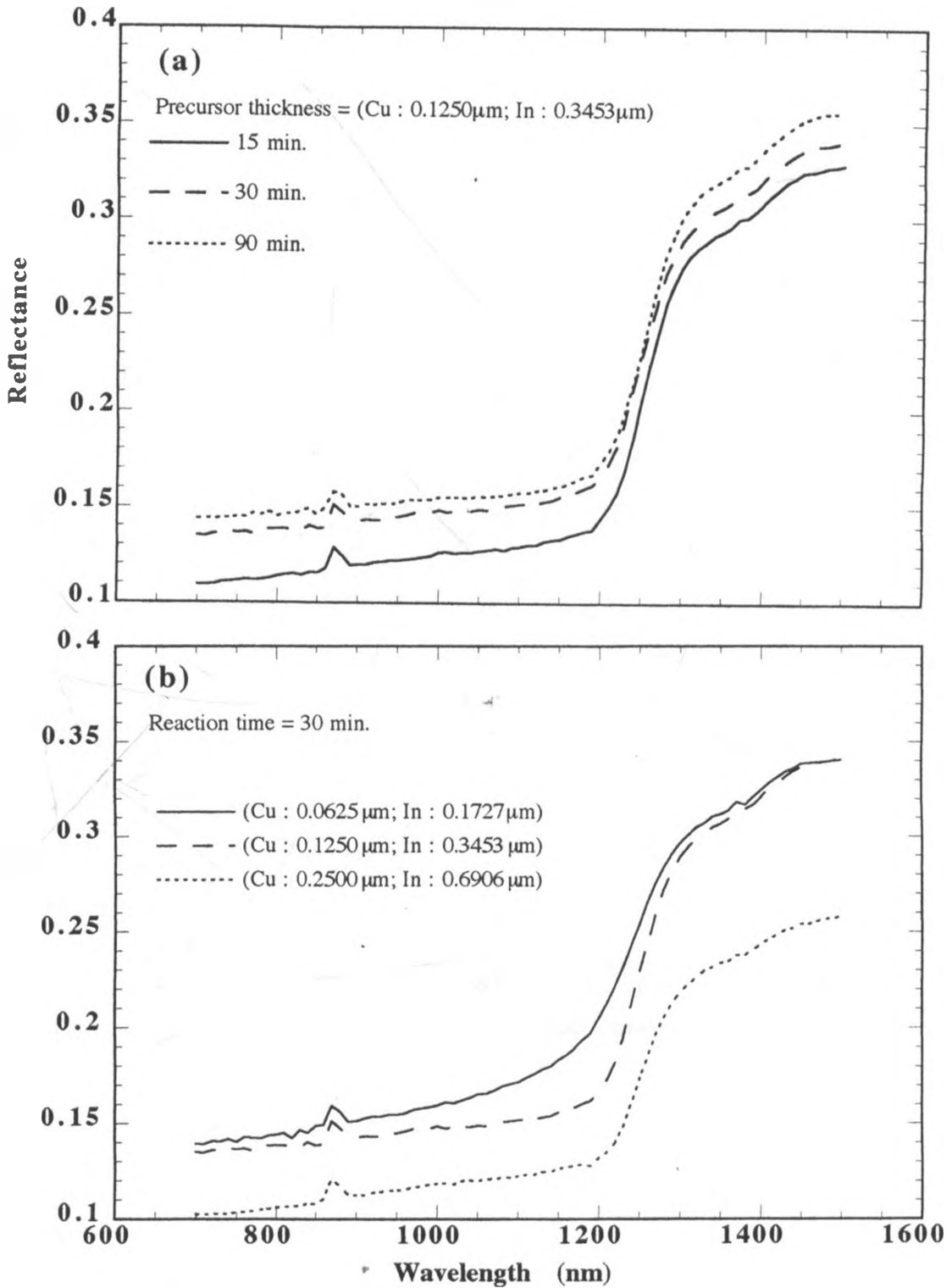
Figure 4.24. Variation of reflectance with: (a) reaction period   (b) absorber thicknesses.

Reaction temperature for CuInSe$_2$ films formation was 350 °C.
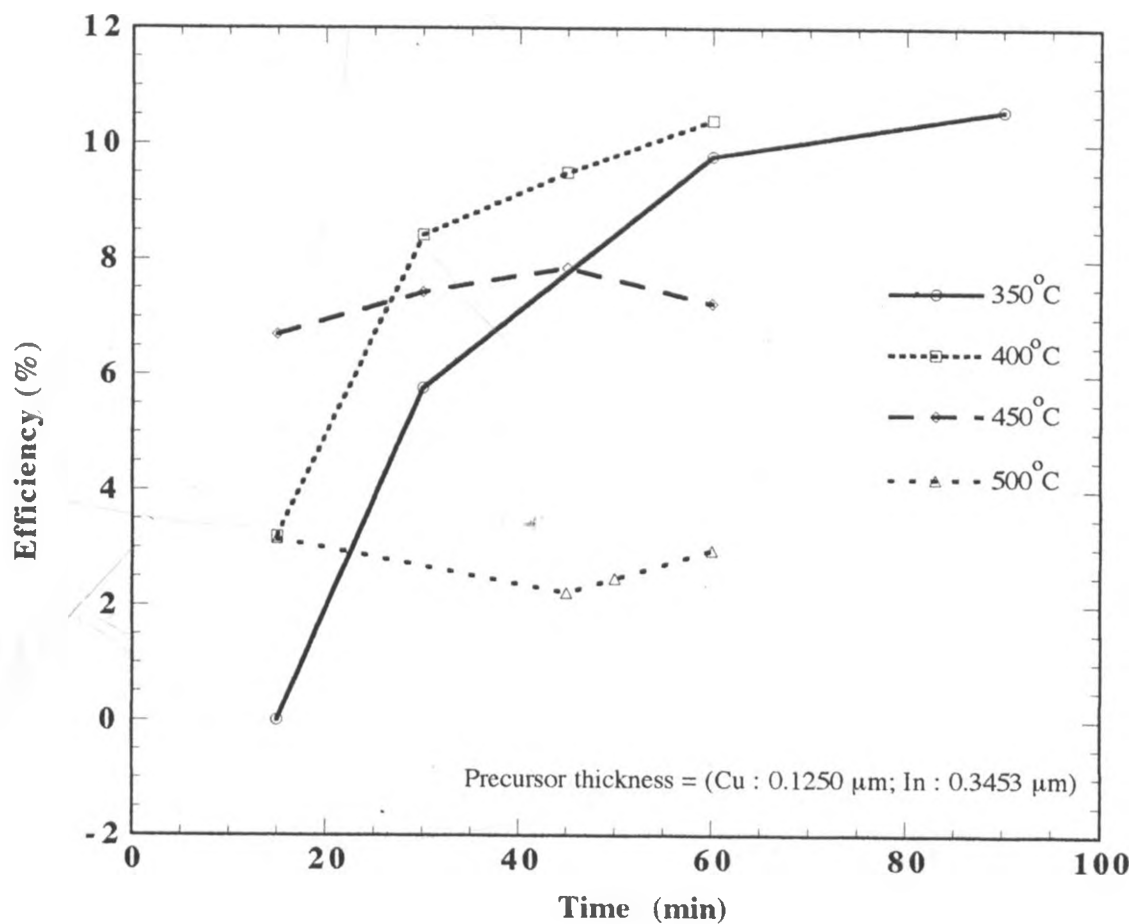
Figure 4.25. Efficiency versus reaction period for solar cells. Precursor thicknesses were (Cu : 0.1250 μm; In : 0.3453 μm) and were selenized at different reaction temperatures.
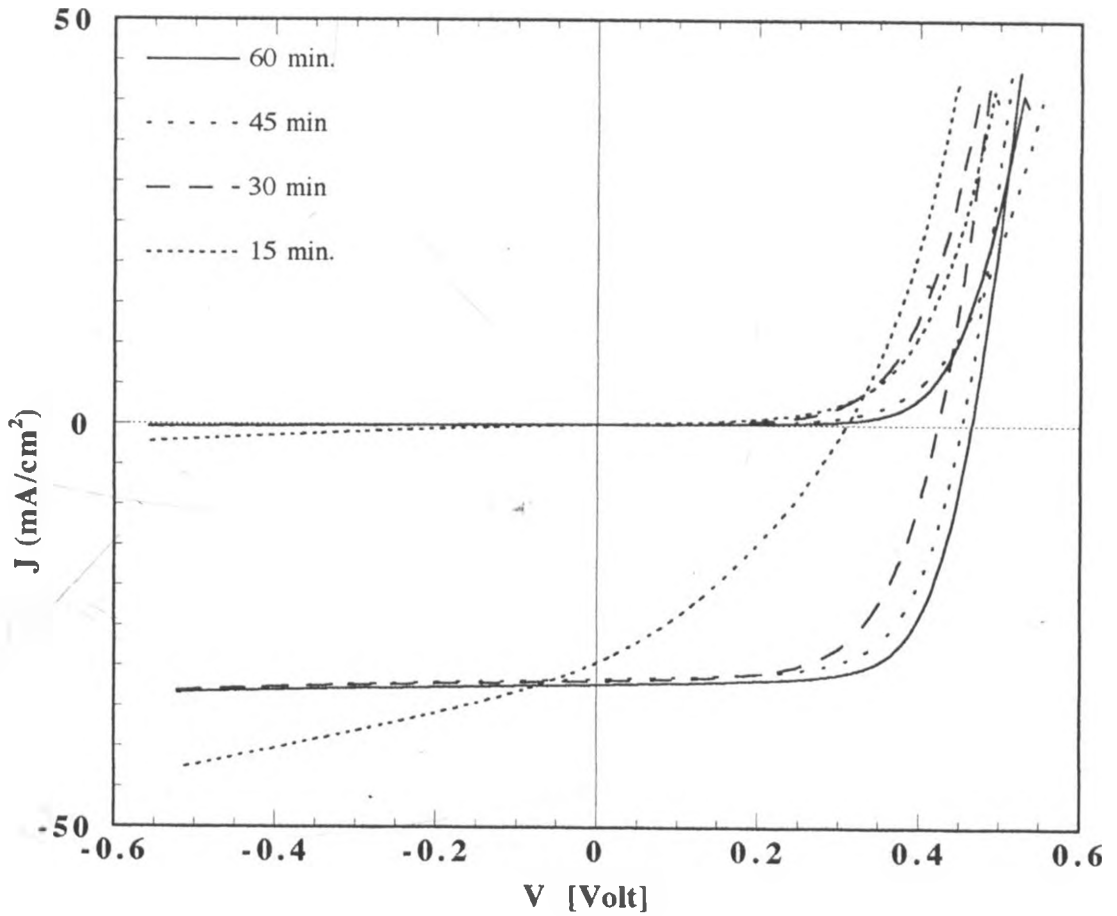
Figure 4.26. Light and dark J - V curves for solar cells for CuIn bilayers selenized at different reaction periods (in minutes). Reaction temperature and absorber thickness were 400 °C and 1.4 μm respectively.
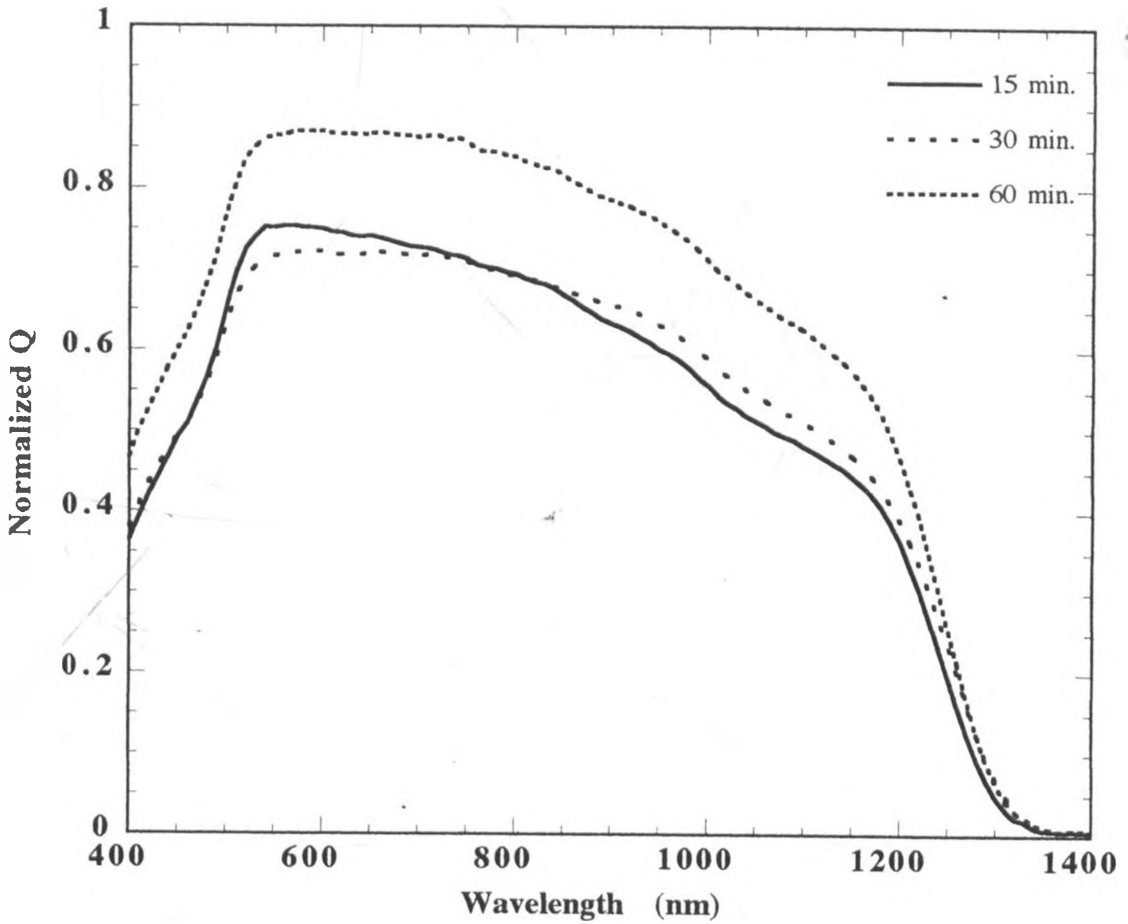
Figure 4.27. Quantum efficiency (Q) curves for solar cells fabricated using absorber layer selenized for reaction periods of 15, 30 and 60 minutes. Absorber thickness and reaction temperature were 1.4 μm and 400 °C, respectively.
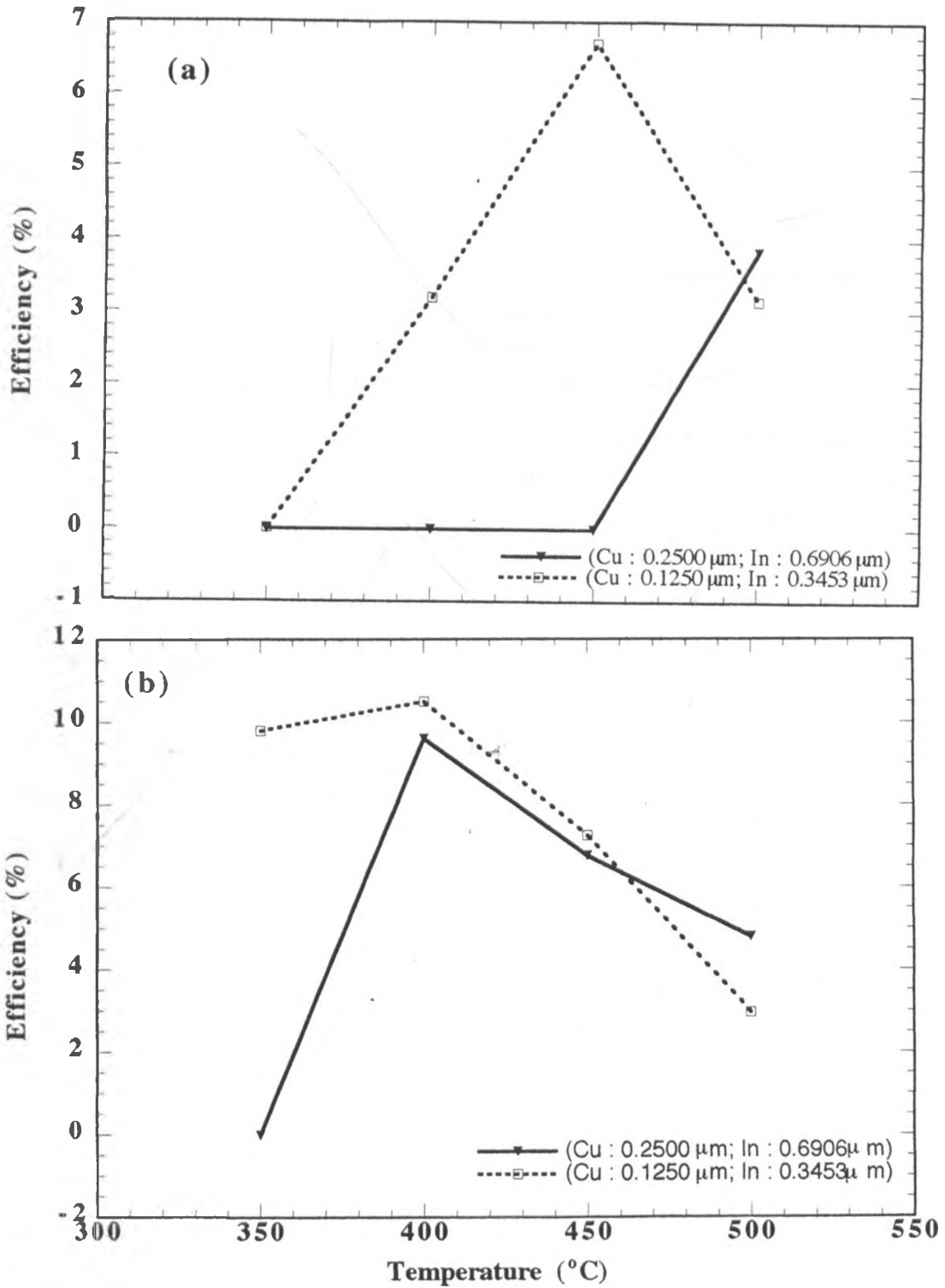
Figure 4.28. Solar cell efficiency with reaction temperature for CuInSe$_2$ based devices of different precursor thicknesses.
Reaction period was kept constant at: (a) 15 minutes (b) 60 minutes
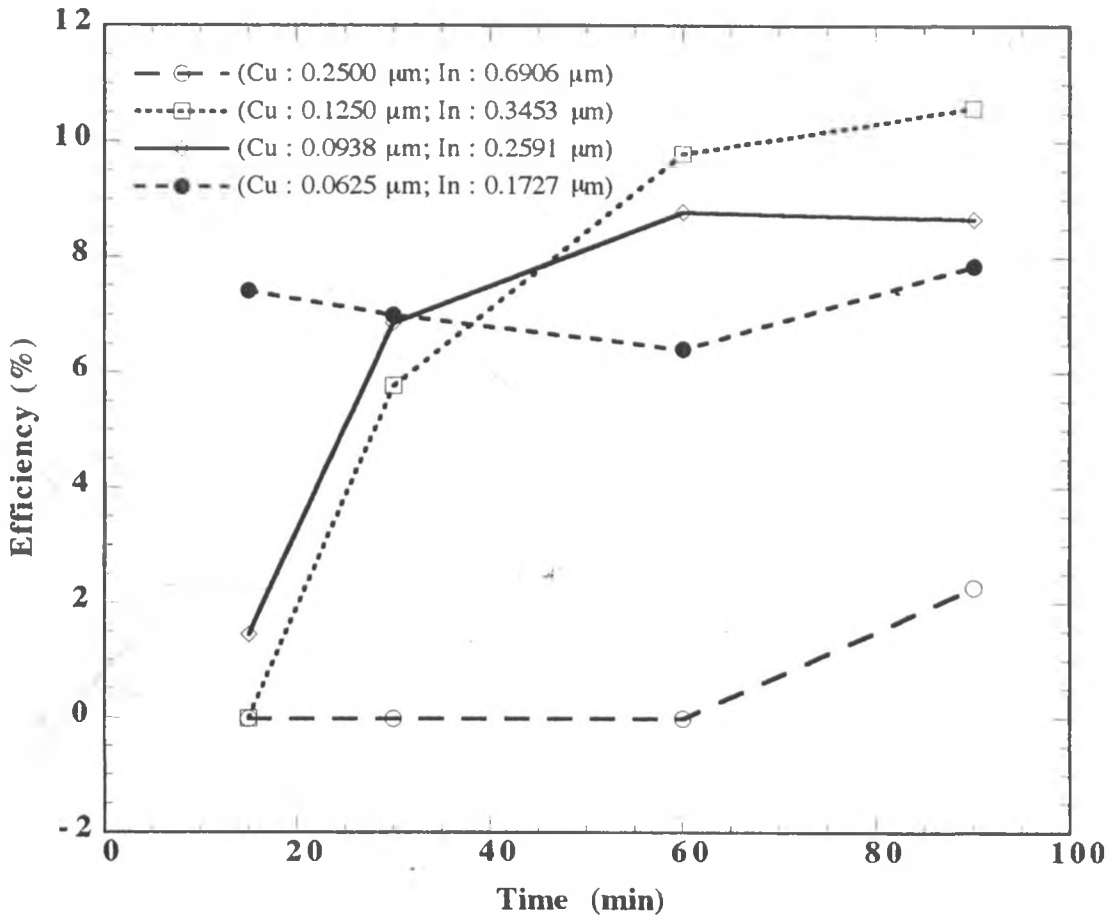
Figure 4.29. Cell efficiency with reaction period for devices fabricated using different precursor thicknesses. Reaction temperature was 350 °C.
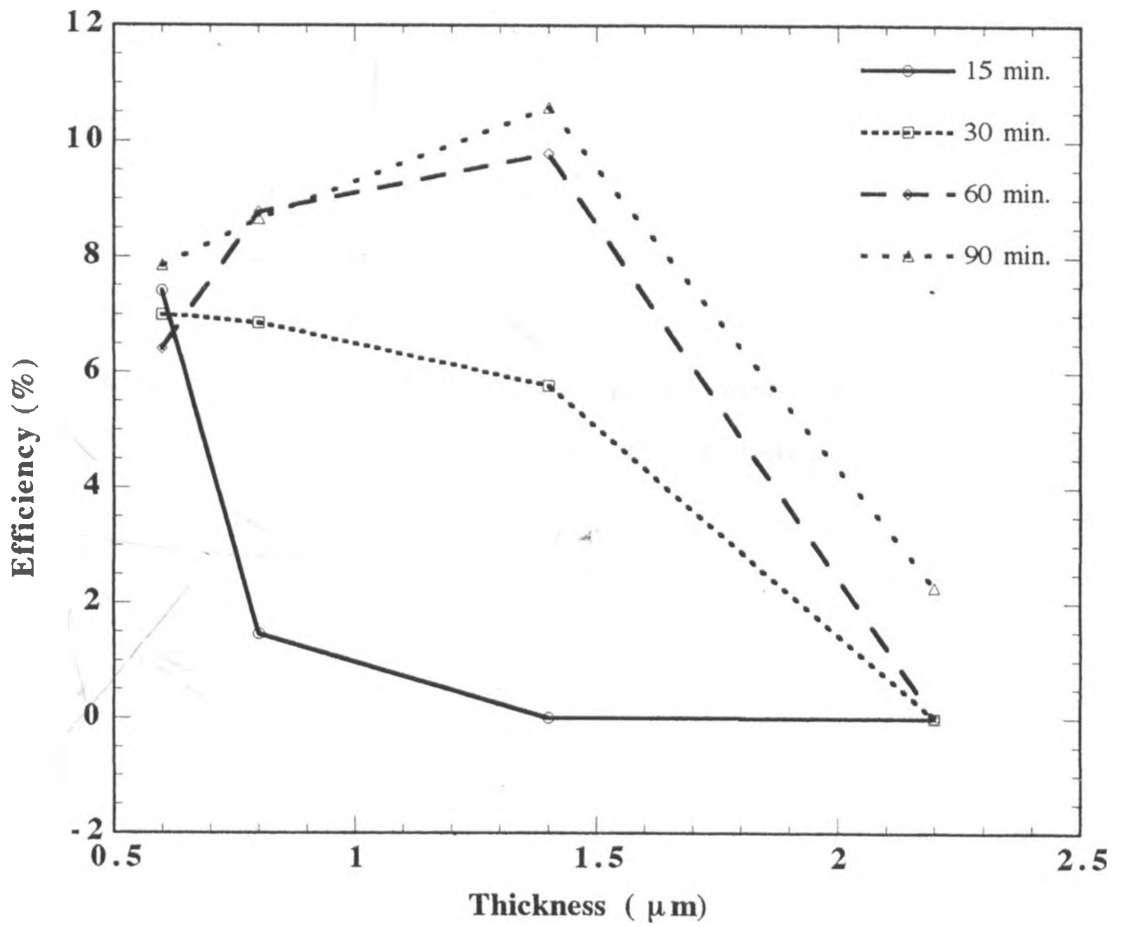
Figure 4.30. Solar cell efficiency versus absorber thickness selenized at different reaction periods. Reaction temperature was 350 °C.

CHAPTER FIVE

CONCLUSION AND SUGGESTIONS FOR FURTHER WORK

5.1 Conclusion

Resistivity of Cu and In films depends on vacuum deposition conditions as well as their thicknesses. For deposition parameters studied in this work, changes of resistivity for Cu films are within the order of 10^1 only. However, substantial changes in resistivity were observed for In films especially with varying sputtering pressure, film thickness, and deposition temperature. The resistivity changes were of order 10^3, 10^9, and 10^{11} for changes with sputtering pressure from 1.7 to 7.9×10^{-3} mbar, film thickness from 33 to 221 nm, and deposition temperature from 150 to 200 °C, respectively. We believe these results are useful especially for those using thinner Cu and In films (< 200 nm) to grow multilayer Cu/In/Cu/In.... for $CuInSe_2$ thin films by two stage process.

Efficiency of $CuInSe_2$ based solar cells have been found to depend on $CuInSe_2$ preparation conditions and precursor thickness. A semi quantitative description of the effect reaction period, reaction temperature and precursor thickness on formation of $CuInSe_2$ has helped to explain the phases observed and their effects on device performance.

The phases present were found to depend on reaction period, reaction temperature, and precursor thickness. A good device with efficiency greater than 10 % can be obtained using an absorber layer with a trace of InSe phase provided the number of InSe moles approaches zero. Qualitatively, the predicted and experimental number of moles with

reaction period for $CuInSe_2$ and InSe agreed very well. Quantitatively, there were some discrepancies between experimental and predicted number of moles. The time it takes for reaction is longer than that predicted by the kinetic model. Probably, a second process is involved which depends on thickness. The chemical kinetic model for reaction of CuIn precursors only takes into account chemical reaction rates with excess of Se. The method used in obtaining experimental data might also have contributed to the discrepancy between experimental and predicted number of moles. However, a definitive conclusion requires a detailed investigation. The number of moles of $CuInSe_2$ increased with reaction period while those of InSe were found to deplete with reaction period. This is consistent with device performance with respect to reaction period especially for reaction temperatures 350 and 400 °C.

Low reaction temperatures require long reaction periods and vice versa for complete reaction of CuIn precursors. This is consistent with high reaction rate constants for high reaction temperatures and low reaction rate constants for low reaction temperatures. At reaction temperatures greater than 400 °C, physical destruction of the $CuInSe_2$ film and $MoSe_2$ phase formation occurs.

Although the time for the precursors to react fully is independent thickness, there is a limit in solar cell efficiency which can be obtained for each precursor thickness. The limit in efficiency is not directly dependent on precursor thickness but it might be a balance between precursor thickness and probably absorption of light, especially for thinner precursors.

Cu/In ratio for selenized CuIn bilayers was found to decrease with decrease in precursor thickness. This was not expected because the starting Cu/In ratio of the precursors were kept constant for all precursor thicknesses. The change in Cu/In ratio

for selenized precursors with thickness might either be due to In loss being more for thicker CuIn bilayers or the EDS measurements for the thinner CuInse$_2$ films having errors. No correlation was found for composition of CuInSe$_2$ films with respect to reaction temperature which is contrary to literature findings. The slightly In rich selenized precursors produced the best cells which is in agreement with literature.

To conclude, the present study has given us fundamental information needed to develop and operate a CuInSe$_2$ based solar cell commercial scale process. For commercial considerations, the most interesting result is the 7.41 % efficiency obtained for a 0.6 μm thick CuInSe$_2$ absorber layer prepared for 15 minutes at reaction temperature of 350 °C. This provides hope as decreasing the reaction temperature, reaction period and CuInSe$_2$ thickness is the challenge for further CuInSe$_2$ research for this technology to be cost effective.

5.2 Suggestions for further work.

Systematic studies where CuInSe$_2$ based solar cells are fabricated with different starting metallic Cu and In resistivities in order to see how metallic resistivities is related to the final CuInSe$_2$ based solar cells can be interesting.

A detailed investigation requiring actual measurements of number of moles experimentally and comparing with those calculated from measured XRD intensities can be worth doing. This will give us a definitive conclusion for experimental and predicted number of moles for CuInSe$_2$ and InSe phases.

$CuInSe_2$ based solar cells with $CuInSe_2$ thickness less than 0.6 µm, prepared using reaction periods ≤ 15 minutes and reaction temperature ≤ 350 °C can be fabricated. Thinner CuIn precursors saves the starting Cu and In material while lower reaction temperatures and shorter reaction periods translate to lower operating costs. As device efficiencies rise and processes are simplified, we can expect to see the introduction of high-performance, high yield, reliable photovoltaic modules based on the $CuIn(Ga)Se_2$ absorber.

This work should also be extended to $Cu(In,Ga)(S,Se)_2$ based solar cells as recent trends in $CuInSe_2$ research and development focus exclusively on these high band-gap alloys.

REFERENCES

Alberts V. and Swanepoel R. (1996), Structural analysis of CuInSe$_2$ thin films prepared by selenization of Cu-In films, Journal of Materials Science: Materials in Electronics, **7**, p. 91.

Bai Y., Ford D. H., Rand J. A., Hall R. B., and Barnett A. M. (1997), 16.6% efficient silicon-film™ polycrystalline silicon solar cells, 26th IEEE Photovoltaic Specialist Conference (Anaheim, USA), p. 35.

Basol B. M. and Kapur V. K. (1990), Deposition of CuInSe$_2$ films by a two stage process utilizing e-beam evaporation, Proc. 21st IEEE Photovoltaic Specialists Conference (Kissiminee, USA), p. 418.

Basol B. M., Kapur V. K., Halani A., and Leidholm C. (1993), Copper indium diselenide thin film solar cells fabricated on flexible foil substrates, Solar Energy Materials and Solar Cells, **29**, p. 163.

Basol B. M., Kapur V. K., Leidholm C. R., Minnick A., and Halani A. (1994), Studies on substrates and contacts for CIS films and devices, Proc. IEEE First World Conference Photovoltaic Energy Conversion (Waikoloa, Hawai), **1**, p. 148.

Basol B. M., Kapur V. K., Leidholm C. R., Minnick A., and Halani A. (1994), Development of low cost CIS cells and modules, 12th NREL PV Prog. Rev., AIP Conference Series 306 (Colorado, USA), p. 79.

Behrisch R. (1981), *Sputtering by Particle Bombardment I*, **47**, (Springer, Berlin)

Behrisch R. (1983), *Sputtering by Particle Bombardment II*, **52**, (Springer, Berlin)

Behrisch R. (1991), *Sputtering by Particle Bombardment III*, **64** , (Springer, Berlin)

Birkmire R. W. and Eser E. (1997), Polycrystalline thin film solar cells: Present status and future potential, Annu. Rev. Mater. Sci., **27**, p. 625.

Birkmire R. W. (1993), High Efficiency $CuInSe_2$ Solar Cells Using the Selenization Process, Technical Digest of the International PVSEC-7 (Nagoya, Japan), p. 527.

Birkmire R. W. (1997), Recent progress and critical issues in thin film polycrystalline solar cells and modules, 26th IEEE Photovoltaic Specialist Conference (Anaheim, USA), p. 295.

Birkmire R. W. (1998), Private communication.

Chapin D. M., Fuller C. S., and Pearson G. L. (1954), A new silicon p-n junction photocell for converting solar radiation into electrical power, Journal of Applied Physics, **25**, p. 676.

Chaplin D. M., Fuller C. S., and Pearson G. L. (1957), US Patent Number 2780

Chapman B. (1980), *Glow Discharge Processes* (Wiley, New York)

Cheremisinoff P. N. (1978), *Principles and Applications of Solar Energy* (Ann. Arbor Science, Michigan).

Chu T. L. and Chu S. S. (1993), Recent progress in thin-film cadmium telluride solar cells, Progress in Photovoltaics: Research and Applications, **1**, p. 31.

Craig S. and Harding G. L. (1981A), Solar selective properties of rough sputtered copper films, Solar Energy Mater., **4**, p. 245.

Craig S. and Harding G. L. (1981B), Effects of argon pressure and substrate temperature on the structure and properties of sputtered Copper films, J. Vac. Sci. Technol., **19**, p. 205.

Cullity B. D. (1978), *Elements of X-Ray Diffraction* (2nd edition, Addison-Wesley Publishing company, Inc., Massachusetts).

Devaney W. E., and Mickelson R. A. (1986), Solar Cells, **16**, p. 131.

Dimmler B., Content A., and Shock H. W. (1991), A new co-evaporation process for high quality CuInSe$_2$ devices, Proc. of the 10th European Photovoltaic Solar Energy Conference (Lisbon, Portugal), p. 875.

Dimmler B., Dittrich H., and Schock H. W. (1988), Structure and morphology of evaporated bilayer and selenized CuInSe$_2$ films, 20th IEEE Photovoltaic Specialist Conference (Las Vegas, USA), p. 1426.

Dittrich H., Prinz U., Szot J., and Schock H. W. (1988), Analysis of reaction kinetics of selenized CuInSe$_2$ and CuGaSe$_2$ thin films, 9th E.C. Photovoltaic Solar Energy Conference (Freiburg, Germany), p. 163.

Doña J. M. and Herrero J. (1992), Chemical bath deposition of CdS thin films: Electrochemical in-situ kinetic studies, J. Electrochem. Soc., **139**, p. 2810.

Fearheiley M. L. (1986), Phase relations in the Cu, In Se system and the growth $CuInSe_2$ single crystals, Solar Cells, **16**, p. 91.

Ford D. H., Barnett A. M., Hall R. B., Kendall C. L., and Rand J. A. (1996), High power commercial silicon-film™ solar cells, Proc. 25th IEEE Photovoltaic Specialist Conference (Washington DC, USA), p. 601.

Fraas L. M., Avery J. E., Sundaram V. S., Kinh V. T., Davenport T. M., Yerkcs J. W., Gee J. M. and Emery K. A. (1990), Over 35 % efficient GaAs/GaSb stacked concentrator cell assemblies for terrestrial applications, Proc. 21st IEEE Photovoltaic Specialists Conference (Kissimimee, USA), p. 190.

Gabor R. A. (1995), The conversion of $(In, Ga)_2Se_3$ Thin Films to $Cu(In, Ga)Se_2$ for application to Photovoltaic solar cells, Ph.D. Thesis, University of Colorado.

Garg J. C., Sharma R. P., and Sharma K. C. (1988), Characterization of $p-CuInSe_2$ films for photovoltaics grown by a chemical deposition technique, Thin Solid Films, **164**, p. 269.

Gay R., Dietrich M., Fredric C., Jensen C., Knapp K., Tarrant D., and Willett D. (1994), Efficiency and Process Improvements in $CuInSe_2$-based Modules, 12th European Photovoltaic Solar Energy Conference (Amsterdam, The Netherlands), p. 935.

Gillespie T. J., Lanning B. R., and Marshall C. H. (1997), Large area copper Indium diselenide (CIS) process, control and manufacturing, Proc. IEEE 26th Photovoltaic Specialist Conference (Anaheim, USA), p. 403.

Glocker D. A and Shah S. I. (1995), *Handbook of Thin Film Processes Technology*, (Institute of Physics Publishing, Bristol and Philadelphia).

Green M. A. (1982), *Solar Cells*, (Printice Hall, Inc, New Jersey).

Green M. A. (1993), Silicon solar cells: Evolution, high-efficiency design and efficiency enhancements, Semiconductor Sci. Technology, **8**, p. 1.

Green M. A. and Emery K. (1993), Short communication: Solar cell efficiency tables(version 2), Progress in Photovoltaics: Research and Applications, **1**, p 225.

Guha S. (1996), Amorphous silicon alloy cells and modules-opportunities and challenges, 25th IEEE Photovoltaic Specialist Conference (Washington, DC, USA), p. 1017.

Guha S., Yang J., Banerjee A., Glatfelter T., Hoffman K., Ovshinsky S. R., Izu M., Ovshinsky H. C., and Deng X. (1994), Amorphous silicon alloy photovoltaic technology - from R& D to production, Mat. Res. Soc. **336**, p. 645.

Gupta A., Shirakata S., Isomura S. (1994), Studies on CuIn precursor for preparation of $CuInSe_2$ thin films by the selenization technique, Solar Energy Materials and Solar Cells, **32**, p. 137.

Hahn H., Frank G., Klinger W., Meyer A. D., and Storger G. Z. (1953), Über einige ternäre chalkogenide mit chalkopyritstruktur, Anorrg. Allgem. chem, **271**, p. 153.

Hall P. M. and Morabito J. M. (1976), Diffusion Mechanisms in the Pd/Au Thin Film system and the correlation of resistivity changes with auger electron spectroscopy and rutherford backscattering profiles, Thin Solid Films, **33**, p. 107.

Hamakawa Y., Ma W., and Okamoto H. (1993), Recent progress in Amorphous silicon solar cells and their technologies, MRS Bulletin, **October**, p. 38.

Hariskos D., Ruckh M., Rühle U., Walter T., Schock H. W. (1994), A novel cadmium free buffer layer for $Cu(In, Ga)Se_2$ based solar cells, Proc. IEEE First World Conference. Photovoltaic Energy Conversion (Waikoloa, Hawai), p. 91.

Hecht E. (1998), *Optics* (Addison Wesley Longmann, Inc., New York), p.67

Hedstrom J., Ohlsen H., Bodegard M., Kylner A., Stolt L., Hariskos D., Ruckh M., and Schock H. W. (1993), $ZnO/CdS/Cu(InGa)Se_2$ Thin Film Solar Cells with improved Performance, 23rd IEEE Photovoltaic Specialists Conference (Louisville, USA), p. 364.

Hovel H. J. (1975), *Solar cells, Semiconductor and Semimetal Series*, **II,** (Academic Press, New York) , p. 217.

Hovel H. J. (1975), *Solar Cells, Semiconductors and Semimetals Series*, **II,** (Academic Press, New York) , p. 16 - 19,

Jackson S. C., Baron B. N., Rocheleau R. E., and Russell T. W. F. (1987), A chemical reaction model for physical vapor deposition of compound semiconductor films, AIChE Journal, **33**, p. 711

Jay F. (Ed.) (1977), *IEEE Standard Dictionary of Electrical and Electronics Terms (Second Edition*, The Institute of Electrical and Electronics Engineers, Inc., New York).

Jensen C. L., Tarrant D. E., Ermer J. H., and Pollock G. A. (1993), The role of Gallium in $CuInSe_2$ solar cells fabricated by a two stage method, Proc. 23rd IEEE Photovoltaic Specialists Conference (Louisville, USA), p. 577.

Jones P. A., Jackson A. D., Lickiss P. D., Pilkington R. D., and Tomlison R. D. (1994), The plasma enhanced chemical vapour deposition of $CuInSe_2$, Thin Solid Films, **238**, p. 4.

Kaye G. W. C. and laby T. H. (1971), *Physical and Chemical Constants* (Longman Group Ltd, New York).

Keavney C. J., Haven V. E. and Vernon S. M. (1990), Emitter structures in MOCVD InP solar cells, Proc. 21st IEEE Photovoltaic Specialists Conference (Kissimimee, USA), p. 141.

Kessler J., Ruckh M., Hariskos D., Rühle U., Menner R., and Schock H. W. (1993), Interface engineering between $CuInSe_2$ and ZnO, Proc. 23rd IEEE Photovoltaic Specialists Conference (Louisville, USA), p. 447.

Kiely C. J., Pond R. C., Kenshole G., and Rockett A. (1991), A TEM study of the crystallography and defect structures of single crystal and polycrystalline copper indium diselenide, Phil. Mag., **A63**, p. 1249.

Klenk R. (1993), Polykristalline CuGaSe$_2$, Dünnschichten für die Photovoltaik-Herstellung und Charakterisierung von Absorbern und Heteroübergängen, Doktorarbeit, Stuttgart.

Klenk R. and Schock H. (1994), Photocurrent collection in thin film solar cells-calculation and characterization for CuGaSe$_2$/(Zn,Cd)S, Proc. 12th European PV Solar Energy Conference (Amsterdam, The Netherlands), p. 1588.

Kumar S.R., Gore R. B., and Pandey R. K. (1992), Preparation and properties of Cu-In alloy precursor for CuInSe$_2$ films, Solar Energy Mater. Solar Cells, **26**, p. 149.

Lakshmikumar S. T. and Rastogi A. C. (1994), Selenization of Cu and In thin films for the preparation of selenide photo-absorber layers in solar cells using Se vapor source, Solar Energy Mater. and Solar Cells, **32**, p. 7.

Liu X. X. and Sites J. R. (1994), Solar cell collection efficiency and its variation with voltage, J. Appl. Phys., **75**, p. 577.

Lyding J. W., Hess K., and Kizilyalli I. C. (1996), Appl. Phys. Lett., **68**, p. 2526.

Madan A., Ovshinsky S. R., and Czubatyj W. (1980), Some electrical and optical Properties of a-Si:F:H Alloys, Journal of Electronic Materials, **9**, p. 385.

Marudachalam M. (1996), Processing, structure and diffusion in $CuIn_xGa_{1-x}SE_2$ thin films for solar cells, Ph.D. Thesis, University of Delaware.

Marudachalam M., Hichri H., Klenk R., Birkmire R. W., Shafarman W. N. and Schultz J. M. (1995), Preparation of Homogeneous $Cu(InGa)Se_2$ films by selenization of Metal Precursors in H_2Se Atmosphere, Appl. Phys. Lett., **67**, p. 3978.

Mason W. P. (1956), *Piezoelectric Crystals and their Application to Ultrasonics*, (D. Van Nostrand company, Inc., Princeton).

Mickelsen R. A. and Chen W. S. (1981), Development of a 9.4 % efficient thin-film $CuInSe_2/CdS$ solar cell, Proc. 15th IEEE Photovoltaic Specialist Conference (Kissimmee, USA), p. 800.

Mickelsen R. A. and Chen W. S. (1982), US Patent number 4335266.

Mickelsen R. A., Chen W. S., Stanbery B. I., Bursh H., Stewart J. M., Hsiao Y. R. and Devaney W. (1985), Development of $CuInSe_2$ for space applications, Proceedings of the 18th IEEE Photovoltaic Specialist Conference (Kissimime, USA), p. 1069.

Mooney J. B. and Lamoreaux R. H. (1986), Spray pyrolysis of $CuInSe_2$, Solar Cells, **16**, p. 211.

Musil J., Bell A. J., and Cepera M. , (1995), Deposition of copper films by unbalanced D. C. magnetron sputtering, Czech. J. Phys., **45**, p. 249.

Mwamburi M. (1994), The preparation and characterization of ITO/Si solar cells, M.Phil Thesis, Moi University.

Nadenau V., Braunger D., Hariskos D., Kaiser M., Koble Ch., Oberacker A., Ruckh M., Ruhle U., Schaffler R., Schmid D., Walter T., Zweigart S., and Schock H. W. (1995), Solar cells based on CuInSe$_2$ and related compounds: Material and Device Properties and Processing, Progress in Photovoltaics: Research and Application, **3**, p. 363.

NASA Lewis Research Center (1977), Terrestrial Photovoltaic measurement procedures, ERDA/NASA/1022-77/16, TM 73702.

Neumann H. and Tomlinson R. D. (1990), Relation between electrical properties and composition in CuInSe$_2$ single crystals, Solar Cells, **28**, p. 301.

Noufi R. and Powell R .(1985), Thin-film copper indium diselenide/cadmium sulfide solar cells, Proc. 6th European Photovoltaic Solar Energy Conference. (London, UK), p. 761.

Ohring M. (1992), *The Material Science Thin Films*, (Academic Press, Inc., New York).

Ohyama H., Aramoto T., Kumazawa S., Higuchi H., Arita T., Shibutani S., Nishio T., Nakajima J., Tsuji M., Hanafusa A., Hibino T., Omura K., and Murozono M. (1997), 16.0% efficient thin-film CdS/CdTe solar cells, 26th IEEE Photovoltaic Specialist Conference (Anaheim, USA), p. 343.

Okuma S. and Hirai H. (1996), Scaling of current-resistivity isotherms of indium films in a magnetic field, Physica B, **228**, p. 272.

Orbey N., Hichri H., Birkmire R. W., and Russell T. W. F. (1997), Effect of Temperature on Copper Indium Selenization, Progress in Photovoltaics: Research and application, **5**, p. 237.

Orbey N., Norsworthy G., Birkmire R. W., and Russel T. W. F. (1998), Reaction analysis of the formation of $CuInse_2$ films in a physical vapor deposition reactor, submitted for publication.

P/N 102800, *Thickness model TM-100/200, TN-100R/200R and TN-300 operation and service manual* (Maxtek, Inc, California).

Pal R., Chattopadhyay K. K., Chaudhuri S., and Pal A. K. (1994), Photoconductivity in $CuInSe_2$ films, Solar Energy Mater. Solar Cells, **33**, p. 241.

Palatnik L. S and Rogachera E. L. (1967), Phase diagrams and structure of some semiconductor $A_2^I C^{VI}$-$B_2^{III}C^{VI}$ alloys, Soviet Physics-Doklady, **12**, p.503.

Parretta A. (1993), $CuInSe_2$ preparation by sputtering and selenization, 3rd EUROCIS II Meeting, 3-9 June, 1993 (Stockholm, Sweden).

Parretta A., Crocchiolo M., Pellegrino M., Quercia L., Addonizio M. L, Agati A., and Menna P. (1992), Properties of sputtered metallic alloys for $CuInSe_2$ based solar cells, Proc. 11th E.C. Photovoltaic Energy Conference (Montreux, Switzerland), p. 850.

Parretta and Rubino (1995), Kinetics of intermetallics transformation in sputtered Cu-In alloys studied by electrical resistance measurements, Solid State Communications, **96**, p. 767.

Parthe E. (1967), Wurtzite and Zinc blend type Structures, Intermetallic Compounds, Ed. by J. H. Westbrook (John Wiley and Sons, New York).

Pern F. J., Noufi R., Mason A. and Franz A. (1991), Characterizations of electrodeposited $CuInSe_2$ thin films: structure, deposition and formation mechanisms, Thin Solid Films, **202,** p. 299.

Philibert J. (1991), Reactive diffusion in thin films, Applied Surface Sciences, **53**, p. 74.

Phillips J. E. (1990), Determination of diffusion length with bi-facial spectral response, Proc. 21st IEEE Photovoltaic Specialists Conference (Kissimmee, USA), p. 782.

Phillips J. E. and Roy M. (1988), Resistive and photoconductive effects in spectral measurements, Proc. 20th IEEE Photovoltaic Specialist Conference (Las Vegas, USA), p. 1614.

Probst V., Karg F., Rimmasch J., Riedl W., Stetter W., Harms H., and Eibl O. (1996), Advanced Stacked Elemental Layer Process for $Cu(InGa)Se_2$ Thin Film Photovoltaic Devices, Mat. Res. Soc. Symp. Proc., **426.** p. 165.

Probst V., Rimmasch J., Setter W., Harms H., Riedel, Holz J., and Karg F. (1995), Improved CIS thin film solar cells through novel impurity control techniques, Proc. 13th European Photovoltaic Solar Energy Conference (Nice, France), p. 2123.

Rincón C. and Gonzalez J. (1986), Temperature dependence of the bandgap in $CuInSe_2$, Solar Cells, **16**, p. 357.

Rocheleau R. E., Meakin J. D., and Birkmire R. W. (1987), Tolerance of $CuInSe_2$ cell performance to variations in film composition and the implications for large area cell manufacture, Proc. 19th IEEE Photovoltaic Specialists Conference (New Orleans, USA), p. 972.

Rockett A. and Birkmire R. W. (1991), $CuInSe_2$ for photovoltaic applications, J. Appl. Phys., **70**, p. R81.

Rockett A., Lommasson T. C., Yang L. C., Talieh H., Campos P., and Thornton J. A. (1988), Deposition of $CuInSe_2$ by the hybrid sputtering and evaporation method, Proc. 20th IEEE Photovoltaic Specialist Conference (Las Vegas, USA), p. 1505.

Runyan W. R. (1965), *Silicon Semiconductor Technology, Texas Instruments Electronics Series* (Mcgraw - Hill book company, New York).

Sachan V. and Meakin J. D. (1993), Study of phases formed during production of copper indium diselenide by reacting copper, indium and selenium layers, Solar Cells, Solar Energy Mater, **30**, p. 147.

Sammann A. N. Y., Abdul-Karim N., Abdul-Hussein N., Tomlison R. D., Hill A. E., and Armour D. G. (1980), Jpn J. Appl. Phys., **19-3**, p. 15

Sato H., Hama T., Niemi E., Ichikawa Y. and Sakai H. (1993), Fabrication of high efficiency CuIn(Ga)Se$_2$ Thin Film Solar Cell by selenization with H$_2$Se, Proc. 23rd IEEE Photovoltaic Specialists Conference (Louisville, USA), p. 521.

Shafarman W. N. (1998), Private communication.

Shafarman W. N., Klenk R., and McCandless B. E. (1996), Device and Material Characterization of Cu(InGa)Se$_2$ Solar Cells with increasing Band Gap, J. Appl. Phys., **79**, p. 7324.

Shirland F. A. (1966), The history, Design, Fabrication and performance of CdS Thin Film Solar Cells, Advanced Energy Conversion, **6**, p. 201.

Sirringhaus H., Theiss S. D., Khan A., and Wagner S. (1997), Self-passivated copper gates for thin film silicon transistors, Mater. Res. Soc. Symp. Proc. **446**, p. 59.

Spear W. E. and LeComber P. G. (1975), Substitutional doping of amorphous silicon, Solid State Communications, **17**, p. 1193.

Staebler D. L. and Wronski C. R. (1977), Reversible conductivity changes in discharge-produced amorphous Si, Applied Physics Letter, **31**, p. 292.

Stone J. L. (1991), Solar Energy materials, **23**, p. 117.

Stone J. L. (1993), Photovoltaics: unlimited electrical energy from the sun, Physics Today, **September**, p. 22.

Strel'chenko S. S., Bondar S. A., Molodyk A. D., Berger L. I. and Balanevskaya A. E. (1969), Mass-spectrometric investigation of the sublimation of certain ternary semiconductors of the $A^IB^{III}C^{VI}_2$, Inorg. Mater., **5**, p. 593.

Subramanian P. R. and Laughlin D. E. (1989), The Cu-In (copper-Indium) system, Bulletin of Alloy Phase Diagrams, **10**, p. 554.

Suntola T. (1993), CdTe Thin-Film solar cells, MRS Bulletin, **October**, p. 45

Szot J. and Prinz U. (1989), Selenization of metallic Cu-In films for $CuInSe_2$ solar cells, J. Appl. Phys., **66**, p. 6077.

Thornton J. A., Lommasson T. C., Talieh H., and Tseng B. H. (1988), Solar Cells, **24**, p. 1

Tuttle J. R., Contreras M. A., Gillespie T. J., Ramanathan K. R., Tennant A. L., Keane J., Gabor A. M., and Noufi R. (1995), 17.1 % Efficient $Cu(InGa)Se_2$-based Thin Film Solar Cells, Progress in Photovoltaics: Research and Applications, **3**, p. 235.

Tuttle J. R., Ward J. S., Duda A., Berens T. A., Contreras M. A., Ramanathan K., Tennant A. L., Keane J., Cole E. D., Emery K., and Noufi R. (1996), Proc. Mat. Res. Soc. Symp.,**426**, p. 143.

Van de Walle C. G. (1998), Hydrogen in silicon: Fundamental properties and consequences or devices, J. Vac. Sci. Technol, **A16,** p. 1767.

Varela M., Bertran E., Manchon M., Esteve J., and Morenza J. L. (1986), Optical properties of co-evaporated $CuInSe_2$ thin films, J. Phys. D, **19,** p. 127.

Varin Jr. R. D. (1991), Selenization: Formation of copper indium diselenide ($CuInSe_2$) polycrystalline thin films for photovoltaic devices, Ph.D. Thesis, University of Delaware.

Velthaus K. O., Kessler J., Ruckh M., Hariskos D., Schmidt D., and Schock H. W. (1992), Novel buffer layers for the $CuInSe_2$/buffer/ZnO devices, Proc. 11th E. Photovoltaic Solar Energy Conference (Montreaux, Switzerland), p. 842

Verma S. (1993), A chemical reactor and reaction engineering analysis of the formation of $CuInSe_2$ by selenization, Ph.D. thesis, University of Delaware.

Verma S., Orbey N., Birkmire R. W., and Russel T. W. F. (1996), Chemical Reaction Analysis of Copper Indium Selenization, Progress in Photovoltaics: Research and Applications, **4,** p. 341.

Verma S., Varrin Jr., R. D., Birkmire R. W., and Russel T. W. F. (1991), Critical process issues in selenization, Proc. 22nd IEEE PV Specialists Conference (Las Vegas, USA), p. 914.

Verma S., Yamanaka S., McCandless B. E., Birkmire R. W., and Russel T. W. F. (1992), Reaction pathways to $CuInSe_2$ formation by selenization, Proc. 11th EC Photovoltaic Solar Energy Conference (Montreaux, Switzerland), p. 807.

Vernon S. M., Tobin S. P., Haven V. E., Geoffroy L. M., and Sanfacon M. M. (1991), High-efficiency concentrator cells from GaAs on Si, Proc. 22nd IEEE Photovoltaic Specialists Conference (Las Vegas, USA), p. 353.

Vinci R. P., Zielinski E. M., and Bravman J. C. (1995), Thermal strain and stress in copper thin films. Thin Solid Films, **262**, p. 142.

Vossen J. L. and Kern W. (1978), *Thin Film Processes* (Academic press, New York).

Walter T. and Schock H. W. (1996), High efficiency thin film solar cells based on chalcopyrite semiconductors, EUROSUN (Freiburg, Germany).

Walter T., Content A., Velthaus K. O., and Schock H. W. (1992), Solar cells based on $CuIn(Se, S)_2$, Sol. Energy Mat. Solar Cells, **26**, p. 357.

Wanlass M. W., Coutts T. J., Ward J. S., Emery K. A., Gessert T. A., and Osterwald C. R. (1990), Advanced high-efficiency concentrator tandem solar cells, Proc. 21st IEEE PV Specialists Conference (Kissimimee, USA), p. 38

Ward J. S., Wanlass M. W., Coutts T. J., Emery K. A., and Osterwald C. R. (1991), InP concentrator solar cells, Proc. 22nd IEEE PV Specialists Conference(Las Vegas, USA), p.365.

Warner A. W. and Stockbridge C. D. (1963), Quartz resonators; reduction of transient frequency excursion due to temperature change, J. Appl. Phys., **34**, p. 437.

Wielder S. (1982), *An Introduction to Solar Energy for Scientist and Engineers* (John Wiley and Sons, Inc., New York).

Yamanaka S., McCandles B. and Birkmire R. W. (1993), Reaction chemistry of $CuInSe_2$ formation by selenization using elemental Se, Proc. 23rd IEEE Photovoltaic Specialists Conference, (Louisville, USA), p. 607.

Yang J., Banerjee A., Glatfelter T., Sugiyama S., and Guha S. (1997), Recent progress in amorphous silicon alloy leading to 13 % stable cell efficiency, 26th IEEE Photovoltaic Specialist Conference (Anaheim, USA), p. 563.

Zanzucchi P. J., Wronski C. R., and Carlson D. E. (1977), Optical and photoconductive properties of produced amorphous silicon, Journal of Applied Physics, **48**, p. 5227.

Zweibel K. (1992), Toward low cost CdTe PV, International Journal of Solar Energy, **12**, p. 285.

APPENDICES

APPENDIX A

Determination of XRD intensity per unit mole for species i (K_i)

Use of pure samples of $Cu_{11}In_9$, In_2Se, InSe and $CuInSe_2$ on Mo coated glass is the standard method for determination of K_i value. The K_i value can be obtained from the following formula:

$$K_i = I_i * \mu_m \qquad\qquad (a1)$$

where μ_m is the linear mass absorption coefficient. Verma (1993) suggests to normalize pure component intensities by dividing with the Mo intensity (Method I). However, more accurate mole calculations were obtained by use of K_i values without dividing the pure intensities by the Mo intensity (Method II) [Birkmire, 1998]. This is attributed to the fact that Mo is not good as a standard as it was found to change orientation. The K_i values obtained by both methods are given in Table A.1.

Table A.1. K_i values of pure species [Birkmire, 1998].

Species	K_i, Method I	K_i, Method II
$Cu_{11}In_9$	270	11.95
In	204	25.79
In_2Se	4InSe	4.22
InSe	52	5.56
CuSe	20	3.20
Cu_2Se	22	3.06
$CuInSe_2$	430	15.69

APPENDIX B

Relationship between Ar flow rate and sputtering pressure.

For the sputtering equipment at the Solar Energy Group, University of Dar es Salaam, the sputtering pressure varies linearly with Ar flow rate:

$$y = (6.890 \times 10^{-5}) x + 0.001$$

where y is the sputtering pressure in mbar and x is the Ar flow rate in ml/min. Graphical representation is given is Figure B.1.
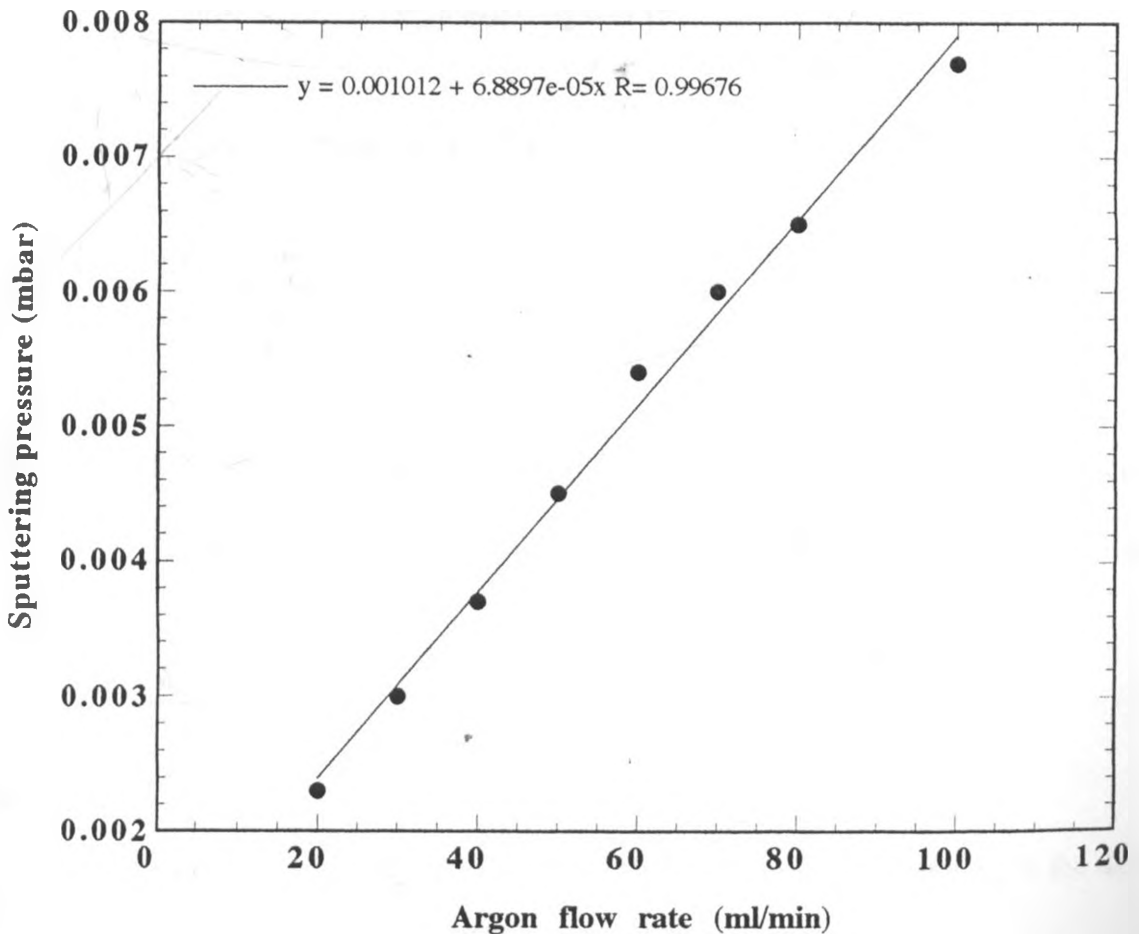

Figure B.1. Calibration graph for sputtering pressure with Ar flow rate.

APPENDIX C

Elemental thickness calculations for a given Cu/In molar ratio.

The relationship between thickness of Cu and In films for a given Cu/In molar ratio, R, can be written as:

$$R = \frac{N_{Cu}}{N_{In}} = \left(\frac{M_{Cu}}{Z_{Cu}} \right) \Big/ \left(\frac{M_{In}}{Z_{In}} \right) \qquad\qquad (c1)$$

where N_{Cu} is the number of moles of Cu film, N_{In} is the number of moles of In film, M_{cu} is the mass of Cu film, M_{In} is the mass of In film, Z_{cu} is the atomic weight of Copper and Z_{In} is the atomic weight of In.

Rearranging equation c1, we get

$$\frac{M_{Cu}}{M_{In}} = R \frac{Z_{Cu}}{Z_{In}} \qquad\qquad (c2)$$

Since Mass = Volume × Density, Volume = Area × thickness, and assuming area of Cu film = area of In film for our substrate holder, the relationship below follows.

$$\frac{M_{Cu}}{M_{In}} = \frac{D_{Cu} t_{In}}{D_{In} t_{In}} \qquad\qquad (c3)$$

where D_{Cu} is the density of Cu film, D_{In} is the density of In film, t_{Cu} is the thickness of Cu film , and t_{In} is the thickness of In film.

Dividing equation c3 by c2 and rearranging we get

$$\frac{t_{Cu}}{t_{In}} = \frac{R Z_{Cu} D_{In}}{Z_{In} D_{Cu}} \qquad (c4)$$

Substituting numerical values of Z_{Cu}, Z_{In}, D_{Cu}, and D_{In} and rearranging we get

$$t_{In} = \frac{2.3 t_{Cu}}{R} \qquad (c5)$$

APPENDIX D

Relation between plane-spacing equations and Braggs law

A general relation to predict the diffraction angle of any set of planes exists. This relation is obtained by combining the Bragg law and the plane-spacing equation applicable to the particular crystal involved.

Some of the known plane spacing equations are given below:

Cubic:
$$\frac{1}{d^2} = \frac{h^2 + k^2 + l^2}{a^2} \qquad (\text{d}1)$$

Tetragonal:
$$\frac{1}{d^2} = \frac{h^2 + k^2}{a^2} + \frac{l^2}{c^2} \qquad (\text{d}2)$$

Hexagonal:
$$\frac{1}{d^2} = \frac{4}{3}\left(\frac{h^2 + hk + k^2}{a^2}\right) + \frac{l^2}{c^2} \qquad (\text{d}3)$$

Rhombohedral:

$$\frac{1}{d^2} = \frac{\left(h^2 + k^2 + l^2\right)\sin^2\alpha_a + 2\left(hk + kl + hl\right)\left(\cos^2\alpha_a - \cos\alpha_a\right)}{a^2\left(1 - 3\cos^2\alpha_a + 2\cos^3\alpha_a\right)} \qquad (\text{d}4)$$

Orthorhombic: $\dfrac{1}{d^2} = \dfrac{h^2}{a^2} + \dfrac{k^2}{b^2} + \dfrac{l^2}{c^2}$

(d5)

Monoclinic: $\dfrac{1}{d^2} = \dfrac{1}{\sin^2 \beta}\left(\dfrac{h^2}{a^2} + \dfrac{k^2 \sin^2 \beta}{b^2} + \dfrac{l^2}{c^2} - \dfrac{2hl\cos\beta}{ac} \right)$

(d6)

Triclinic: $\dfrac{1}{d^2} = \dfrac{1}{v^2}\left(S_{11}h^2 + S_{22}k^2 + S_{33}l^2 + 2S_{12}hk + 2S_{23}kl + 2S_{13}hl \right)$

(d7)

where,   v = volume of unit cell,

$$S_{11} = b^2c^2\sin^2\alpha_a,$$

$$S_{22} = a^2c^2\sin^2\beta,$$

$$S_{33} = a^2b^2\sin^2\gamma,$$

$$S_{12} = abc^2(\cos\alpha_a\cos\beta - \cos\gamma),$$

$$S_{23} = a^2bc(\cos\beta\cos\gamma - \cos\alpha_a),$$

$$S_{13} = ab^2c(\cos\gamma\cos\alpha - \cos\beta)$$

As an example, $CuInSe_2$ phase posses a tetragonal structure with axes a and c and therefore combining

$$\lambda = 2d\sin\theta$$

(d8)

and

$$\frac{1}{d^2} = \frac{h^2 + k^2}{a^2} + \frac{l^2}{c^2}, \tag{d9}$$

we have

$$Sin^2\theta = \frac{\lambda^2}{4}\left(\frac{h^2 + k^2}{a^2} + \frac{l^2}{c^2}\right) \tag{d10}$$

and similar equations can readily be obtained for other crystal systems.

APPENDIX E

Initial number of moles and reaction rate constants calculations

In this research, the initial number of moles of different species in the starting CuIn bilayer(Cu/In = 0.8) is given in table E.1. Reaction rate constants for temperatures 350 - 500 °C is shown in table E.2.

Table E.1. Reaction rate constants for different temperatures

Reaction Rate constant	Temperature (°C)			
	350	400	450	500
k'_3 (min^{-1})	0.143	0.368	0.833	1.694
k'_5 (min^{-1})	0.045	0.190	0.652	1.913
k'_7 (cm^3 mol^{-1} min^{-1})	16.009	22.914	31.21	40.845

Table E.2. Number of moles of different species in the starting CuIn bilayer.

Thickness (Å)		Species moles			
Cu	In	N_o, Cu	N_o, In	$N_{Cu11In9}$	N_{In}
2500	6906	1.98×10^{-5}	2.48×10^{-5}	1.80×10^{-6}	8.57×10^{-6}
1250	3453	9.92×10^{-6}	1.24×10^{-5}	9.02×10^{-7}	4.28×10^{-6}
938	2591	7.45×10^{-6}	9.31×10^{-6}	6.77×10^{-7}	3.21×10^{-6}
625	1727	4.96×10^{-6}	6.20×10^{-6}	4.51×10^{-7}	2.14×10^{-6}